Multiphase Smoothed Particle Hydrodynamics Modeling of Supercooled Large Droplets Impingement and Solidification at In-flight Icing Conditions

Xiangda Cui

Department of Mechanical Engineering

McGill University

Montreal, Québec

April 2021

A thesis submitted to McGill University in partial fulfillment of

the requirements of the degree of Doctor of Philosophy

Table of Contents

ACKNOWLEDGEMENTS iv

NOMENCLATURE v

LIST OF FIGURES viii

ABSTRACT xiii

RÉSUMÉ xv

CHAPTER 1 INTRODUCTION 1

1.1 Motivation and objectives 1

1.1.1 In-flight icing 1

1.1.2 Supercooled Large Droplets (SLDs) 1

1.1.3 Thesis objectives 3

1.2 Literature review 3

1.2.1 Experimental study of SLD 3

1.2.2 CFD study of SLD 5

1.2.3 Smoothed Particle Hydrodynamics (SPH) 7

1.3 Thesis contributions 10

1.3.1 Algorithm 10

1.3.2 Engineering 10

1.4 Thesis outline 11

CHAPTER 2 METHODOLOGIES 12
2.1 Governing equations 12
2.2 Multiphase SPH equations 13
2.3 Numerical techniques 16
2.3.1 Surface tension model 16
2.3.2 Boundary conditions at solid surfaces 17
2.3.3 Contact angle model 18
2.3.4 Particle shifting technique 22
2.3.5 Latent heat model and ice fraction 22
2.3.6 Supercooled solidification model 23
2.4 MPI parallelization 26
2.4.1 A cell system and neighbor searching 26
2.4.2 3D partitioning 27
2.4.3 The sequence of collecting particles 28
2.4.4 Re-indexing particles 30
2.4.5 Parallel efficiency 31
CHAPTER 3 RESULTS 34
3.1 Droplet impingement on a water film 34
3.1.1 Validation: a droplet impinging on a water film at low speed 34
3.1.2 A droplet impinging on a water film at high speed (aeronautical speed) 37

3.1.3 A study of the effects of water thickness 41
3.1.4 A study of the effects of impact angle 43
3.1.5 A study of the effects of droplet speed 45
3.1.6 A study of the effects of droplet diameter 49
3.2 Droplet impingement and solidification on cold solid surfaces 52
3.2.1 Validation: two-phase Stefan solidification 52
3.2.2 A stationary droplet freezing on a cold surface 53
3.2.3 A droplet impinging and freezing on a cold surface 57
3.2.4 A droplet obliquely impinging and freezing on a cold surface 62
3.3 Droplet impingement and solidification on hydrophobic surfaces 67
3.3.1 Validation: evolution of 3D droplets on solid surfaces 67
3.3.2 A droplet impinging on a hydrophobic surface 71
3.3.3 A droplet impinging on a cold superhydrophobic surface 74
3.4 SLD impingement on iced surfaces with supercooled effects 78
3.4.1 Validation: SLD impinging on an ice target 78
3.4.2 A study of the effects of droplet supercooling degree 82
3.4.3 A study of the effects of droplet speed 85
CHAPTER 4 CONCLUSIONS 88
REFERENCES 91

ACKNOWLEDGEMENTS

I would like to express my deepest gratitude to my supervisor, Professor Wagdi G. Habashi, for giving me the opportunity to conduct research at McGill University's CFD Laboratory, and for his continuous support and guidance throughout my studies.

I would like to thank Dr. Ahmed Bakkar and Dr. Vincent Casseau for giving me valuable advice on many aspects of my research. I am also thankful to all my colleagues in CFD Lab for creating a delightful working environment.

I would like to acknowledge the Natural Sciences and Engineering Research Council of Canada (NSERC) for funding this research through a Discovery Grant. I am also grateful to Compute Canada for the use of their supercomputing resources.

Finally, I give my gratitude to my parents, brother, sister-in-law and nephews. Their unconditional love, encouragement and support make this long journey possible and meaningful.

NOMENCLATURE

Abbreviation

CFD	Computational Fluid Dynamics
CFL	Courant–Friedrichs–Lewy number
CPU	Central Processing Units
CUDA	Compute Unified Device Architecture
GPU	Graphics Processing Units
IPS	Ice Protection Systems
LS	Level Set
LWC	Liquid Water Content
MOF	Moment of Fluid
Ma	Mach number
MPI	Message Passing Interface
OpenMP	Open Multi-Processing
SPH	Smoothed Particle Hydrodynamics
SLD	Supercooled Large Droplets
VOF	Volume of Fluid

Latin Symbols

c	sound speed
C_{v}	specific heat
e	internal energy of particle
f_{ice}	ice fraction of particle

$\boldsymbol{F}_i^{adh}$	artificial adhesion force term
$\boldsymbol{F}_i^{sf}$	surface tension term
h	characteristic length of kernel function
k	thermal conductivity
L	specific latent heat
m	mass of particle
$\boldsymbol{n_i}$	unit normal of interface
p	pressure of particle
p_0	background pressure
Q^{Loss}	heat loss of particle
$\boldsymbol{r}$	position of particle
s_j^i	color function
T	temperature of particle
$\boldsymbol{u}$	velocity of particle
V	volume of particle
W	kernel function
$\boldsymbol{\nabla} W$	gradient of kernel function

Greek Letters

α	artificial viscous coefficient
β	surface tension coefficient
γ	fluid constant
δ	artificial diffusive coefficient

ε	artificial adhesion force coefficient
θ	contact angle
λ	partial color coefficient
π_{ij}	artificial viscous term
ρ	density of particle
ρ_0	initial density of particle
Ψ_{ij}	artificial diffusive term

Subscript

i	particle *i*
j	neighbor particle of *i*

LIST OF FIGURES

Figure 1. Smoothing kernel. 13

Figure 2. The framework of the multiphase SPH solver. 15

Figure 3. Fixed ghost particles near a solid wall corner. 17

Figure 4. Droplets on surfaces with different contact angles. 18

Figure 5. Different colors are assigned to fixed ghost particles at various contact angles. ... 20

Figure 6. The corrected color of fixed ghost particles when the air-water interface is away from triple-phase points. 21

Figure 7. Normal corrections to fixed ghost particles when triple-phase points are in their kernel support domains. 21

Figure 8. Latent heat model for particles at freezing temperature. 23

Figure 9. Dendrite growth speeds measured in experiments and used in simulations. 25

Figure 10. Supercooled solidification model. 25

Figure 11. All neighbors of particles in cell (i, j, k) distribute in 27 adjacent cells. 26

Figure 12. The shared zones are the cells along the communication interfaces. 27

Figure 13. 1D, 2D and 3D partitioning strategies for a cubic domain on 8 processors. 28

Figure 14. The sequence of data communication. 29

Figure 15. Re-indexing technique to accommodate migrating particles. 31

Figure 16. Solver speed-up to compute 110 million particles for 50 time steps on 32 to 1024 cores. 32

Figure 17. Solver parallelization efficiency to compute 110 million particles for 50 time steps on 32 to 1024 cores. 33

Figure 18. Effects of particle load on computing efficiency with 64 cores. 33

Figure 19. Sketch of a low-speed droplet impinging on a water film. 34

Figure 20. Measurements of the post-impact water crown diameter and height. 35

Figure 21. Top and side views of the water crown accounting for surface tension (left half) and neglecting surface tension (right half)..... 35

Figure 22. Non-dimensional time history of the post-impact water crown diameters. 36

Figure 23. Non-dimensional time history of the post-impact water crown heights. 36

Figure 24. Sketch of a droplet impinging on a water film at an aeronautical speed..... 37

Figure 25. Snapshots of the water crown at t* = 2.23 with different total numbers of particles. 38

Figure 26. The crown profiles at t* = 2.23 with different total numbers of particles..... 39

Figure 27. The time history of the crown diameters with different total numbers of particles. 39

Figure 28. Snapshots of the droplet impingement at aeronautical speed at t* = 0.55, 1.11, 1.67 and 2.23 (top to bottom)..... 40

Figure 29. Water crown on different water film thicknesses..... 41

Figure 30. Profiles of the cross-section of the water crown with various water film thicknesses. 42

Figure 31.Time history of the crown dimeters with various water film thicknesses..... 43

Figure 32. Sketch of oblique impingements on a water film..... 43

Figure 33. Snapshots of oblique droplet impingement with various impact angles at t* = 0.55, 1.11, 1.67 and 2.23..... 44

Figure 34. Sketch of droplet impingement on a thin water film at various speeds. 45

Figure 35. Snapshots of a 0.5 mm droplet impacting a water film of 0.012 mm at t* = 0.1189, 1.189, 2.378, 3.568 and 4.758 (top to bottom)..... 46

Figure 36. Radial binning method to count the number of particles in each section..... 46

Figure 37. The average height (black lines) and the number (red lines) of the splashing particles in radial sections..... 48

Figure 38. Sketch of droplet impingement on a thin water film with different diameters. ... 49

Figure 39. The average height (black lines) and the number (red lines) of the splashing particles in radial sections..... 51

Figure 40. Sketch of the 1D two-phase Stefan problem..... 52

Figure 41. Time history of ice front position from analytical solution and SPH simulations of various particle spacings for the two-phase Stefan problem. 53

Figure 42. Sketch of the two stages of a post-impact still droplet freezing on a cold plate. . 54

Figure 43. Snapshots of a droplet impacting a cold plate at different time instances. 55

Figure 44. Snapshots of the solidification of a still droplet with a base diameter of 3.56 mm and a height of 1.58 mm on a −30 °C plate. 56

Figure 45. Time history of the position of central freezing front of a still droplet with a base diameter of 3.56 mm and a height of 1.58 mm on a −30 °C plate..... 57

Figure 46. Sketch of the droplet normal impingement..... 58

Figure 47. Snapshots of the impingement stage at different time instances..... 59

Figure 48. Snapshots of the solidification stage at different time instances..... 60

Figure 49. Sketch of the radial binning technique employed to count the number of ice particles in each concentric zone. 61

Figure 50. Post-impact ice particle distribution for the normal impingements. 61

Figure 51. Sketch of the oblique droplet impingement. 62

Figure 52. Snapshots of the oblique impingement stage at different time instances. 63

Figure 53. Snapshots of the solidification stage at different time instances. 64

Figure 54. Sketch of the binning technique in *x*-direction employed to count the number of ice particles in each zone. 65

Figure 55. Post-impact ice particle distributions along the *x*-direction for the oblique impingements. D = 0.5 mm, T_d = 0 °C, T_p = −50 °C, α = 30° and V = 5 m/s & 100 m/s. 65

Figure 56. Post-impact ice particle distributions along the *y*-direction for the oblique impingements. D = 0.5 mm, T_d = 0 °C, T_p = −50 °C, α = 30° and V = 5 m/s & 100 m/s. 66

Figure 57. Evolution of 3D droplets on solid surfaces. 67

Figure 58. Snapshots of the evolution of droplets on surfaces with various contact angles: 45°(left), 90°(middle) and 135°(right). 69

Figure 59. Diameters of the solid-liquid contact aeras of the equilibrium droplets on solid surfaces with contact angles from 45° to 165°. 70

Figure 60. Heights of the equilibrium droplets on solid surfaces with contact angles from 45° to 165°. 70

Figure 61. Sketch of a droplet impacting on a hydrophobic surface. 71

Figure 62. Snapshots of a 2.75 mm droplet impacting-spreading-retracting on a hydrophobic surface at t = 1.31, 3.14, 6.02, 8.21, 10.26, 14.02, 20.54 and 24.12 ms (left to right; top to bottom). 72

Figure 63. Time history of the non-dimensional spreading diameters of a 2.75 mm water droplet impacting a hydrophobic surface at 1.18 m/s. 73

Figure 64. Sketch of a droplet impacting on a cold superhydrophobic surface. 74

Figure 65. Snapshots of the central section of the SPH simulation of a 3.06 mm droplet impacting a −15 °C superhydrophobic surface at 1.4 m/s at t = 1.885, 3.771, 7.542, 9.428, 11.314, 15.085, 18.856 and 22.628 ms with the contours of *z*-axis velocity (left) and the ice fraction(right). 76

Figure 66. Time history of the contact area ratio, $A/Amax$, of a 3.06 mm droplet impacting a −15 °C superhydrophobic surface at 1.4 m/s. 77

Figure 67. A supercooled water droplet entirely bouncing from a superhydrophobic surface by experiments [21] and SPH simulations. 77

Figure 68. Sketch of a −16 °C SLD impinging on an ice target. 78

Figure 69. Time history of the lamella heights in different particle resolutions. 79

Figure 70. Top view of the SLD impinging on an ice target at t = 3.86 ms. 80

Figure 71. Snapshots of SLD impinging and freezing on an ice target at t = 1.26, 2.56, 3.86, 5.16 & 7.66 ms (blue: water; light red: ice; grey: air). 81

Figure 72. Sketch of SLD impinging on an ice target with different supercooling degrees. 82

Figure 73. Time history of the lamella heights for different droplet temperatures. 83

Figure 74. Snapshots of SLD impinging and freezing on an ice target with different droplet temperatures. 84

Figure 75. Sketch of SLD impinging on an ice target at various speeds. 85

Figure 76. Snapshots of SLD impinging and freezing on an ice target at different speeds at t* = 0.918, 1.837, 2.755, and 5.511. 87

Figure 77. Time history of the lamella heights at different impact speeds. 87

ABSTRACT

Encounters with Supercooled Large Droplets (SLD) pose a danger to aircraft, as they can cause ice accretion beyond the reach of ice protection systems. In-flight icing effects must meet the regulations of airworthiness authorities in order for a new class of aircraft to obtain a type certification. Since flights into natural icing conditions and wind/icing tunnel tests cannot fully explore the SLD icing envelope, Computational Fluid Dynamics (CFD) has become an indispensable tool for assessing in-flight icing effects. However, the SLD modules of such in-flight icing simulation codes rely on empirical data or extrapolation from low-speed experiments. This thesis aims to develop a multiphase Smoothed Particle Hydrodynamics (SPH) solver for conducting "numerical experiments" of SLD impingement at flight speeds, to ultimately yield a macroscopic SLD model that can be embedded into in-flight icing simulation codes.

SPH is a mesh-free CFD method suitable for SLD problems as it can handle complex interfaces and model multi-phase physics. In the multiphase SPH framework presented here, the inviscid momentum and energy equations are solved for flow and heat transfer, along with an equation of state linking pressure and density. A multiphase model is used to represent interfacial flows, and a fixed ghost particle method to enforce boundary conditions. Artificial viscous and diffusive terms are employed to smooth physical fields and decrease numerical instability, while a particle shifting technique is used to alleviate anisotropic particle distribution. Several numerical techniques are proposed to model the complex physics of SLD impingement such as a contact angle model to represent the non-wetting properties of hydrophobic surfaces, a latent heat model to account for phase change and a supercooled solidification model to capture dendritic freezing.

The solver is validated against a series of experimental results, showing good agreement. It is then first applied to droplets impinging at flight speeds on a water film to study the effects on the

post-impact water crown of droplet speed and diameter, surface tension, water film thickness, and impact angle. Droplets impacting on cold solid surfaces are then simulated to study freezing time and post-impact ice particle distribution for a range of speeds and impact angles. Following this, an improved contact angle model is used to study the interaction between droplets and hydrophobic/superhydrophobic coatings. Finally, SLD impinging on ice surfaces are studied via a supercooled solidification model, with supercooling degree and impact speed effects on residual ice analyzed.

This thesis thus develops an SPH numerical framework capable of simulating SLD impingement and solidification at in-flight icing conditions. It provides a toolset for comprehensive parametric studies of SLD impingement, paving the way for a macroscopic SLD model for in-flight icing simulation codes.

RÉSUMÉ

L’encontre en vol de grosses gouttelettes surfondues (Supercooled Large Droplets, soit SLD) présente un danger pour les aéronefs, en causant un cumul de givre dépassant la portée des systèmes de protection. De tels effets doivent être soigneusement examinés conformément aux règlements des autorités de certification de la sécurité aérienne, avant d’obtenir un certificat de vol en mode givrant. Étant donné que les essais en soufflerie ou en vol ne permettent pas l’exploration complète de l’enveloppe de vol en mode givrant, plus particulièrement pour les SLD, la simulation numérique (Computational Fluid Dynamics, soit CFD), est un outil indispensable pour évaluer de tels effets. Toutefois, les modules SLD qu’utilisent les logiciels de simulation du givrage en vol se basent soit sur des données empiriques, soit sur une extrapolation d'expériences à basse vitesse. Il existe donc un besoin pressant de données numériques de l’impact des SLD à des vitesses de vol beaucoup plus élevées qui puissent aboutir à un modèle SLD macroscopique intégré aux logiciels de simulation du givrage en vol.

L'hydrodynamique des particules lissées (Smoothed Particle Hydrodynamics, soit SPH) est une méthode CFD appropriée pour la simulation des SLD car elle permet, sans maillage, de gérer des interfaces complexes et de modéliser la physique multiphasique des mélanges eau-glace. Dans le cadre SPH multiphasique présenté dans cette thèse, les équations de bilan de la quantité de mouvement et de l'énergie sont résolues pour l’écoulement et le transfert de chaleur, avec une équation d'état explicitement reliant pression et densité. Un modèle multiphasique représente les flux inter faciaux, et une méthode de particules fantômes fixes est choisie pour construire certaines conditions aux parois. Un terme visqueux artificiel et un terme diffusif sont utilisés pour lisser les champs physiques et réduire l'instabilité numérique, et une technique de déplacement des particules pour rendre la distribution des particules moins anisotrope. Une gamme de techniques

numériques sont de plus proposées pour la modélisation de la physique complexe de l'impact des SLD. Des modèles sont proposés pour l'angle de contact des surfaces hydrophobes, la chaleur latente pour tenir compte des changements de phase, et de solidification surfondue pour capturer la congélation dendritique.

Le solveur est validé versus une panoplie de résultats expérimentaux, démontrant une bonne concordance. Il est appliqué aux gouttelettes entrant en collision, à des vitesses de vol, avec un film d'eau pour étudier les effets sur la couronne d'eau de la vitesse et diamètre des gouttelettes, de la tension superficielle, la distribution des particules, l'épaisseur du film et de l'angle d'impact. Les gouttelettes impactant les surfaces solides froides sont ensuite simulées pour étudier le temps de congélation et la distribution des particules rebondissant à différentes vitesses et angles. En complément, l'interaction entre les gouttelettes et les revêtements hydrophobes / super hydrophobes est examinée en utilisant un modèle d'angle de contact pouvant mieux représenter les propriétés non mouillantes. Finalement, les simulations des SLD impactant les surfaces de glace sont menées par un modèle de solidification en surfusion permettant d'analyser les effets du degré de surfusion et de la vitesse d'impact sur la couche de glace résiduelle.

Cette thèse présente donc un cadre numérique SPH capable de simuler l'impact et la solidification des SLD dans des conditions appropriées au givrage en vol. Elle fournit donc un outil pratique pour effectuer des études paramétriques complètes de l'impact des SLD et est un pas important pour la construction éventuelle d'un modèle de prédiction de la distribution post-impact des SLD pour les logiciels de simulation du givrage en vol.

CHAPTER 1 INTRODUCTION

1.1 Motivation and objectives

1.1.1 In-flight icing

In-flight icing poses a serious risk to aviation safety: ice accretion on aircraft lifting and control surfaces, engine inlets, appendages may cause increased drag, reduced lift, early stall, flameout and erroneous/inoperative sensors and probes [1]. One or more combinations of these adverse effects can result in substantial and sudden performance degradation, leading to incidents and/or accidents [2].

Such icing effects must be assessed through extensive procedures under airworthiness agencies' certification standards, such as Appendices C and O of Federal Aviation Administration's Part 25 [3-4], European Aviation Safety Agency's CS-25 [5], and Transport Canada Civil Aviation's CARs [6].

1.1.2 Supercooled Large Droplets (SLDs)

According to Appendix O [4], new aircraft must be protected against Supercooled Large Droplets (SLDs) encompassing freezing drizzle and freezing rain, which have a diameter range of 50-1000 μm [4]. SLDs behave differently from smaller cloud droplets as they may break up or coalesce before impact, spread and splash during impact, and bounce after impact [7]. Splashing and bouncing droplets can then re-impinge further back on the aircraft, beyond the reach of ice protection systems (IPS); a dangerous situation [8].

Airworthiness for flying into known icing conditions is usually demonstrated by a judicious combination of Computational Fluid Dynamics (CFD) simulations, dry/icing wind tunnel tests, and test flights into natural icing conditions [9].

Tests in dry/icing wind tunnels have considerable scaling limitations, as neither droplets characteristics, full geometry nor altitude conditions can be fully replicated. Due to the low accessibility to such facilities, the wait time may be long, and only a portion of the icing envelope can be investigated [10]. In addition, replicating SLD conditions in wind tunnels is challenging, as large droplets may break up during acceleration or settle at its base before reaching test sections [11].

SLD conditions are difficult to locate in nature, and flights into such natural icing conditions are dangerous and expensive. Therefore, only limited number of regulation conditions can be tested or encountered during natural icing tests [1].

As computer power is rapidly growing, CFD can conduct icing simulations on complete aircraft, under high-altitude conditions, with no scaling and is capable of exploring the full icing envelope, making it an indispensable component of the certification process of Appendices C and O.

Several in-flight icing simulation codes have been developed and widely used, such as FENSAP-ICE [1] for 3D flows and LEWICE3D [12] for 2.5D flows, as only two examples. However, their SLD modules, evaluating the mass and velocity of the secondary droplets after impingement, are either heuristic correlations or extrapolations from droplet experiments at low speeds and/or non-SLD conditions [8,12]. Therefore, a need exists for studying single SLD impingement and solidification under aeronautical conditions.

1.1.3 Thesis objectives

This work aims to introduce a triple-phase (air-water-ice) Smoothed Particle Hydrodynamics (SPH) parallel solver by combining and enhancing many disparate numerical techniques to simulate single SLD impingement and solidification at in-flight icing conditions. This work can advance the understanding of SLD's impinging and freezing behaviour and provide a toolset for conducting comprehensive parametric studies of SLD impingement and building a macroscopic SLD model for in-flight icing simulation codes.

1.2 Literature review

1.2.1 Experimental study of SLD

SLD clouds impinging on airfoils were first investigated in icing tunnels. SLDs of diameters 50 to 180 μm were accelerated in airflows to a speed range of 77 to 103 m/s and impacted on airfoils in [13]. The mass loss ratio due to splashing was obtained for a number of tests with different droplet sizes and liquid water content (LWC). The optical visualization techniques were improved in [14] to capture the outcomes of SLD droplets impacting on clean/iced airfoils at speeds up to 60 m/s. These experiments mainly studied the correlations between the mass loss ratio and the impingement characteristics such as droplet diameter, impact speed and LWC.

The fundamental mechanisms of SLD impingement and solidification could not be clearly revealed by observing SLD clouds impinging on airfoils. Many single droplet experiments [15-20] were thus conducted to explore the complex physics of SLD and investigate the effects of impact speeds, supercooling degrees, solid substrate materials, surface wettability and plate temperatures on the droplet behavior.

Two series of experiments were carried out in [15] to analyze single SLD behaviour, using shadowgraph and infrared imaging techniques to visualize the impingement dynamics and heat transfer. At first, −5 °C supercooled droplets of 1.5 mm impacting on −18 to 0 °C solid surfaces at a speed of 3.4 m/s were conducted, and the effects of phase change on spreading diameters were reported. They showed that supercooled solidifications could hinder droplet bouncing on hydrophobic surfaces. Room-temperature droplets sized from 130 to 200 μm impacting on solid surfaces at a speed range of 10 to 63 m/s were then conducted to identify various impingement outcomes and measure the spreading radii and speeds of the splashing jet.

Room-temperature droplets impacting on ice surfaces of −15 to −5 °C at speeds of 1.4 to 2.8 m/s were studied in [16], and droplet spreading diameters were recorded and analyzed, finding that droplets did not retract from maximum spreading and that cooler ice surfaces decreased the spreading area.

The solidification of supercooled liquid down to −20 °C was investigated in [17] by a Hele-Shaw cell that overcame optical distortions, clearly presenting the process of nucleation and dendrites growth. The spreading speeds of the initial ice layer and dendritic front in supercooled water were measured for a range of supercooling degrees, showing that the speeds were related to the growth rate of a single ice dendrite. The nucleation sites of water droplet impacting onto a cold substrate were then studied in [18], using a high-speed video system. It was observed that the generated nanobubbles increased the nucleation rate. The process of SLD impacting on ice surfaces was further explored in [19], finding that lower droplet temperatures or higher impact speeds caused thinner residual ice.

Supercooled water droplets impingement on cold hydrophobic surfaces were studied in [20], showing that droplet bouncing was hindered when both droplet and plate were below water freezing temperature.

Droplets impacting on supercooled micro/nano-structure surfaces were conducted to examine the temperature-dependent droplet-wall interactions in [21]. It was found that the chosen superhydrophobic materials could entirely repel low-speed water droplets, without ice formation, for droplet temperatures down to −25 °C.

Aeronautical-speed SLD experiments still face technical limitations. Accelerating droplets to high speeds is not easy, as aerodynamic forces may break droplets up. Visualization and quantitative measurement of SLD post-impact mass distributions are also challenging, especially for high-speed impingement that is accompanied by a large number of splashing particles. Although most of these experiments are conducted at low speeds, they still reveal some important physical mechanisms in SLD impingement and provide benchmarks for validating numerical models. CFD simulations can extend the ranges of droplet diameter, impinging speed and supercooling degree, thus obtaining a deeper understanding of SLD behaviour at in-flight icing conditions.

1.2.2 CFD study of SLD

The intricacies of modeling single SLD impingement arise from complex interfaces and multi-physics (phase change, supercooled effects, ice-water mixtures and non-wetting properties), as SLD may break up, coalesce, splash, bounce, and fully or partially freeze on various dry/wet surfaces.

Mesh-based CFD simulations use tracking or capturing techniques to handle interfacial problems. Interface-tracking methods have to update meshes as the flow evolves, and they are only

accurate for small interface motions [22]. On the other hand, interface-capturing techniques can be performed on fixed grids and are flexible and efficient. For example, the Volume of Fluid (VOF) method [23] defines a function representing the fractional volume of the cell occupied by one phase of fluid, while the Level-Set (LS) method [24] uses a signed distance function to reconstruct the interfaces.

The LS method, combining variational multi-scale meshes and a higher-order Taylor-Galerkin temporal discretization within a finite element framework, was used in [11,25] to model droplet impingement on solid surfaces and water films at speeds of 50 to 100 m/s in 2D. The effects of droplet size and velocity, airspeed, impact angle and surface wettability were investigated.

A Moment-of-Fluid (MOF) method, a generalization of VOF, was adopted in [26] to simulate 3D droplets impacting on dry or wet surfaces, at speeds around 50 m/s. Effects of the surrounding air on water crowns were studied, finding that lower air density could suppress the splash on dry surfaces. Droplets obliquely impacting on thin liquid films at speeds of 60 to 200 m/s were further conducted in [27], who reported that the higher tangential velocity caused lower splashing behind the advancing droplet, and that a thinner liquid film led to earlier crown breakup.

Droplets impacting on dry or wet solid surfaces were simulated in [28] at a maximum speed of 20 m/s with a combined LS-VOF method to represent the interfaces. They found that impingement on dry surfaces caused much less splashing than on water films, and that a higher air density might trigger splashing.

Supercooled droplets impacting and freezing on superhydrophobic surfaces at a speed range of 1 to 5 m/s were simulated in [29], with a classical nucleation model to initiate solidification, and showed that supercooling could hinder droplet bouncing.

Although interface-capturing methods are capable of representing complex interfaces, they cannot strictly conserve mass, particularly for high-speed impingement with many splashing droplets. Moreover, the interactions between droplet impingement and solidification render the implementation of such techniques complicated. To the author's knowledge, there is no published work that can simultaneously simulate aeronautical-speed SLD impingement and solidification.

1.2.3 Smoothed Particle Hydrodynamics (SPH)

The SPH method can easily represent evolving interfaces, exactly conserve mass and intrinsically model complex physics such as phase change and mixtures [30], making it a suitable approach to simulate high-speed SLD impingement and solidification.

The SPH method was first proposed by Gingold and Monaghan [31] and Lucy [32] to solve astrophysical problems by approximating the spatial derivatives of physical fields through an integration over neighbour particles. Following its success in astrophysics, SPH was then applied to free-surface flows by Monaghan [33] and to interfacial flows [34-35], demonstrating its robustness and flexibility for fluid flow problems.

The original SPH scheme was characterized by numerical instabilities and unphysical noise, and a number of numerical techniques were introduced to overcome these problems. An artificial viscous term was first proposed in [36] to decrease excessive particle oscillations in shock problems and was further used to evaluate both shear and bulk viscosity in free-surface flows [33]. A diffusive term was later introduced into the continuity equation to reduce the high-frequency spurious noise in pressures [37]. The particle shifting technique was first proposed to address the numerical instability caused by anisotropic distributions in the incompressible SPH (ISPH) method [38], and it was then extended to the SPH method [39]. A specific technique handling free surfaces when performing particle shifting was reported in [40].

When the SPH method was applied to wall-bounded flows in [33], repellent forces were used to represent solid walls. This method was capable of modeling complex solid boundaries, but it could also cause spurious particle oscillations near solid boundaries due to kernel truncations. A ghost particle method was thus proposed in [34] and was further developed into a fixed ghost particle method in [41], proving to be more stable and efficient for complex geometries.

During these developments, SPH has been successfully applied to a variety of problems [42-45], including droplet impingement [46-48]. Melting ceramic droplets impinging and solidifying on inclined solid surfaces were studied in [46], approximating surface tension with an attraction force, and representing solidification by turning captured fluid particles into solid ones. A single-phase SPH model was used in [47] to simulate droplets impacting on a liquid surface, and post-impact water crowns and central columns showed good agreement when compared to experimental results. The interaction between droplets and dry or wet walls was simulated, and the effects of impact speeds on splash crowns were investigated in [48]. It is worth mentioning that all these works were conducted at low speeds and neglected the air phase, thus having limited direct applicability to SLD impingement at in-flight conditions.

Heat conduction and solidification problems have been studied via SPH in [49-50]. The main challenge of discretizing the energy equation in SPH was identified to be the poor estimation of second-order derivatives in [49], and thus an integral form of the energy equation was proposed to perform SPH interpolations. This approach was applied to several Stefan problems, showing good agreement with analytical solutions. Multiphase solidification problems were further simulated in [50], in which fluid particles and virtual solid particles without mass were employed to represent phase transitions by transferring the mass of freezing fluid particles to virtual solid particles. The

solidification of pure liquids and solutions was simulated without fluid motion, showing good agreement with analytical and experimental results.

To study droplet impacting on hydrophobic/superhydrophobic surfaces, the non-wetting properties of solid boundaries have to be addressed. A contact angle model was introduced in [51] based on a continuum surface tension model for simulating 2D triple-phase interactions. This model was further developed in [52] by correcting the normal of the liquid-gas interface to the desired contact angles near the triple-phase point, and 3D equilibrium non-wetting problems and 2D droplet pining effects were simulated. To avoid kernel truncation, another contact angle model [53] was proposed by extrapolating droplet profiles into solid ghost particles while computing the surface tension, and the model was applied to 2D droplets impacting on solid surfaces with contact angles ranging from 50° to 175°. However, none of these studies simulated 3D droplet impinging on hydrophobic surfaces, as the dynamical triple-phase point requires a robust contact angle model.

Finally, one must remark that 3D multiphase SPH simulations are intensive and need high performance computing. Parallel SPH codes can use various programming interfaces on different hardware architectures, such as OpenMP (Open Multi-Processing) [54-55] and MPI (Message Passing Interface) [56-58] on CPUs (Central Processing Units) and CUDA (Compute Unified Device Architecture) on GPUs (Graphics Processing Units) [59-61].

The parallelization of SPH is different from that of mesh-based methods due to the dynamical neighbor lists and migrating particles between adjacent subdomains. OpenMP and GPU use shared-memory architectures and allow neighbor searching without resorting to data communication. However, due to the overhead of synchronization and communication, the scalability of OpenMP sharply drops when threads exceed a certain number, e.g., 24, as mentioned in [54]. The main barriers to implementing SPH on GPUs are limited memory space and the

communication bottleneck between GPUs and CPUs. MPI uses a distributed-memory architecture and requires complex data communications that increase coding complexity but allow large-scale SPH simulations on computer clusters. Thus, in conclusion, this work develops an MPI-based parallelization for simulations of the order of hundreds of millions of particles.

1.3 Thesis contributions

1.3.1 Algorithm

This thesis makes fundamental contributions to the SPH method, leading to a comprehensive triple-phase (air-water-ice) framework for modeling the multi-physics of SLD impingement and solidification at in-flight icing conditions in 3D.

1. A multiphase model combining a number of disparate numerical techniques is developed to simulate aeronautical-speed SLD impingement.
2. A latent heat model is developed to simulate droplet impingement with phase change.
3. A supercooled solidification model is proposed to represent the supercooled effects in SLD impingement.
4. A robust contact angle model is developed to account for the non-wetting properties of hydrophobic/superhydrophobic surfaces.
5. A massively parallel framework based on MPI is built to enable large-scale simulations.

1.3.2 Engineering

This thesis makes significant contributions to the engineering field, particularly for in-flight icing.

1. Simulating SLD impingement and solidification at in-flight icing conditions can advance the microscopic knowledge of SLD impinging and freezing behaviour.

2. A comprehensive numerical tool is developed for conducting numerical experimentation of single SLD impingement, and a macroscopic SLD model can thus be built for in-flight icing simulation codes.
3. This work can also benefit other fields beyond in-flight icing, such as electricity-transmission-lines/wind-turbines icing, spray coating, and ink-jet printing.

1.4 Thesis outline

The thesis is organized as follows: the mathematical background and the numerical framework are introduced in Section 2. The solver is validated in Section 3 against experimental results and applied to SLD impingement under various conditions. Droplets impinging on thin water films at aeronautical speeds are simulated to investigate the effects on the post-impact water crown of droplet diameter and speed, impact angle, and water film thickness. Droplets impinging and freezing on cold surfaces are then simulated at different speeds to discuss the interactions between impingement and solidification. After that, the droplet impinging on hydrophobic and superhydrophobic surfaces are also simulated to explore the potential anti-ice coatings based on non-wetting properties. Finally, an SLD impinging on an ice target is modeled accounting for supercooled effects with various supercooling degrees and impact speeds. The main findings are summarized in the last section and future work is proposed.

CHAPTER 2 METHODOLOGIES

2.1 Governing equations

The flow is governed by the continuity equation, the Euler momentum equations, and the energy equation, which are written as follows:

$$\frac{D\rho}{Dt} = -\rho \boldsymbol{\nabla} \cdot \boldsymbol{u} \tag{1}$$

$$\frac{D\boldsymbol{u}}{Dt} = \boldsymbol{g} - \frac{\boldsymbol{\nabla} p}{\rho} \tag{2}$$

$$\frac{De}{Dt} = \frac{1}{\rho} \boldsymbol{\nabla} \cdot (k \boldsymbol{\nabla} T) - \frac{p}{\rho} (\boldsymbol{\nabla} \cdot \boldsymbol{u}) \tag{3}$$

where $\boldsymbol{u}$, ρ, p, $\boldsymbol{g}$, e, T and k are the velocity vector, density, pressure, gravitational acceleration, internal energy, temperature and thermal conductivity, respectively. The viscous effects are not accounted for the present work since viscous forces are much smaller than inertial forces for the current high-speed SLD impingements.

The fluid is assumed to be weakly compressible and an equation of state is used to relate density to pressure [33]. For multiphase flows, separate equations of state are defined for the liquid and gas phases [34] as:

$$p_l = \frac{c_l^2 \rho_{0l}}{\gamma_l} \left[\left(\frac{\rho_l}{\rho_{0l}} \right)^{\gamma_l} - 1 \right] + p_0 \tag{4}$$

$$p_g = \frac{c_g^2 \rho_{0g}}{\gamma_g} \left[\left(\frac{\rho_g}{\rho_{0g}} \right)^{\gamma_g} - 1 \right] + p_0 \tag{5}$$

where l and g indicate the liquid and gas phases, respectively, p_0 is the background pressure, ρ_0 is the initial density, and γ_l and γ_g are fluid constants and set to 7.0 and 1.4 [34]. c_l is the artificial sound speed in liquid phase given by:

$$\frac{u_{max}}{c_l} \approx 0.1 \tag{6}$$

where u_{max} is the maximum flow speed and c_g is the sound speed in gas phase [34] given by:

$$c_g = \sqrt{c_l^2 \gamma_g \rho_{0l} / (\gamma_l \rho_{0g})} \tag{7}$$

2.2 Multiphase SPH equations

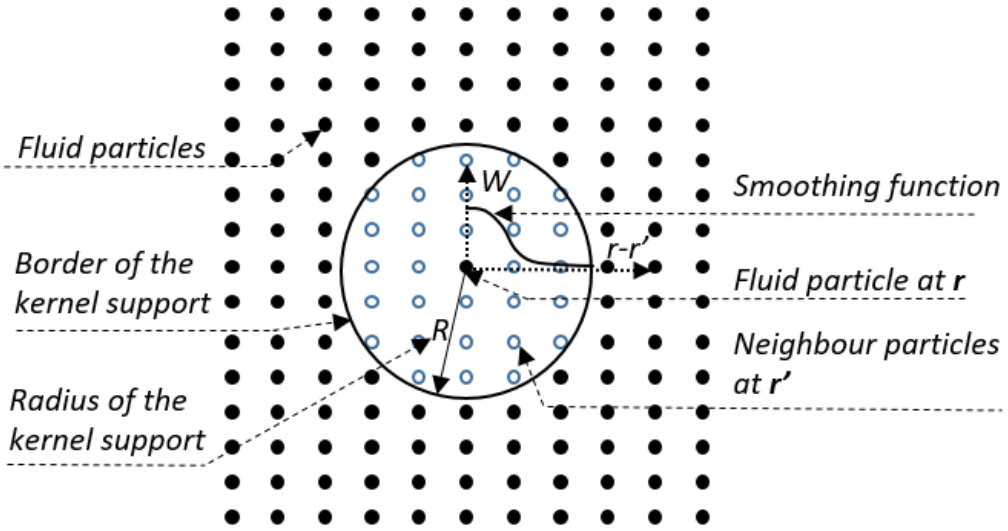

Figure 1. Smoothing kernel.

In SPH, the value of a function, $f(\boldsymbol{r})$, can be represented by an integral as:

$$\langle f(\boldsymbol{r}) \rangle = \int_{\Omega} f(\boldsymbol{r}') W(\boldsymbol{r} - \boldsymbol{r}', h) dV' \tag{8}$$

where $\boldsymbol{r}'$, dV' denote the position and volume of neighbor fluid particles, W is a kernel function and Ω is its support domain. As shown in Figure 1, the kernel is a bell-shaped function that tends to vanish outside its support. h is the characteristic length of the kernel function and equals 1.0001 or 1.3334 times the particle spacing in this work. The kernel support Ω is limited within a sphere

of radius $R = 3h$, the particles within Ω are defined as neighbors while external ones are assumed to have negligible effects on the particle of interest.

According to [62], the interpolation of differential operators of pressure and velocity in Eq. (1-3) can be written as:

$$\langle \boldsymbol{\nabla} \cdot \boldsymbol{u}(\boldsymbol{r}) \rangle = \int_{\Omega} [\boldsymbol{u}(\boldsymbol{r}') - \boldsymbol{u}(\boldsymbol{r})] \cdot \boldsymbol{\nabla} W(\boldsymbol{r} - \boldsymbol{r}', h) dV' \tag{9}$$

$$\langle \boldsymbol{\nabla} p(\boldsymbol{r}) \rangle = \int_{\Omega} [p(\boldsymbol{r}') + p(\boldsymbol{r})] \boldsymbol{\nabla} W(\boldsymbol{r} - \boldsymbol{r}', h) dV' \tag{10}$$

The discretized conduction term is derived in [49], and flow field variables are smoothed using an artificial diffusive term [37] and an artificial viscous term [33]. The discretized multiphase SPH equations can thus be written as:

$$\frac{D\rho_i}{Dt} = -\rho_i \sum_j (\boldsymbol{u}_j - \boldsymbol{u}_i) \cdot \boldsymbol{\nabla} W_{ij} V_j + \delta hc \sum_j \boldsymbol{\Psi}_{ij} \cdot \boldsymbol{\nabla} W_{ij} V_j \tag{11}$$

$$\frac{D\boldsymbol{u}_i}{Dt} = \boldsymbol{g} - \frac{1}{\rho_i} \sum_j (p_j + p_i) \boldsymbol{\nabla} W_{ij} V_j + \alpha hc \sum_j \pi_{ij} \boldsymbol{\nabla} W_{ij} V_j + \frac{1}{\rho_i} \boldsymbol{F}_i^{sf} + \frac{1}{\rho_i} \boldsymbol{F}_i^{adh} \tag{12}$$

$$\frac{D}{Dt}(C_{vi} T_i) = \frac{1}{\rho_i} \sum_j (k_i + k_j)(T_i - T_j) \frac{(\boldsymbol{r}_i - \boldsymbol{r}_j) \cdot \boldsymbol{\nabla} W_{ij} V_j}{|\boldsymbol{r}_i - \boldsymbol{r}_j|^2} - \frac{p_i}{\rho_i} \sum_j (\boldsymbol{u}_j - \boldsymbol{u}_i) \cdot \boldsymbol{\nabla} W_{ij} V_j \tag{13}$$

$$p_i = \frac{c_i^2 \rho_{0i}}{\gamma_i} \left[\left(\frac{\rho_i}{\rho_{0i}} \right)^{\gamma_i} - 1 \right] + p_0 \tag{14}$$

where subscript j denotes the neighbour particles of particle i, V_j is the volume of particle j, C_{vi} is the specific heat of particle i, α and δ are the smoothing coefficients set to 0.1 and 0.3 for maintaining numerical stability, $\boldsymbol{F}_i^{sf}$ denotes the surface tension term, and $\boldsymbol{F}_i^{adh}$ is an artificial adhesion force. The artificial diffusive and viscous terms are given by:

$$\boldsymbol{\Psi}_{ij} = 2(\rho_i - \rho_j)\frac{\boldsymbol{r}_i - \boldsymbol{r}_j}{|\boldsymbol{r}_i - \boldsymbol{r}_j|^2} \tag{15}$$

$$\pi_{ij} = 2(\boldsymbol{u}_i - \boldsymbol{u}_j)\cdot\frac{\boldsymbol{r}_i - \boldsymbol{r}_j}{|\boldsymbol{r}_i - \boldsymbol{r}_j|^2} \tag{16}$$

The diffusive term is applied among particles of the same phase. The Gaussian kernel and its gradients used in the SPH equations can be written as:

$$W_{ij} = \frac{1}{(\pi h^2)^{3/2}} e^{-\frac{(\boldsymbol{r}_i - \boldsymbol{r}_j)^2}{h^2}} \tag{17}$$

$$\boldsymbol{\nabla} W_{ij} = -\frac{2(\boldsymbol{r}_i - \boldsymbol{r}_j)}{h^2} W_{ij} \tag{18}$$

The full framework of this multiphase SPH solver is presented in Figure 2, and the numerical techniques mentioned are explained in detail in following sections.

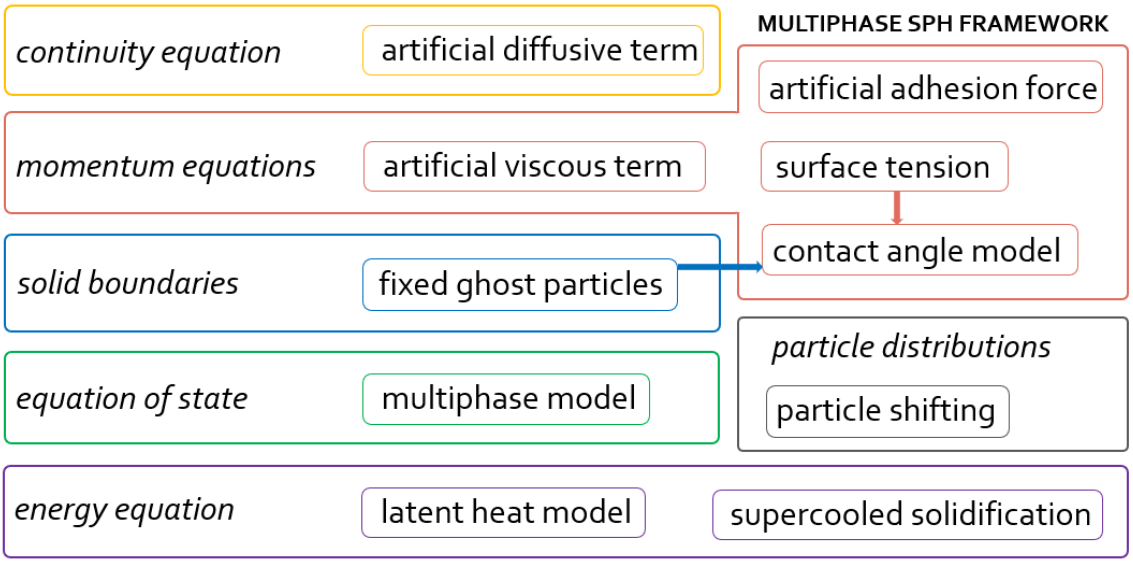

Figure 2. The framework of the multiphase SPH solver.

2.3 Numerical techniques

2.3.1 Surface tension model

The surface tension term proposed in [51] and further developed in [63] is added into the momentum equations as follows:

$$\boldsymbol{F}_i^{sf} = \beta(\boldsymbol{\nabla} \cdot \boldsymbol{n_i})\boldsymbol{\nabla} s_i \tag{19}$$

where β is the surface tension value of water-air interfaces and set to 0.072 N/m, $\boldsymbol{n_i}$ is the unit normal of interface, and $\boldsymbol{\nabla} s_i$ is the gradient of the fluid color and defined as:

$$\boldsymbol{n}_i = \frac{\boldsymbol{\nabla} s_i}{|\boldsymbol{\nabla} s_i|} \tag{20}$$

$$\boldsymbol{\nabla} s_i = \frac{1}{V_i}\sum_j \left(V_i^2 + V_j^2\right)\frac{\left(s_i^i + s_j^i\right)}{2}\boldsymbol{\nabla} W_{ij} \tag{21}$$

where $s_i^i = 0$, and $s_j^i = \frac{2\rho_i}{\rho_i + \rho_j}$. If particles *i* and *j* belong to the same phase, s_j^i is set to zero. The interface curvature can be calculated through:

$$\boldsymbol{\nabla} \cdot \boldsymbol{n_i} = N\frac{\sum_j \left(\boldsymbol{n_i} - \emptyset_j^i\, \boldsymbol{n_j}\right) \cdot \boldsymbol{\nabla} W_{ij} V_j}{\sum_j |\boldsymbol{r_i} - \boldsymbol{r_j}| \cdot |\boldsymbol{\nabla} W_{ij}| V_j} \tag{22}$$

where *N* is the spatial dimension, and $\emptyset_j^i$ is a sign function set to −1 if particles *i* and *j* belong to different phases; otherwise set to 1.

When a portion of fluid tends to splash out of a droplet, it must overcome an adhesion force caused by surface tension, thus converting kinetic energy into surface energy. However, this adhesion force cannot be accurately calculated for sparsely splashing particles, usually single ones, as the interface of a single water particle cannot be precisely constructed in the present continuum surface tension model. Therefore, an artificial adhesion force adapted from an interface sharpness force proposed in [34] is applied to water particles to prevent any unphysical splashing.

$$\boldsymbol{F}_i^{adh} = \frac{\varepsilon}{\Gamma_i^3} \sum_{j \in \text{water}} (\rho_j + \rho_i) \nabla W_{ij} V_j; \text{ for } i \in \text{water} \tag{23}$$

$$\Gamma_i = W_{ii} V_i + \sum_{j \in \text{water}} W_{ij} V_j \tag{24}$$

where ε is a constant coefficient set to 0.02.

2.3.2 Boundary conditions at solid surfaces

The solid boundaries are built using a fixed ghost particle method, as proposed in [41]. In order to offset the kernel support truncation near the solid wall, a layer of fixed ghost particles is placed along the solid surface, as shown in Figure 3. The physical quantities of the fixed ghost particles are mirrored from the interpolation points in the fluid domain.

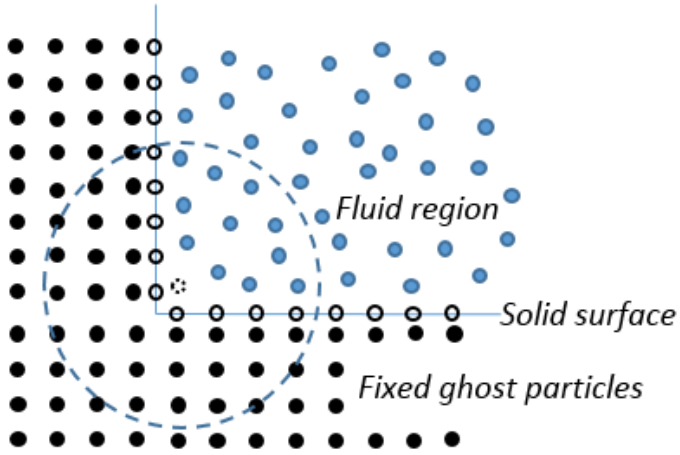

Figure 3. Fixed ghost particles near a solid wall corner.

The physical value f_g of a fixed ghost particle can be interpolated as:

$$f_g = \sum_j f_j W^{MLS}(\boldsymbol{r}_j) V_j \tag{25}$$

where *j* denotes neighbor particles of the counterpart interpolation point of ghost particle *i*, and W^{MLS} can be calculated by:

$$W^{MLS}(\boldsymbol{r}_j) = \boldsymbol{M}_i^{-1}\boldsymbol{e}_1 \cdot \boldsymbol{b}_{ij}W_{ij} \tag{26}$$

$$\boldsymbol{b}_{ij}^T = [1, x_j - x_i, y_j - y_i, z_j - z_i\,] \tag{27}$$

$$\boldsymbol{e}_1^T = [1, 0, 0, 0] \tag{28}$$

$$\boldsymbol{M}_i = \sum_j \boldsymbol{b}_{ij} \otimes \boldsymbol{b}_{ij} W_{ij} V_j \tag{29}$$

where $\otimes$ denotes a tensor product, and (x_i, y_i, z_i) and (x_j, y_j, z_j) are the coordinates of interpolation point *i* and neighbor particle *j*, respectively.

2.3.3 Contact angle model

The wettability of a solid surface can be quantified by contact angles, θ, as shown in Figure 4. Hydrophobic and superhydrophobic surfaces typically have contact angles larger than 90° and 150°, respectively.

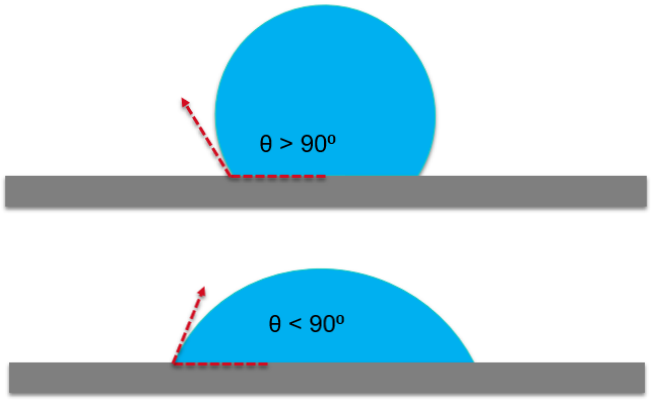

Figure 4. Droplets on surfaces with different contact angles.

A robust contact angle model is proposed based on the continuum surface tension model, and it clarifies the role of the fixed ghost particles in the calculation of surface tension near triple-phase points.

The color function used in the surface tension model is further specified for the fixed ghost particles. At the special contact angles, θ = 0°, 90° and 180°, the definitions of the colors of fixed

ghost particles are straightforward, as shown in Figure 5. They are treated as water color for θ = 0°, and inversely as air color for θ = 180°. As for θ = 90°, the fixed ghost particles near water particles are set to water color, while all others are assigned air color.

Partial colors are introduced for modeling other contact angles, as illustrated in Figure 5. For 0° < θ < 90°, fixed ghost particles near water particles are set to water color, while the rest are given a partial water color. For 180° > θ > 90°, fixed ghost particles near water particles are set to partial air color, and the rest are assigned air color. A coefficient, λ, is added to the color function of the surface tension model to account for partial coloring, as follows:

$$s_i^j = \lambda \frac{2\rho_i}{\rho_i + \rho_j} \tag{30}$$

$$\lambda = \begin{cases} 1 & \text{different color} \\ 0 & \text{same color} \\ 1 - \sin\theta & \text{partial different color} \\ \sin\theta & \text{partial same color} \end{cases} \tag{31}$$

During the implementation of this model, it has been found that an unphysical force could be generated when the water film is thinner than the radius of the kernel domain, as shown in Figure 6. To avoid such problems, the fixed ghost particles are treated as water color instead of partial color when calculating the interface normal for fluid particles away from the triple-phase points. Particles that have at least a neighbour air particle close to solid surfaces (distance being less than 0.75h) are considered to be near triple-phase points and then allowed to use the partial colors to calculate their interface normal.

In the surface tension model, the interface curvature of particle i is evaluated using the divergence of the interface normal, $\boldsymbol{\nabla \cdot n_i}$. As illustrated in Figure 7, the normal of the fixed ghost particles near the triple-phase point is enforced to the desired contact angle, thus avoiding truncated kernel supports while computing $\boldsymbol{\nabla \cdot n_i}$. The difference between the interface normal of fluid

particles and fixed ghost particles can result in larger $|\nabla \cdot \boldsymbol{n_i}|$, thus guiding the triple-phase interface approaching the desired contact angle.

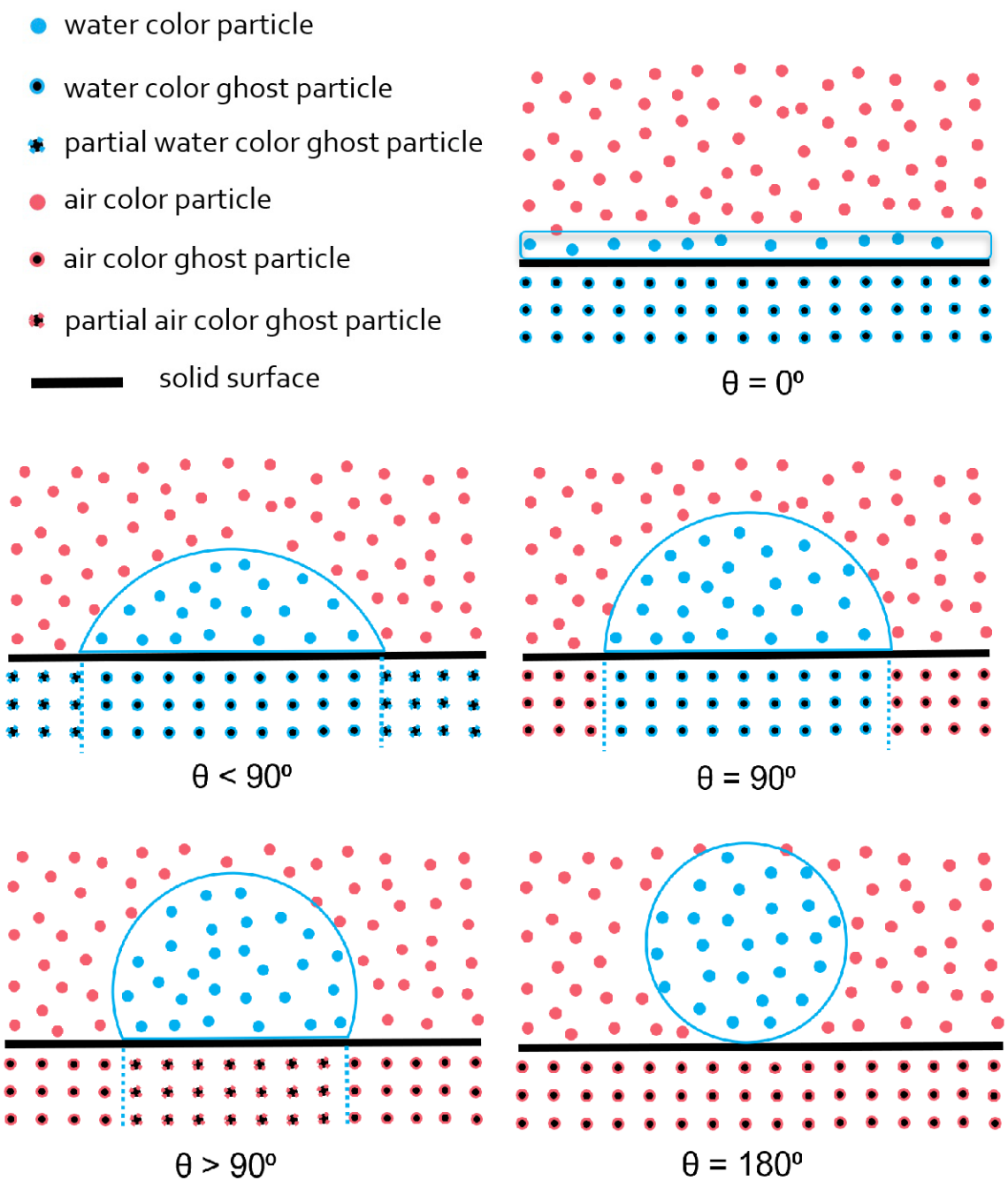

Figure 5. Different colors are assigned to fixed ghost particles at various contact angles.

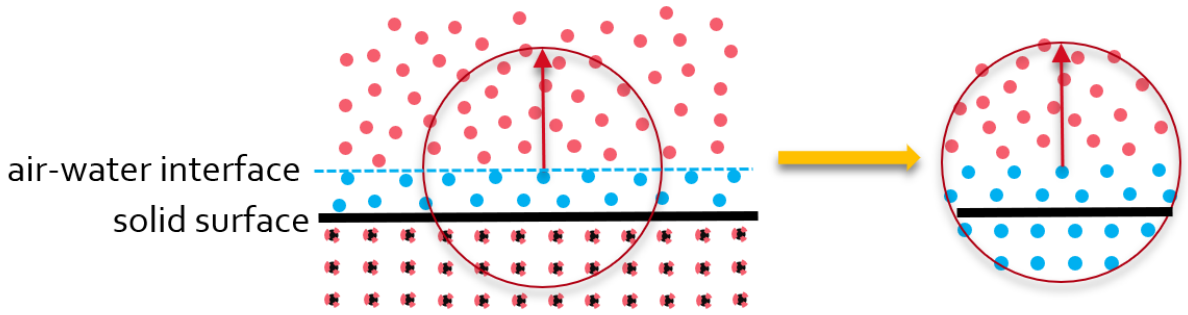

Figure 6. The corrected color of fixed ghost particles when the air-water interface is away from triple-phase points.

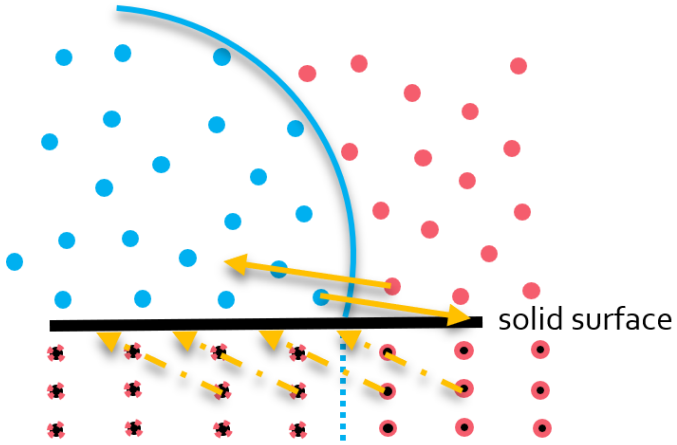

Figure 7. Normal corrections to fixed ghost particles when triple-phase points are in their kernel support domains.

2.3.4 Particle shifting technique

In SPH, isotropic particle spatial distribution is crucial for accurate integral interpolations. However, it is difficult to guarantee this property, especially in zones exhibiting high velocity gradients [64]. High-speed droplet impingements are characterized by strong flow advection and large interface deformations. Hence, the simulations are usually accompanied by anisotropic particle distributions. This problem can be significantly alleviated by the particle shifting algorithm [39]:

$$\delta r_i = -CFL \cdot Ma \cdot (2h)^2 \sum_j \nabla W_{ij} \frac{m_j}{\rho_j} \tag{32}$$

$$r_i^* = r_i + \delta r_i \tag{33}$$

where δr_i is the shifting distance, r_i^* is the new particle position, *CFL* represents the Courant–Friedrichs–Lewy number to control the time step size, and *Ma* is the Mach number.

2.3.5 Latent heat model and ice fraction

SPH can model complex multiphase physics in a simple way, thus making it a suitable approach to represent the solidification of SLD. As shown in Figure 8, a latent heat container with a capacity *mL* (where *L* is the specific latent heat of water and *m* is the mass of a water particle) is used to collect the heat loss, Q^{Loss}, of the particles at freezing. The freezing particles can be interpreted as water-ice mixture particles and the ice fraction is defined as $f_{\mathrm{ice}} = Q^{\mathrm{Loss}}/mL$. As the latent heat container gets filled by the cumulative heat loss ($Q^{\mathrm{Loss}} = mL$), the particle turns into an ice particle and its physical properties, such as thermal conductivity and specific heat, are then changed.

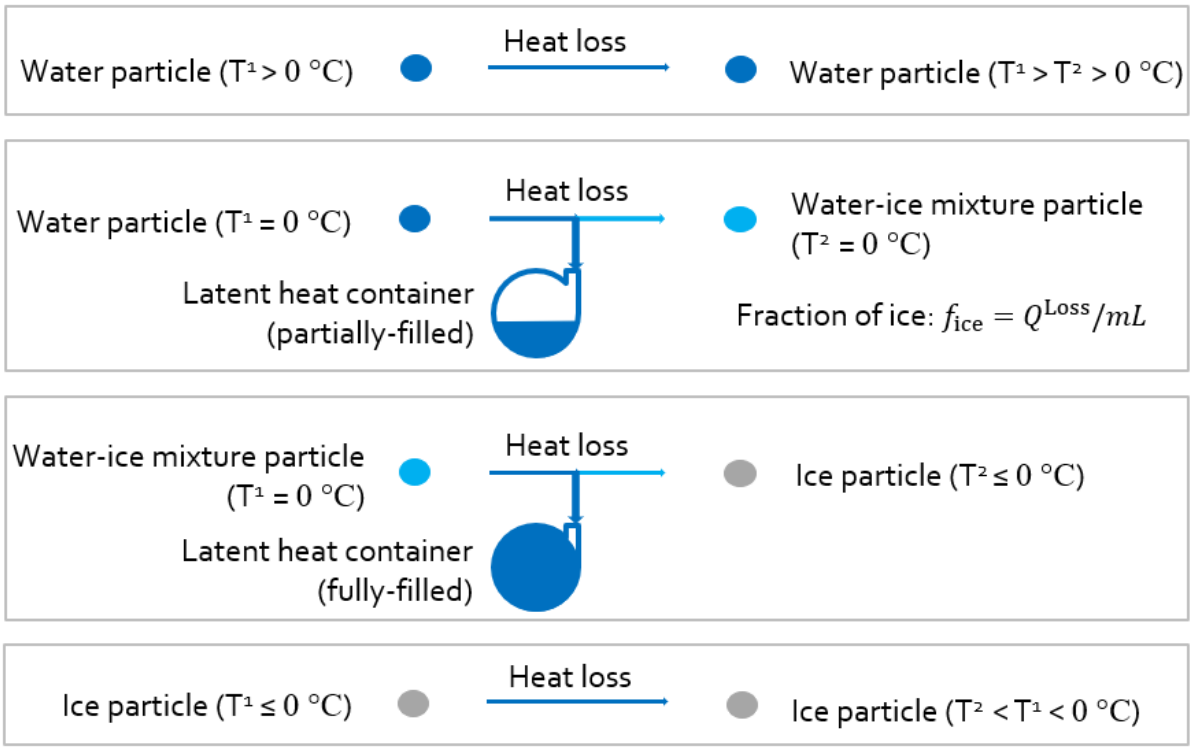

Figure 8. Latent heat model for particles at freezing temperature.

2.3.6 Supercooled solidification model

Supercooled solidification has three stages: initial nucleation, dendritic freezing, and quasi-isothermal solidification [65]. Because the current work focuses on SLD impinging on ice surfaces, it is assumed that the dendritic freezing starts immediately upon contacting an ice surface. A supercooled solidification model using the experimentally measured propagating speeds [17, 66], as shown in Figure 9, is proposed to represent the dendrite growth.

When an ice particle or ice boundary particle appears in the kernel domain of a supercooled particle i ($T_i < -4$ °C), the supercooled particle is activated to grow dendrite as shown in Figure 10. The dendrite growing speed of a supercooled particle i used in the simulations is a simple regression of the experimental data [17, 66] and is given by:

$$U(T_i) = 1.5((T_f - T_i)/20)^2 \tag{34}$$

where T_f is the freezing temperature, 0 °C. The dendrite length of a supercooled particle, S_d, is calculated as follows:

$$S_d = S_{d0} + U(T_i)dt \tag{35}$$

When S_d is less than or equal to the minimum distance between the supercooled water particle and an ice particle, the supercooled particle freezes and instantly releases its residual latent heat to its neighbour supercooled particles ($T_j < -4$ °C), as shown in Figure 10. The temperature increase of neighbor particles is then calculated by:

$$\Delta T_j = (L + C_{\mathrm{v}i}(T_i - T_f))W_{ij}V_j/(C_{\mathrm{v}j}\Gamma_i);\ \text{if } \Gamma_i > 0.15 \tag{36}$$

$$\Gamma_i = \sum_{j \in T_j < -4\ ^\circ\mathrm{C}} W_{ij}V_j \tag{37}$$

where C_{v} is the specific heat, W_{ij} is the value of kernel function, and L is the specific latent heat. It is worth noting that all water and ice particles have the same mass in the simulations. If the distance between the newly frozen particle and the ice boundary particle or a fixed ice particle is smaller than an initial particle spacing, the new ice particle is frozen in place. Otherwise, it remains a free ice particle moving with the fluid flow until the abovementioned distance criterion is satisfied.

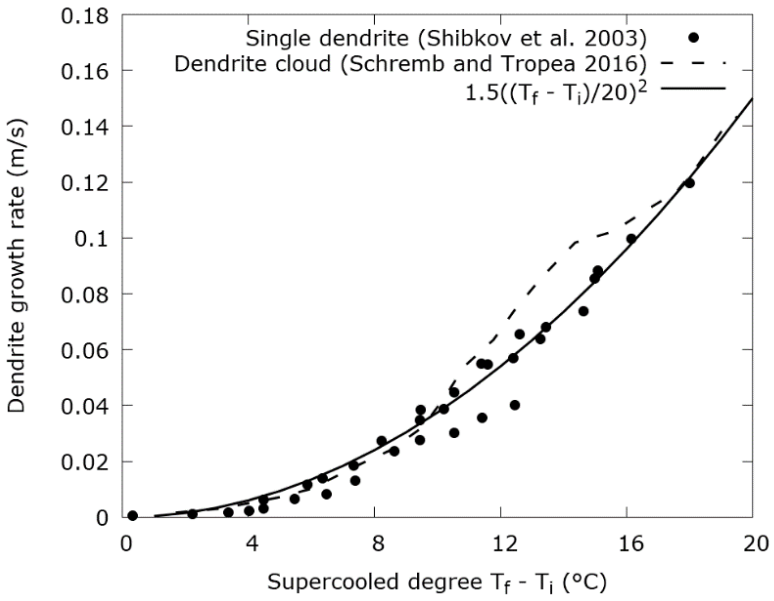

Figure 9. Dendrite growth speeds measured in experiments and used in simulations.

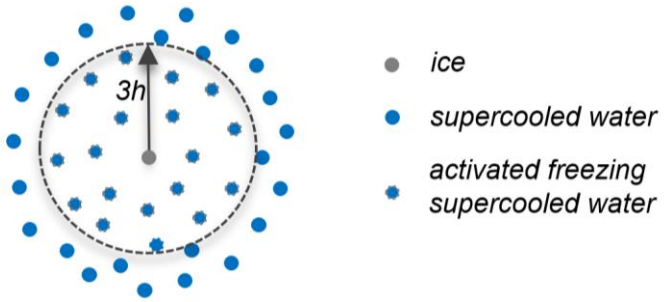

(a). An ice particle activates neighbor supercooled particles' dendrite growth.

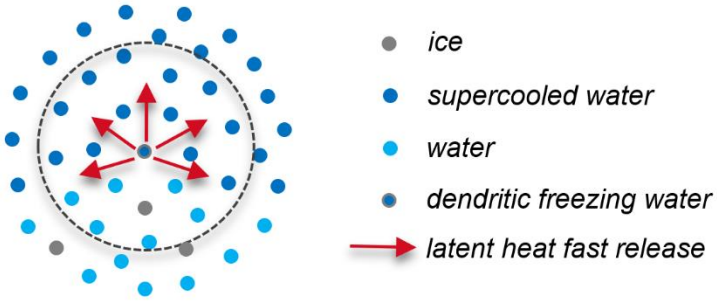

(b). A dendritic freezing particle releases its latent heat to neighbors instantly.

Figure 10. Supercooled solidification model.

2.4 MPI parallelization

2.4.1 A cell system and neighbor searching

SPH uses moving particles to represent fluid flows, and the interpolations are performed through integrals over neighbor particles. The dynamical neighbor list, being the base of SPH computations, is the main barrier to efficient MPI parallelization on a distributed-memory architecture.

A cell system is used to perform neighbor searching, data communications and particle re-indexing. The computational domain is divided into spatially fixed cubic cells with a constant side length equal to the radius of the kernel support domain, $3h$. The total number and list of the particles in each cell are calculated from the particle positions. A particle in cell (i, j, k) can find all its neighbor particles from the 27 adjacent cells from $(i-1, j-1, k-1)$ to $(i+1, j+1, k+1)$, as illustrated in Figure 11. As these cells can belong to different subdomains, it is necessary to collect the particles from the cells along the communication interface in adjacent subdomains through MPI communication, as shown in Figure 12. The cells and particles collected from the adjacent subdomains are henceforth labeled guest cells/particles, and the original ones within subdomains are labeled host cells/particles.

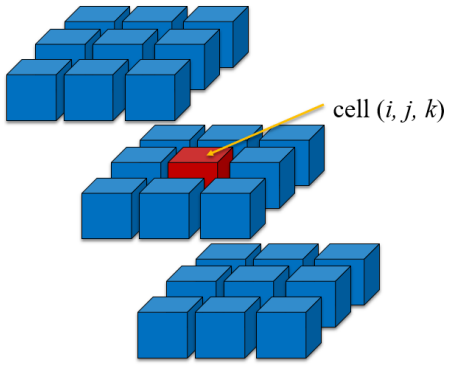

Figure 11. All neighbors of particles in cell (i, j, k) distribute in 27 adjacent cells.

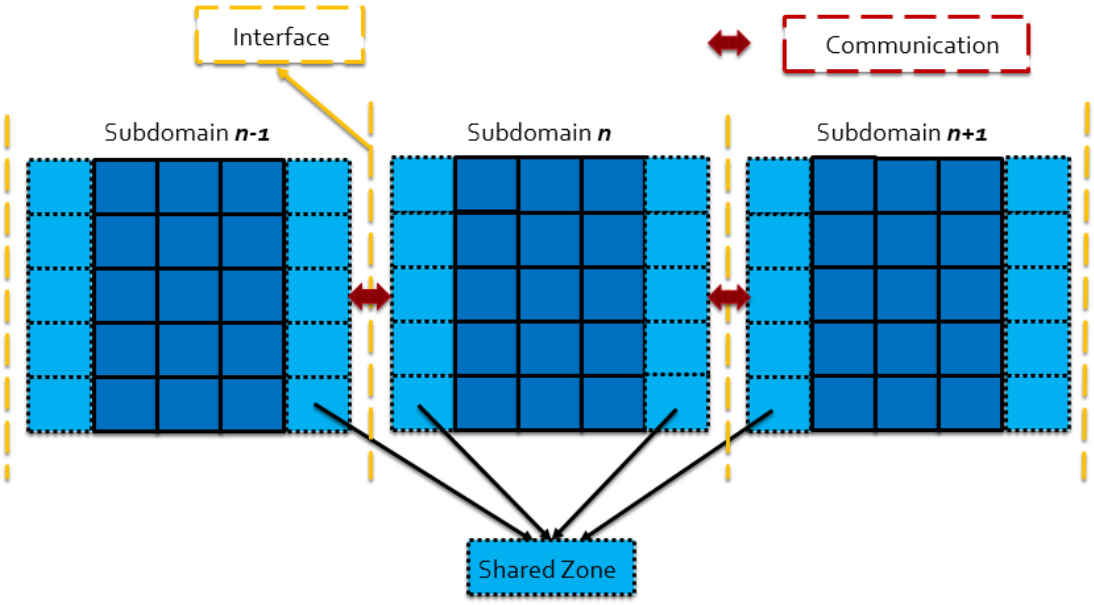

Figure 12. The shared zones are the cells along the communication interfaces.

2.4.2 3D partitioning

In a distributed-memory architecture, the computational domain is partitioned into *N* spatially fixed subdomains that are assigned to *N* processors. The particles of each subdomain are stored in the local memory and shared to adjacent processors as necessary. Because the computational domain is fully filled with air and water particles, the computing loads on each processor are balanced automatically if the subdomains have the same volume.

The current work uses 3D partitioning to perform massively parallel computing and to improve parallelization efficiency. 1D partitioning is straightforward but faces limitations, since the subdomain requires a minimum thickness of one cell, as shown in Figure 12. When splitting a cubic domain of 1 m^3 into eight subdomains, 3D partitioning can effectively decrease communication interfaces area from 7 m^2 in 1D and 4 m^2 in 2D to 3 m^2, as illustrated in Figure 13.

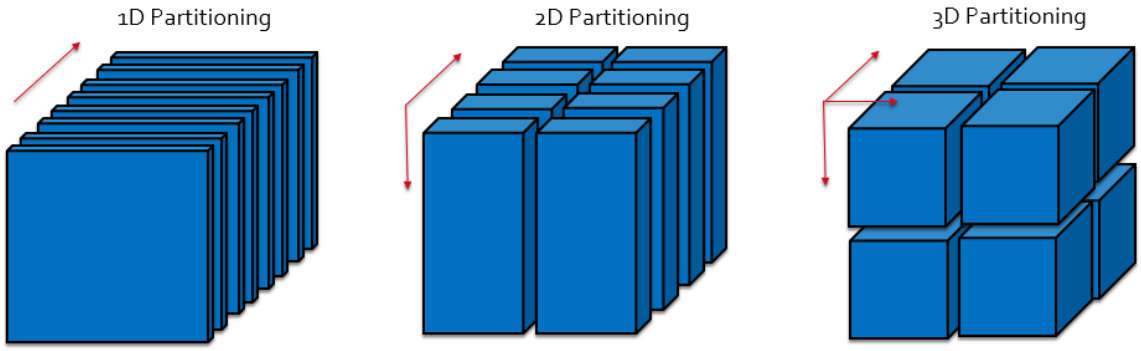

Figure 13. 1D, 2D and 3D partitioning strategies for a cubic domain on 8 processors.

2.4.3 The sequence of collecting particles

In 3D partitioning, a subdomain has to share data with up to 26 adjacent subdomains. A sequential collecting particles strategy is used to decrease the number of communicating directions from 26 to 6, as shown in Figure 14. At first, the particles of adjacent subdomains in the *x*-direction are collected. Then, the particles including the guest particles received from the *x*-direction are collected from the *y*-direction. Similarly, for the *z*-direction, all the particles along the communication interface including these received in the last two steps are collected. The host and guest particles from different directions are stored at separate sections in an array.

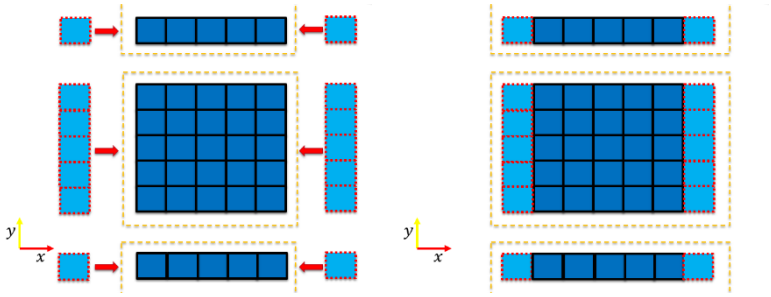

(a). *x*-axis communication.

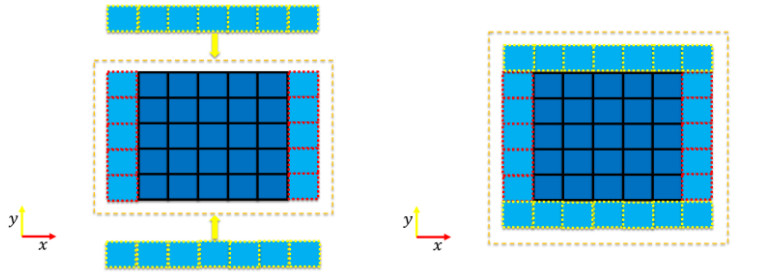

(b). *y*-axis communication.

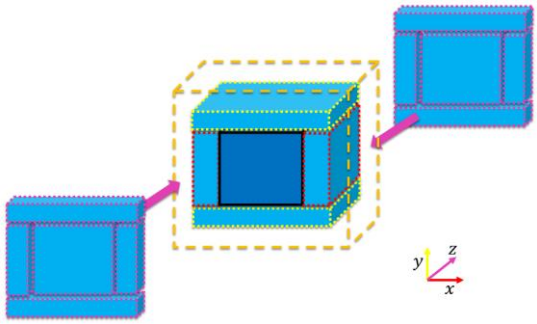

(c). *z*-axis communication.

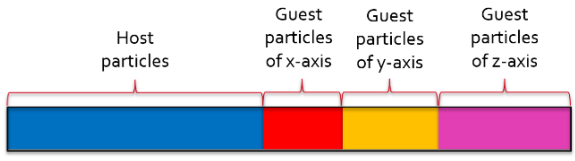

(d). Storing host and guest particles in an array.

Figure 14. The sequence of data communication.

2.4.4 Re-indexing particles

Removing and inserting particles in a distributed-memory architecture can easily cause allocation problems, hence, a re-indexing technique is introduced to accommodate migrating particles.

In SPH simulations, some particles can migrate out of the subdomain as shown in Figure 15. These migrating particles are sent to the intended subdomains along with the other shared particles. The lists of particles for both host and guest cells are re-calculated according to their latest positions, thus making the migrating particles registered in their new cells. Particles are re-indexed through looping over the particle lists of the cells in the subdomain, and moving-in particles are thus stored as host particles and moving-out particles become guest particles.

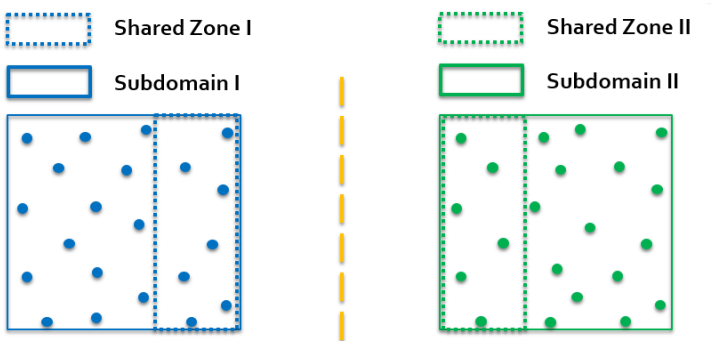

(a). Initial particle position

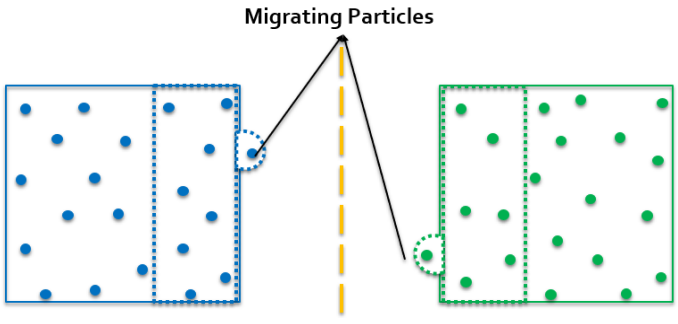

(b). Particle position after movement

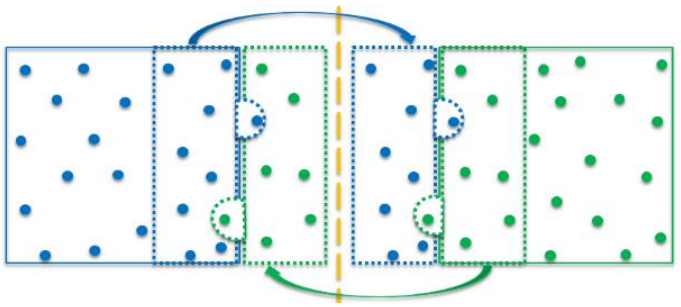

(c). Sharing particles

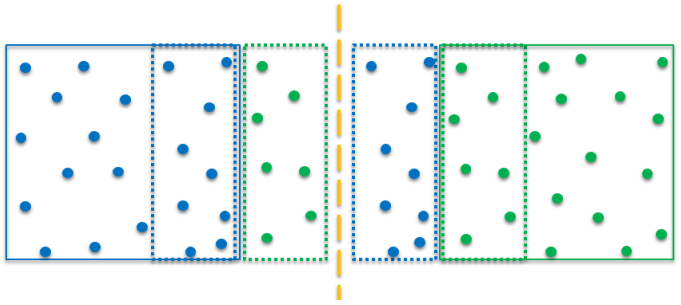

(d). Re-indexing particles by looping all cells

Figure 15. Re-indexing technique to accommodate migrating particles.

2.4.5 Parallel efficiency

To investigate the scalability of the code, a test with 110 million particles is conducted for 50 time steps on 32 to 1024 cores (Intel Gold 6148 Processor 2.4 GHz). The cell system has a size of $(160 \times 160 \times 160)$, and each cell initially has 27 particles. Ten repetition tests are carried out, and the CPU computing times are recorded and averaged.

The parallelization speed-up ($S = N_0 T_{N_0}/T_N$) and efficiency ($\eta = N_0 T_{N_0}/NT_N$) are shown in Table 1 and plotted in Figures 16-17, where N_0 is set to 32. The results show a linear speed-up close to the ideal one, and good parallelization efficiencies are obtained even on a large number of cores.

Cores	32	64	128	256	512	1024
CPU computing time (s)	3743	2011	986.1	501.0	253.1	128.8
Speed-up	32	59.6	121.5	239.1	473.3	930.0
Efficiency (%)	100	93.1	94.9	93.4	92.4	90.8

Table 1. CPU computing time, parallelization speed-up and efficiency of the solver to compute 110 million particles for 50 time steps on 32 to 1024 cores.

The effects of particle load on computing speeds are also investigated by conducting a series of tests with various particles numbers ranging from 1,728 to 1,481,544 on each of the 64 cores (Intel E5-2650 v4 Processor 2.2 GHz). The number of particles processed for a time step in one computing second is presented in Figure 18, showing that 100,000 or more particles on each processor can guarantee a good computing efficiency.

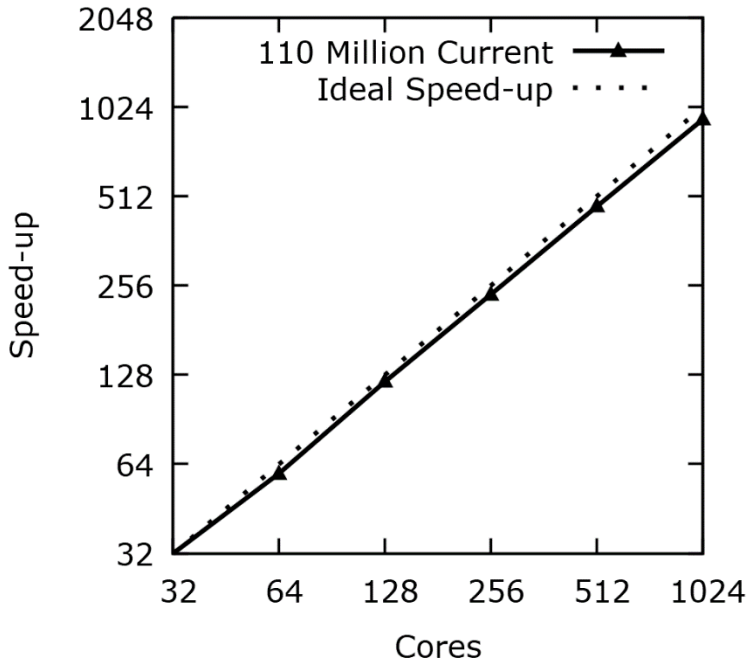

Figure 16. Solver speed-up to compute 110 million particles for 50 time steps on 32 to 1024 cores.

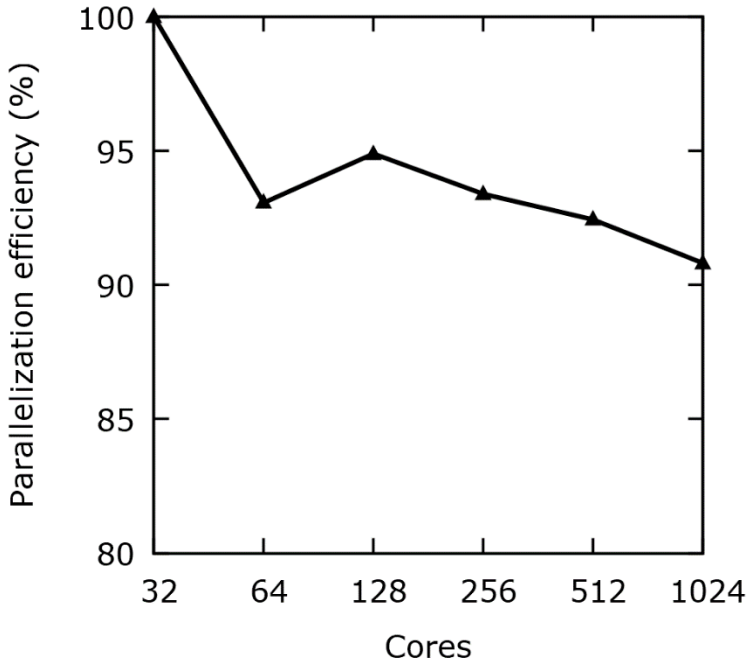

Figure 17. Solver parallelization efficiency to compute 110 million particles for 50 time steps on 32 to 1024 cores.

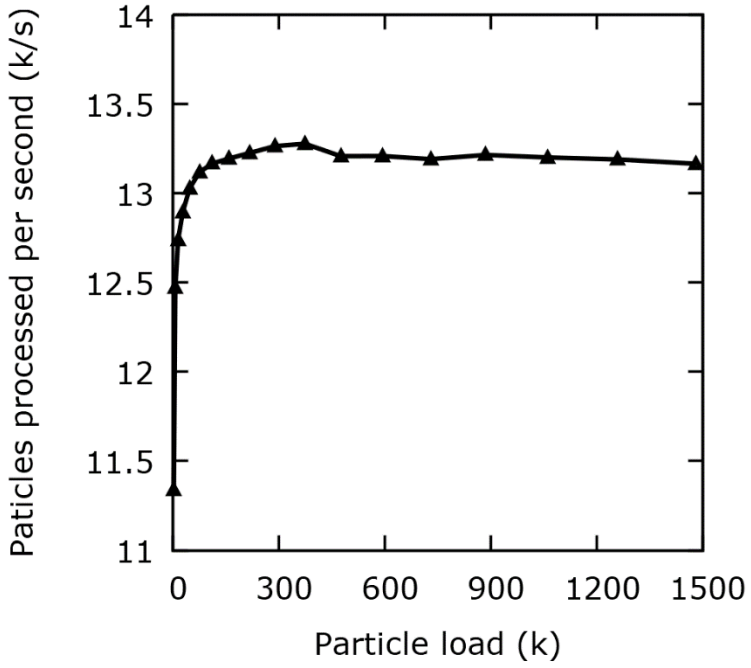

Figure 18. Effects of particle load on computing efficiency with 64 cores.

CHAPTER 3 RESULTS

3.1 Droplet impingement on a water film

The solver is first validated against experimental results of a low-speed droplet impingement on a water film. It is then applied to impingement at aeronautical speeds, and post-impact water crowns are investigated for different droplet diameters, impact speeds, impact angles, and film thicknesses.

3.1.1 Validation: a droplet impinging on a water film at low speed

According to the experiment of [67], a droplet of 3.82 mm is launched towards a water film of 0.67D at a speed of 3.94 m/s, as shown in Figure 19.

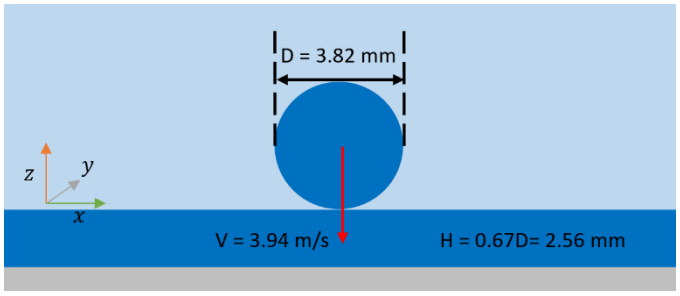

Figure 19. Sketch of a low-speed droplet impinging on a water film.

In the simulation, the size of the computational domain is set to (8D × 8D × 4D), as a compromise between wall constraint effects and computational cost. The particle spacing is set to D/26, and the computational domain is filled with 4.6 million fluid particles. At the initial time instance, the air particles are at rest and the droplet is lying above the water film. As shown in Figure 20, the top external diameter is measured as crown diameter without the free rim and outward jets, and the crown height is measured from the still water film surface.

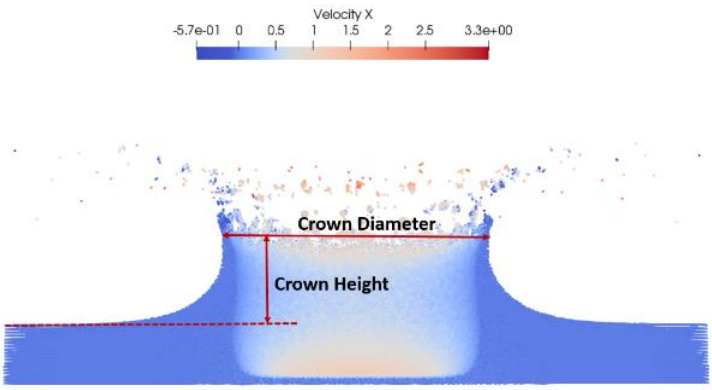

Figure 20. Measurements of the post-impact water crown diameter and height.

The effects of surface tension are investigated by repeating the simulation with no surface tension, and the water crowns are compared in Figure 21. It is found that surface tension results in larger secondary droplets for low-speed impingements.

Defining a non-dimensional time as $t^* = t/(D/V)$, where D and V are the initial diameter and velocity of the droplet, the time history of crown diameters and heights are compared to experimental data in Figures 22-23, showing good qualitative agreement.

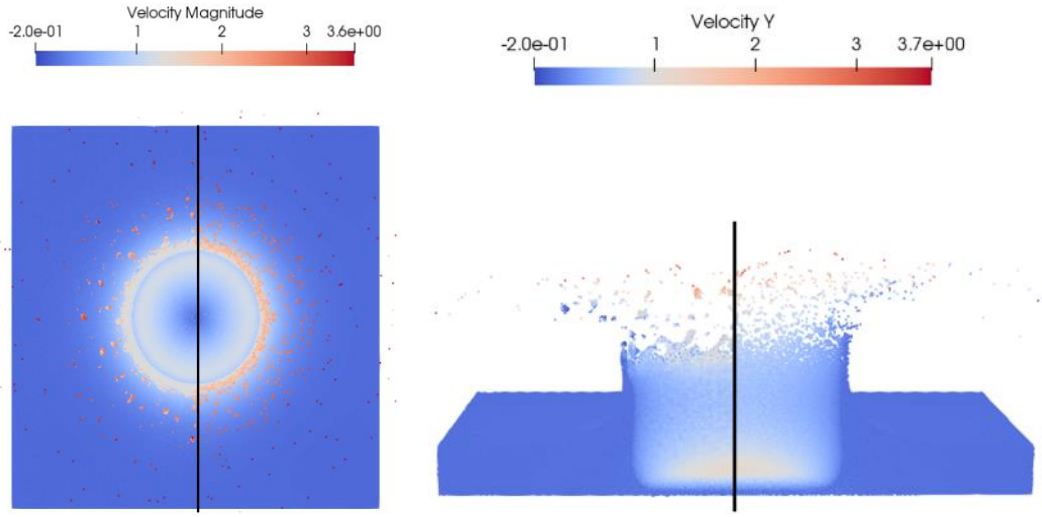

Figure 21. Top and side views of the water crown accounting for surface tension (left half) and neglecting surface tension (right half).
D = 3.82 mm, V = 3.94 m/s, H = 0.67D.

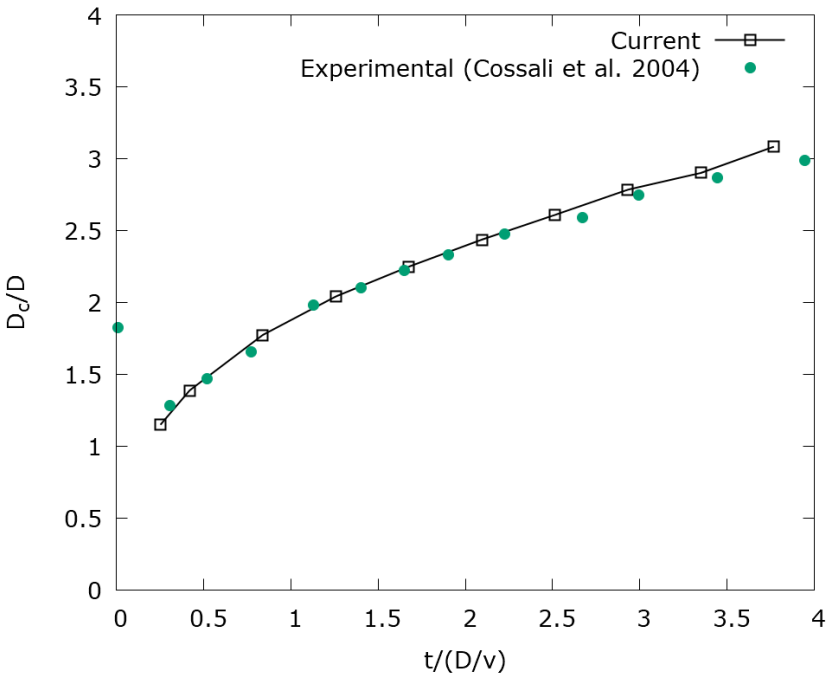

Figure 22. Non-dimensional time history of the post-impact water crown diameters. D = 3.82 mm, V = 3.94 m/s, H = 0.67D.

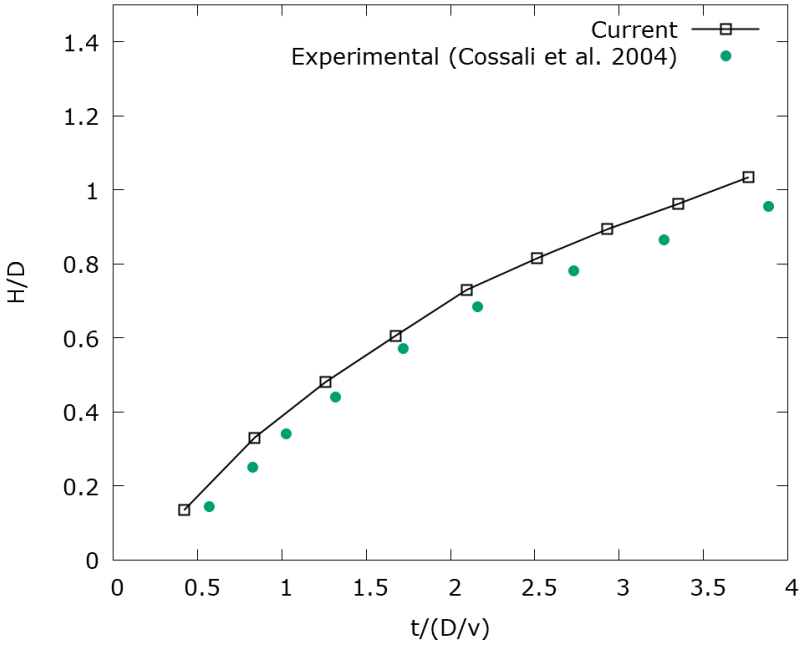

Figure 23. Non-dimensional time history of the post-impact water crown heights. D = 3.82 mm, V = 3.94 m/s, H = 0.67D.

3.1.2 A droplet impinging on a water film at high speed (aeronautical speed)

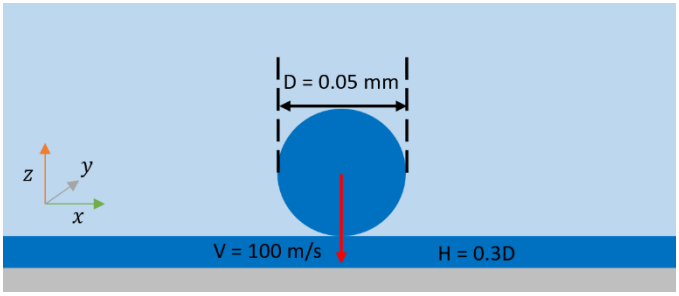

Figure 24. Sketch of a droplet impinging on a water film at an aeronautical speed.

The solver is applied to droplet impingement at high speeds, typical of aeronautical situations. In the simulation, a droplet with a diameter of 0.05 mm impinging on a film with a thickness 0.3D at an approach speed of 100 m/s is modeled. The computational domain is set to (8D × 8D × 4D). In order to investigate the effects of particle resolution, four particle spacings (D/26, D/35, D/44 and D/50) are used to generate 5 million, 11 million, 22 million and 31 million particles. Figure 25 presents the water crowns at t* = 2.23, and their profiles are plotted in Figure 26. The time history of crown diameters is compared in Figure 27, showing that increasing the number of particles from 5 million to 22 million results in an increase in the crown height and diameter. Noting that 22 million and 31 million particle cases lead to similar results, the following cases use 22 million particles to implement the simulations. Figure 28 shows top- and side-view snapshots of the water crown at different time instances.

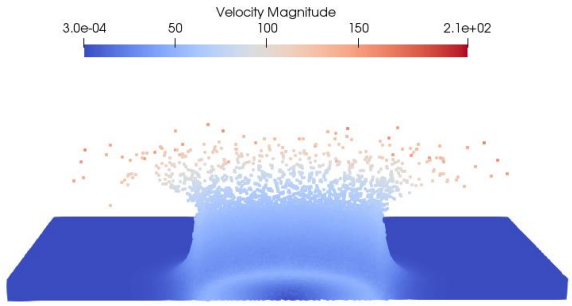

(a) 5 million

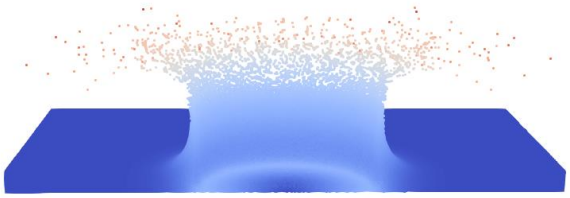

(b) 11 million

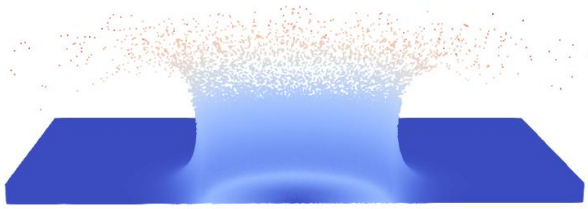

(c) 22 million

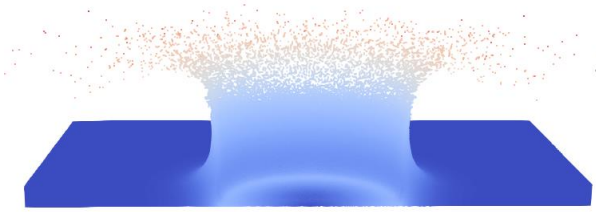

(d) 31 million

Figure 25. Snapshots of the water crown at t* = 2.23 with different total numbers of particles. D = 0.05 mm, V = 100 m/s, H = 0.3D.

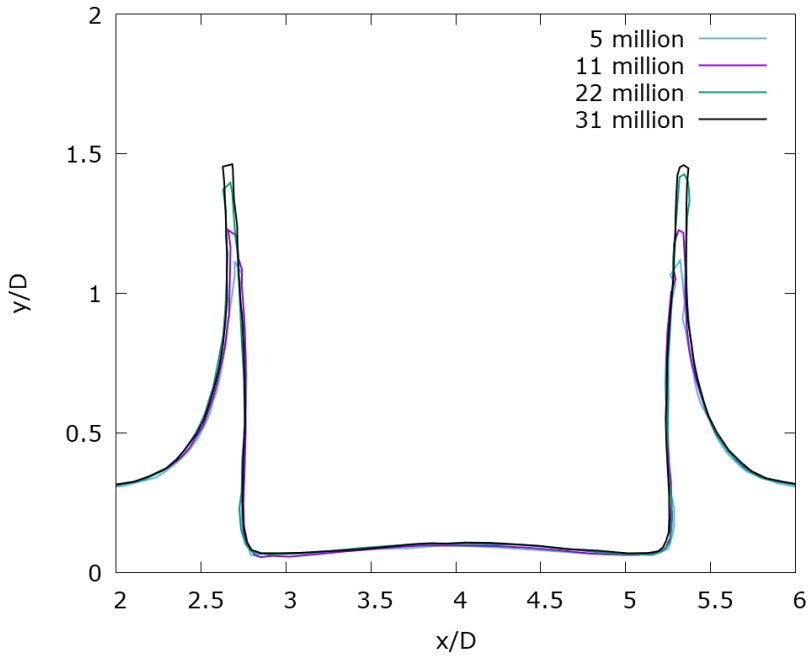

Figure 26. The crown profiles at t* = 2.23 with different total numbers of particles. D = 0.05 mm, V = 100 m/s, H = 0.3D.

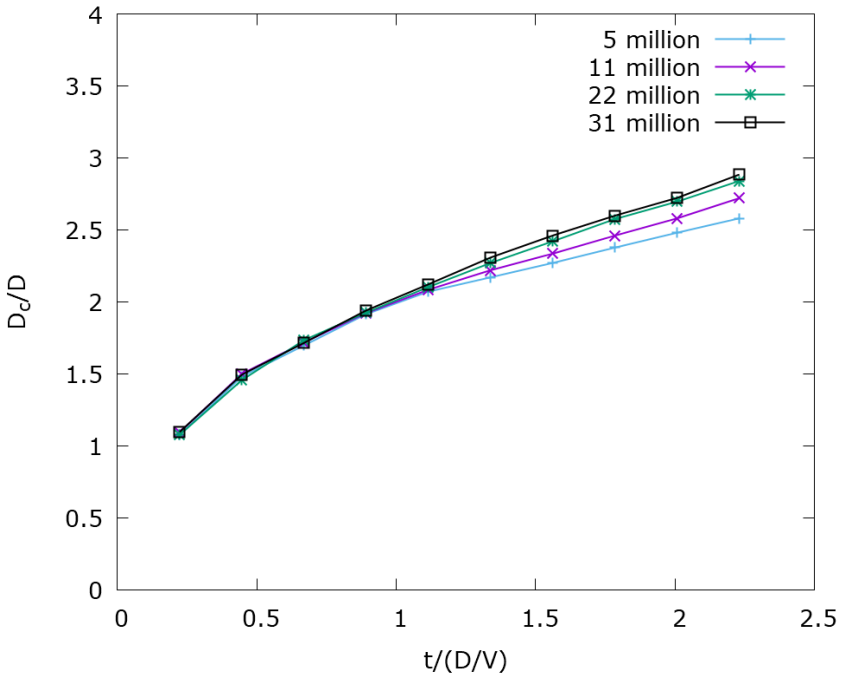

Figure 27. The time history of the crown diameters with different total numbers of particles. D = 0.05 mm, V = 100 m/s, H = 0.3D.

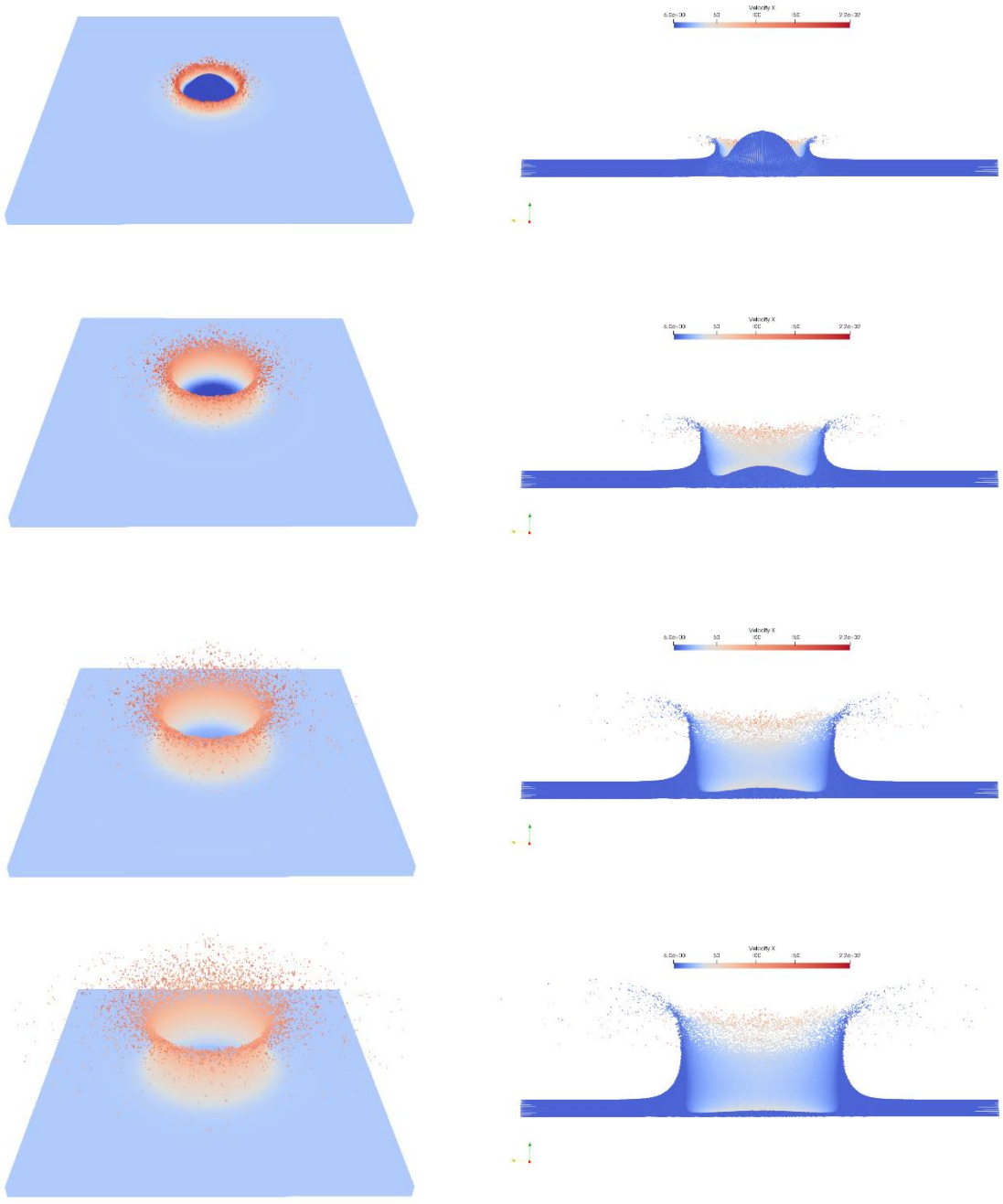

(a) Top view (b) Side view

Figure 28. Snapshots of the droplet impingement at aeronautical speed at t* = 0.55, 1.11, 1.67 and 2.23 (top to bottom).
D = 0.05 mm, V = 100 m/s, H = 0.3D.

3.1.3 A study of the effects of water thickness

In order to study the effects of water film thickness, three different film thicknesses are used: 0.075D, 0.15D and 0.3D. The droplet diameter is set to 0.05 mm and the initial speed to 100 m/s. The computational domain is set to (8D × 8D × 4D) and the particle spacing to D/44, generating 22 million fluid particles.

Snapshots of the water crown at t* = 0.89 and 1.67 for various water film thicknesses are shown in Figure 29. The crown profiles at these time instances are compared in Figure 30, with the origin placed on the air-water interface of the film for clarity. The time history of the crown diameters is further plotted in Figure 31. As the water film thickness is decreasing, the crown diameter increases, and the fully developed crown presents a shallower internal base.

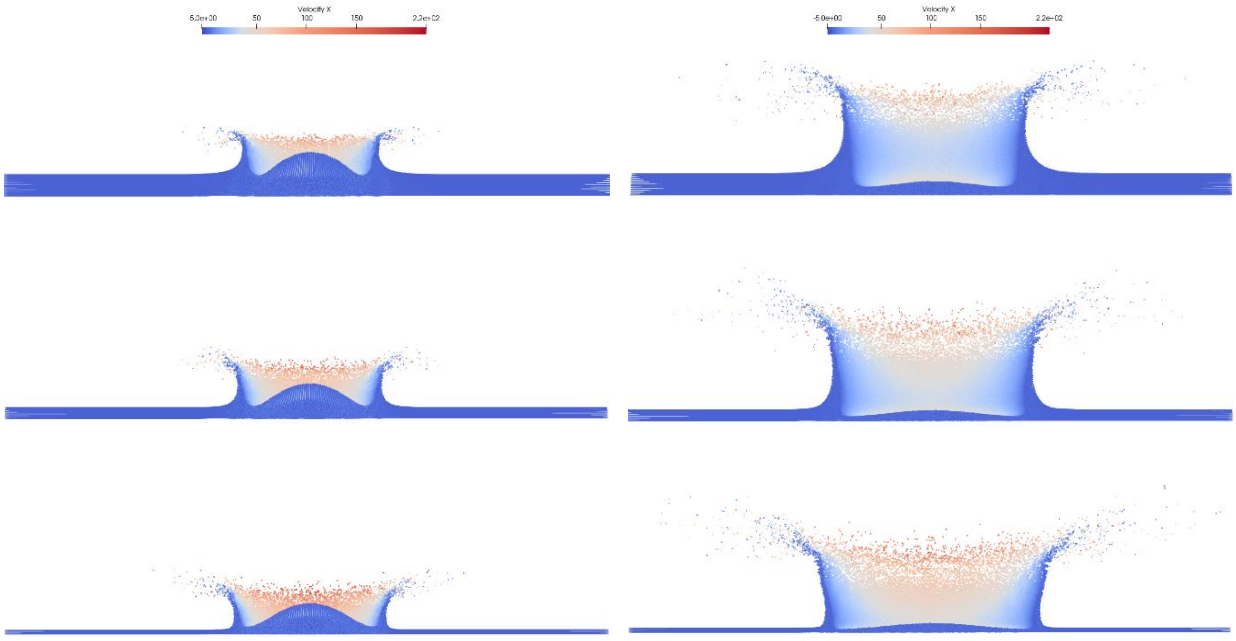

(a) t* = 0.89 (b) t* = 1.67

Figure 29. Water crown on different water film thicknesses.
H = 0.300D, 0.150D and 0.075D (top to bottom), D = 0.05 mm, V = 100 m/s.

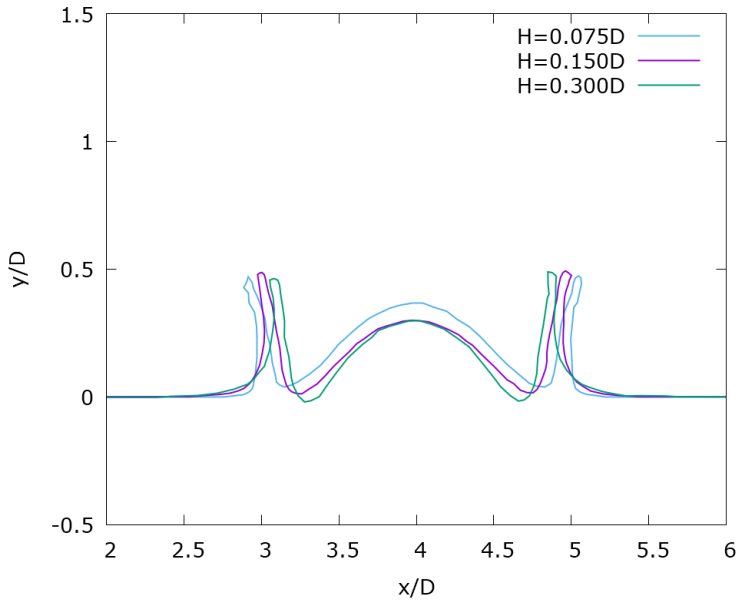

(a) t* = 0.89

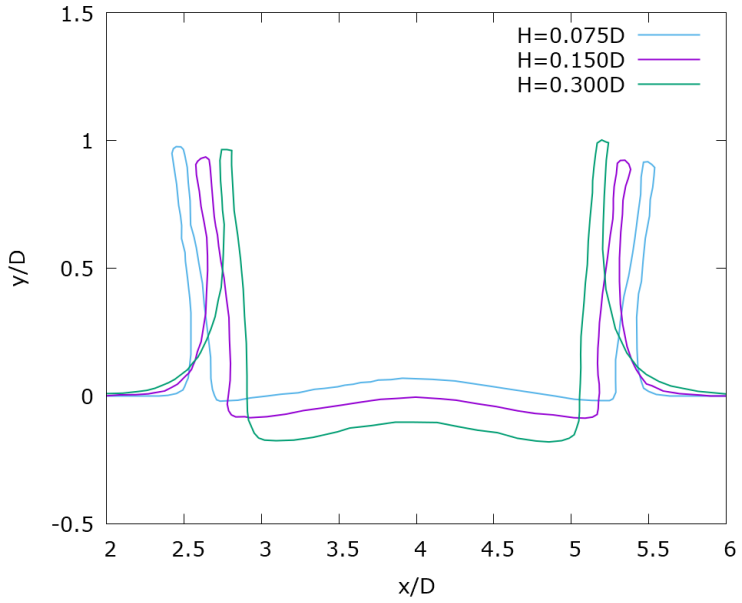

(b) t* = 1.67

Figure 30. Profiles of the cross-section of the water crown with various water film thicknesses. D = 0.05 mm, V = 100 m/s.

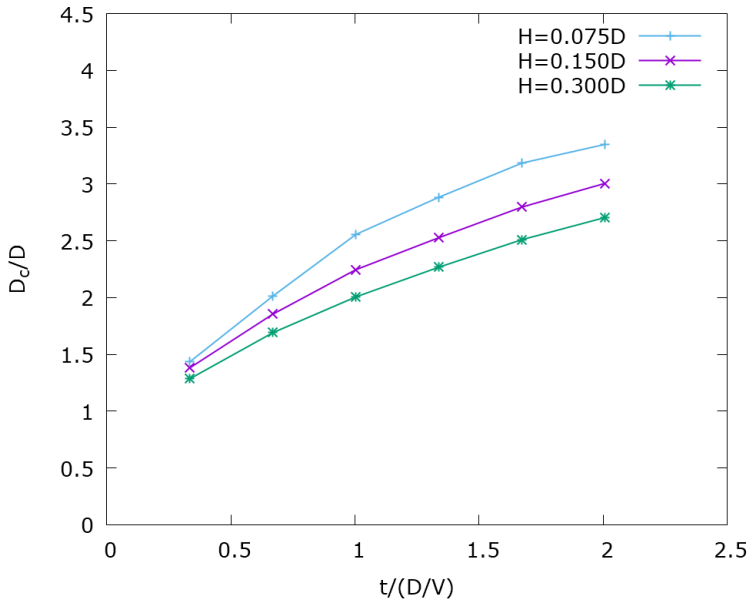

Figure 31.Time history of the crown dimeters with various water film thicknesses.
D = 0.05 mm, V = 100 m/s.

3.1.4 A study of the effects of impact angle

Oblique droplet impingements at aeronautical speeds are conducted with three impact angles: 30°, 45° and 60°. The droplet diameter is set to 0.05 mm, the initial speed to 100 m/s, and the water film thickness to 0.15D, as shown in Figure 32.

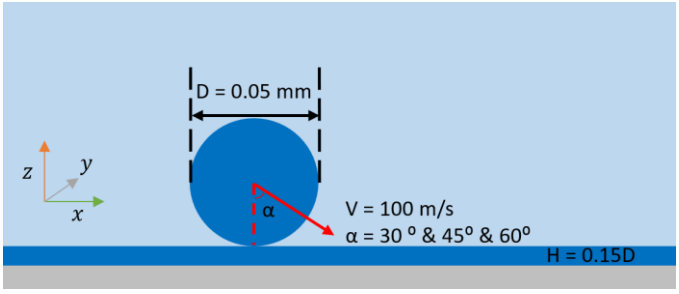

Figure 32. Sketch of oblique impingements on a water film.

The computational domain is set to (10D × 8D × 4D) and the particle spacing to D/44, using 26 million fluid particles. The snapshots of the oblique impingements at different angles are shown

in Figures 33. It is found that a vertical trajectory dominates the splashing movement at 30°, while a clear down-forward trend is observed in the case of 45°. At 60°, the horizontal motion along the water film results in a Kelvin-Helmholtz instability suppressing the forward or upward splashing, and this was also reported by [27] under similar conditions.

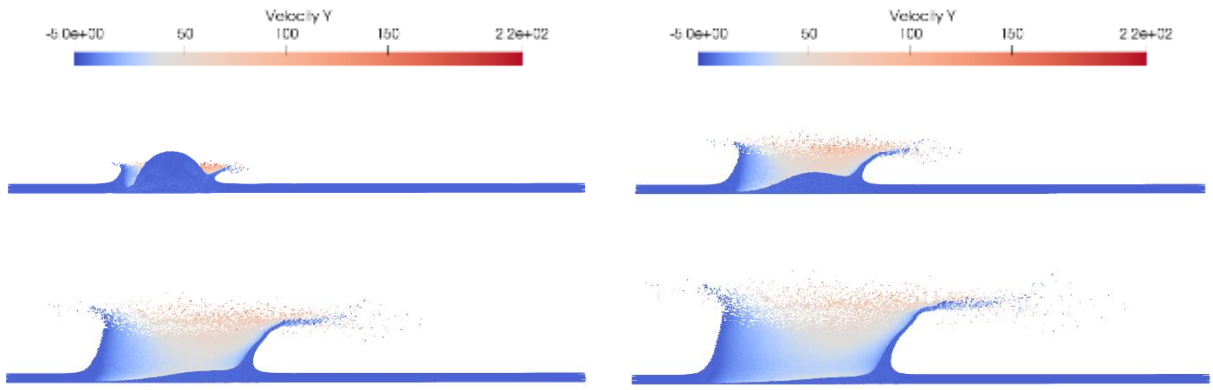

(a) 30°

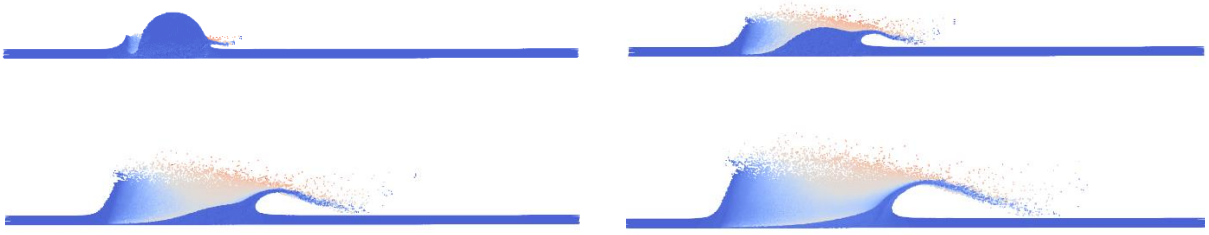

(b) 45°

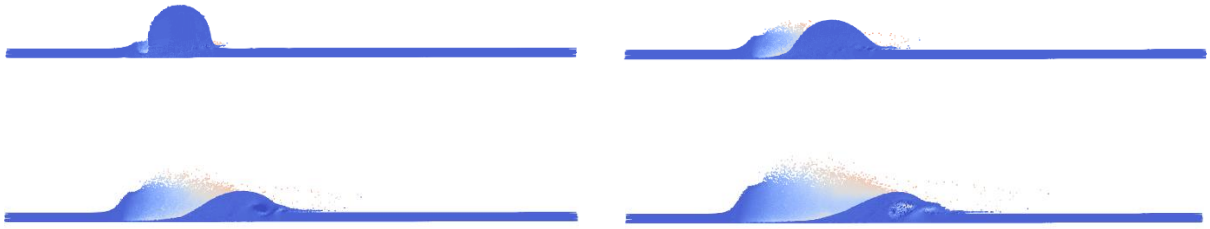

(c) 60°

Figure 33. Snapshots of oblique droplet impingement with various impact angles at t* = 0.55, 1.11, 1.67 and 2.23.
D = 0.05 mm, V = 100 m/s, H = 0.15D.

3.1.5 A study of the effects of droplet speed

The effects of the droplet speed are studied by simulating a 0.5 mm droplet impinging on a thin water film of 0.012 mm thickness at speeds of 10 m/s and 100 m/s, as shown in Figure 34. In the simulations, the computational domain is set to (10D × 10D × 2D) and the particle spacing to D/42, generating 16.8 million fluid particles.

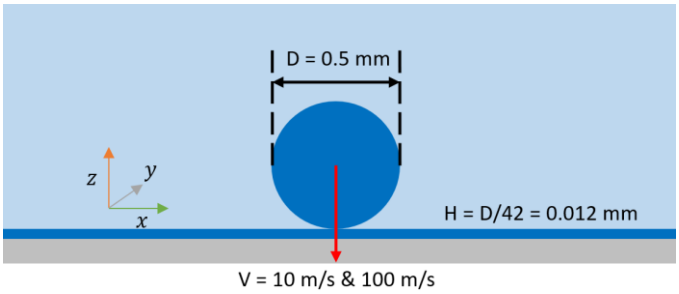

Figure 34. Sketch of droplet impingement on a thin water film at various speeds.

As presented in Figure 35, snapshots from the simulations at different time instances, t* = 0.1189, 1.189, 2.378, 3.568 and 4.758, are compared. It is found that the case of 10 m/s generates large secondary droplets due to surface tension effects and that the case of 100 m/s causes a cloud of splashing particles.

To quantitively analyze the distribution of splashing particles, the computational domain is divided into annulus zones with a width of $r_0/4$, as shown in Figure 36, where r_0 is the initial radius of the droplet, and the origin of the axes is set to the initial impacting point. N_{ri} denotes the number of particles that are above the initial water film's free surface in zone i. The number of particles and their average height at each bin are plotted in Figure 37 for both cases at t* = 1.189, 2.378, 3.568 and 4.758. It is found that the aeronautical case results more splashing particles in higher and wider spatial ranges, and these differences expand as the crown further evolves.

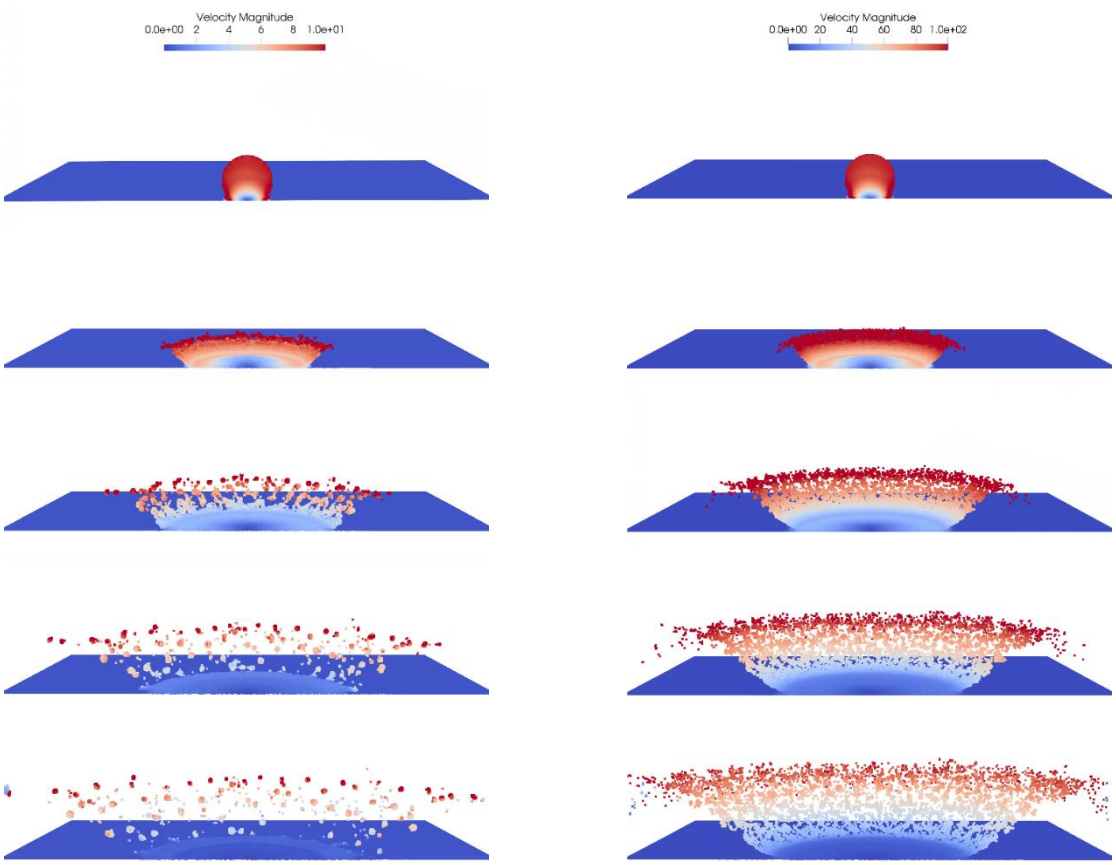

(a) 10 m/s (b) 100 m/s

Figure 35. Snapshots of a 0.5 mm droplet impacting a water film of 0.012 mm at t* = 0.1189, 1.189, 2.378, 3.568 and 4.758 (top to bottom).

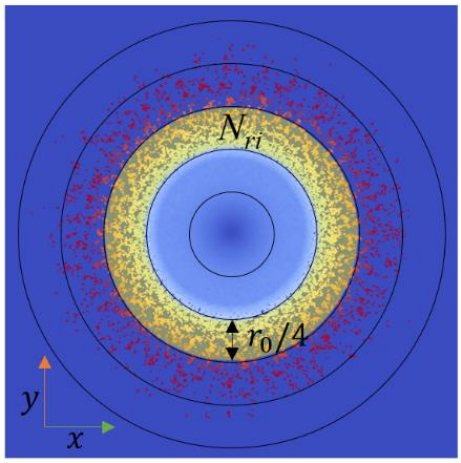

Figure 36. Radial binning method to count the number of particles in each section.

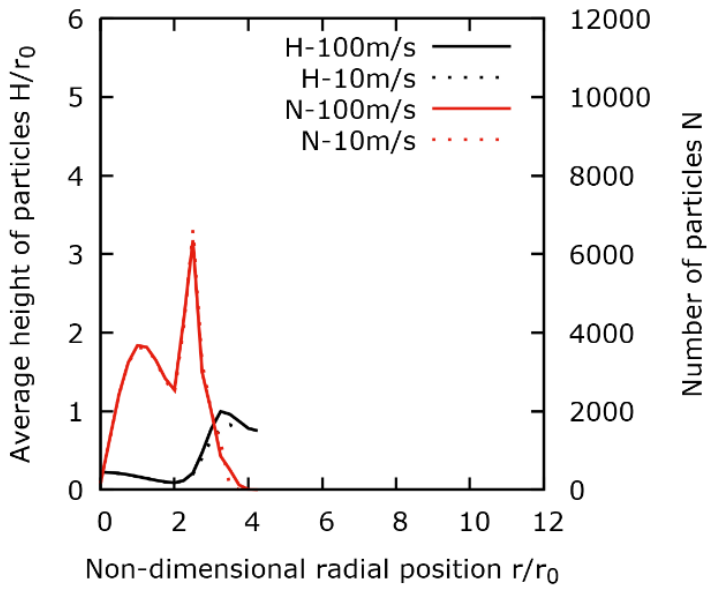

(a) t* = 1.189

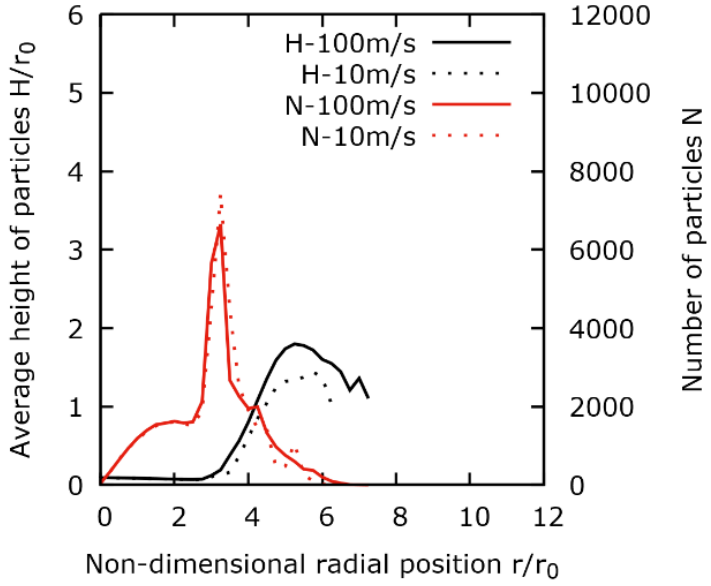

(b) t* = 2.378

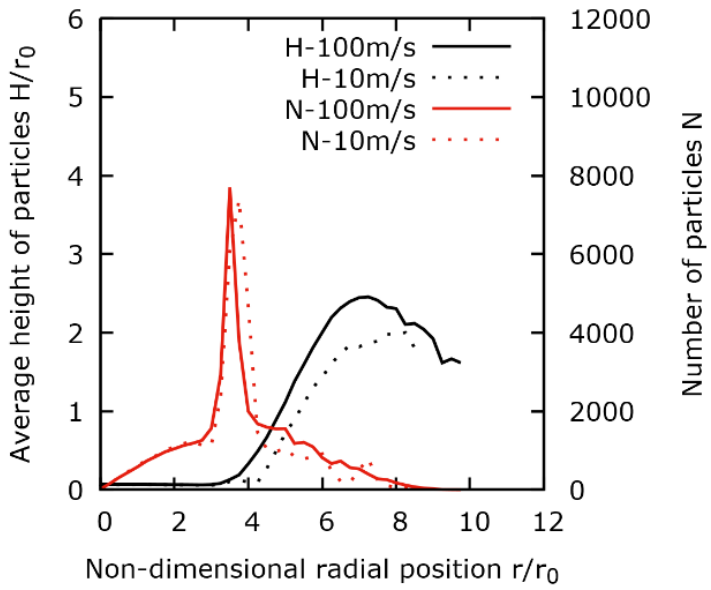

(c) t* = 3.568

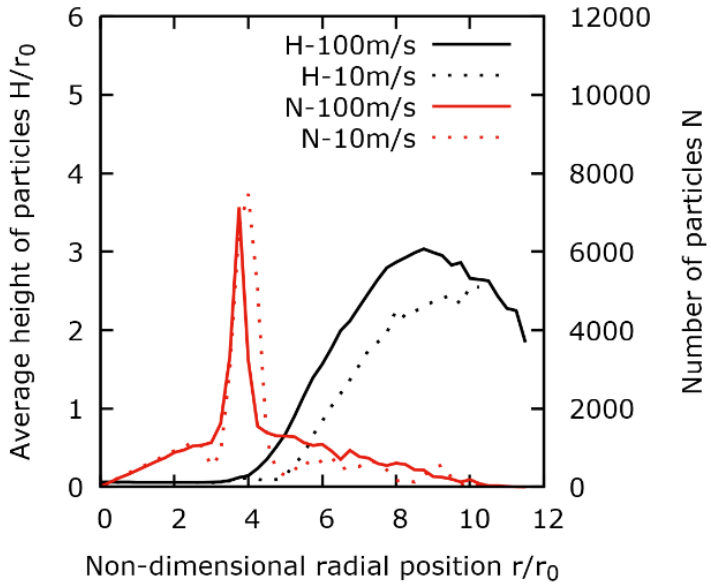

(d) t* = 4.758

Figure 37. The average height (black lines) and the number (red lines) of the splashing particles in radial sections.
D = 0.5 mm, V = 10 m/s (dotted line) & 100 m/s (solid line), H = D/42.

3.1.6 A study of the effects of droplet diameter

The effects of droplet diameter on the post-impact splashing are also studied. As shown in figure 38, the case of 100 m/s in section 3.1.5 is adapted by changing the droplet diameter to 2.5 mm and 0.025 mm.

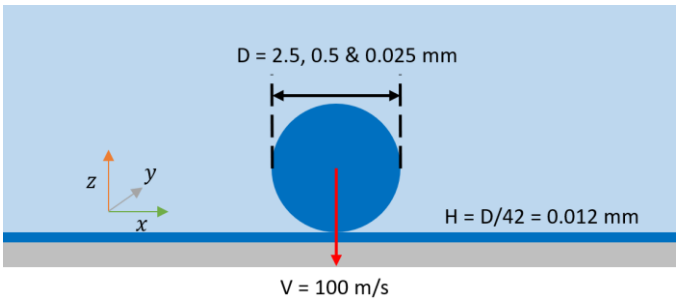

Figure 38. Sketch of droplet impingement on a thin water film with different diameters.

The distribution of particles along the radial axis and their average height at each section for D = 2.5 mm, 0.5 mm and 0.025 mm at t* = 1.189, 2.378, 3.568 and 4.758, are presented in Figure 39. Although the diameters vary 100-fold, the non-dimensional particle distribution almost overlap. It means that the splashing range is proportional to the droplet diameter and that SLD can cause much wider distributions than the normal cloud droplets at the same impact speed, due to their large size. This is a confirmation of the ice accretion beyond the protected zones under SLD conditions.

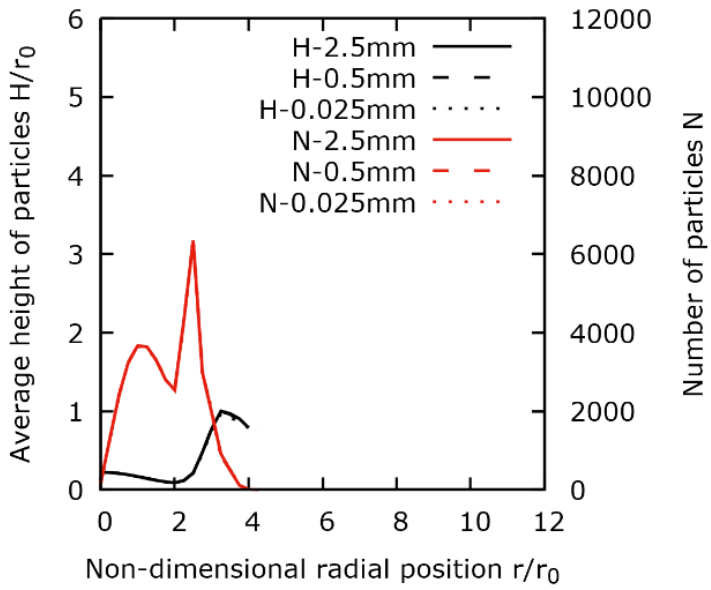

(a) t* = 1.189

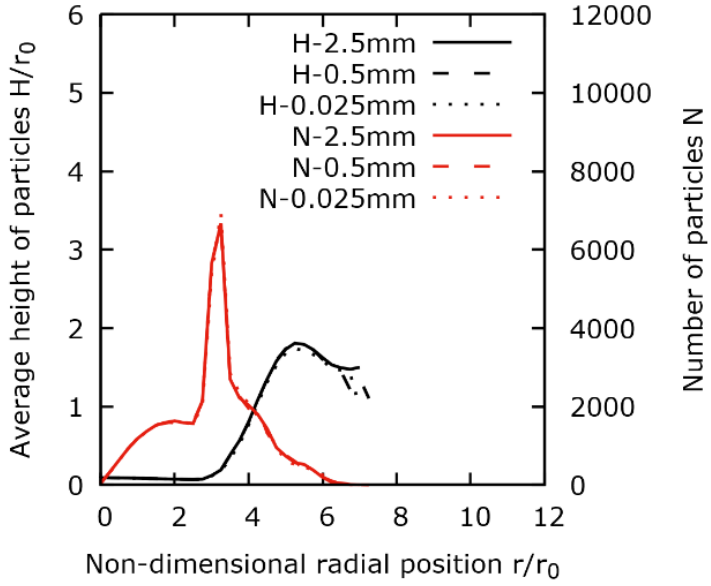

(b) t* = 2.378

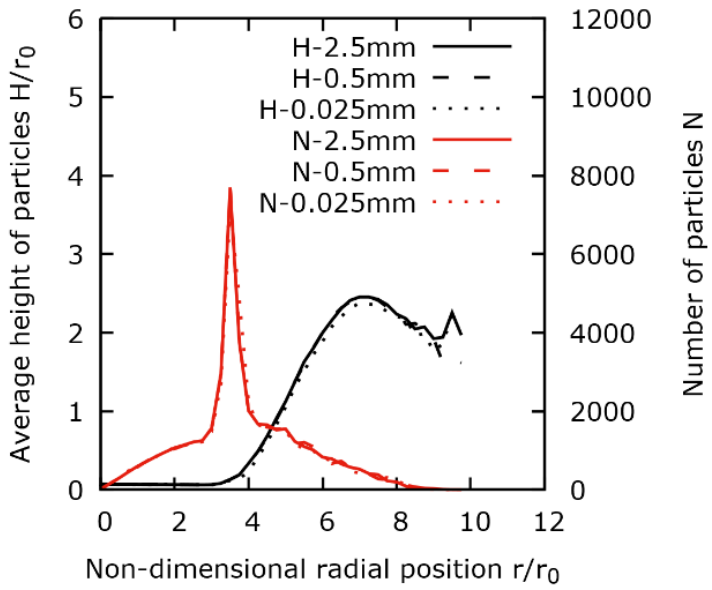

(c) t* = 3.568

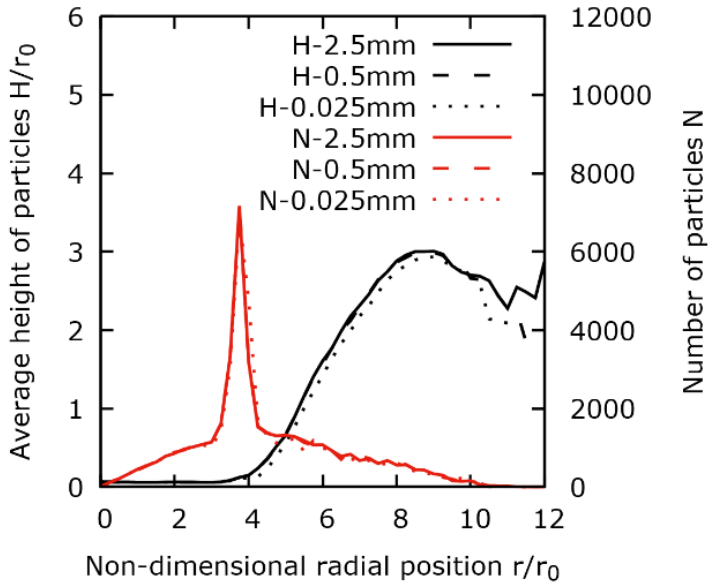

(d) t* = 4.758

Figure 39. The average height (black lines) and the number (red lines) of the splashing particles in radial sections.
V = 100 m/s, H = D/42, D = 2.5 mm (solid lines), 0.5 mm (dash lines) & 0.025 mm (dotted lines).

3.2 Droplet impingement and solidification on cold solid surfaces

In this section, the solver, incorporating a latent heat model to represent phase change, is extended to simulate droplets impinging and freezing on cold surfaces at aeronautical speeds.

3.2.1 Validation: two-phase Stefan solidification

At first, a 1D two-phase Stefan problem, in which a semi-infinite liquid domain ($x > 0$) is cooled and solidified by a wall ($x = 0$) below freezing temperature, is solved to compare against an analytical solution of ice front expressed as:

$$x_f(t) = 2\lambda\sqrt{tk/C_v}$$

where t is time, k is thermal conductivity, C_v is specific heat, and λ is a constant obtained from the transcendental equation presented in [68] and equals 0.3073 for this case.

As shown in Figure 40, the fluid domain is set to (0.1 m × 0.025 m × 0.025 m). The initial and melting temperatures of the fluid are equal to 4 °C and 0 °C, respectively, and the boundary temperature is set to −10 °C. The latent heat of fusion is taken as 80,300 J/kg. The thermal conductivity and specific heat capacity are set to 2.89 J/s/m/°C and 2590 J/kg/°C for the liquid phase, and correspondingly to 4.02 and 2050 for the solid phase. The densities for both phases are 1000 kg/m^3.

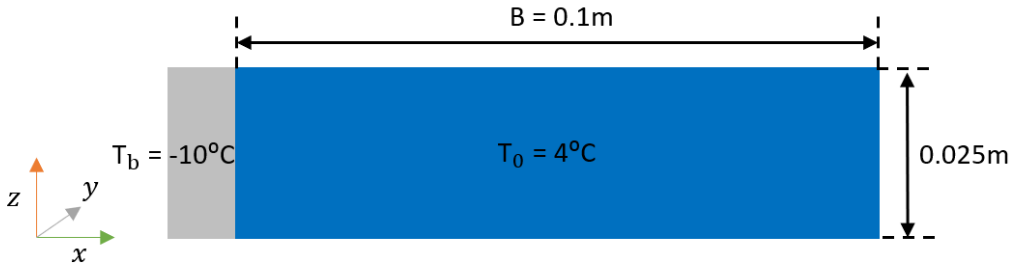

Figure 40. Sketch of the 1D two-phase Stefan problem.

Different particle spacings, Δs = B/24, B/48, B/96 and B/144, are used to generate 800, 6,000, 55,000 and 187,000 particles, respectively. The time history of the position of the ice front is plotted in Figure 41 and demonstrates that the numerical solution approaches the analytical one as the particle resolution is increased.

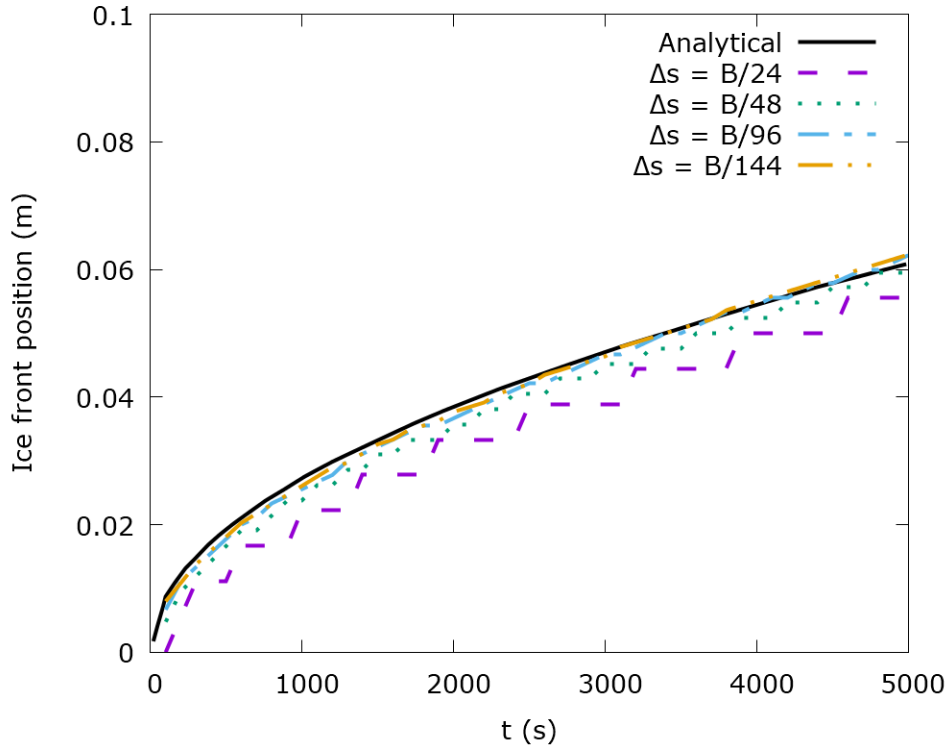

Figure 41. Time history of ice front position from analytical solution and SPH simulations of various particle spacings for the two-phase Stefan problem.

3.2.2 A stationary droplet freezing on a cold surface

A stationary droplet freezing on a cold solid surface is modeled and compared to the experimental results of [69]. Due to the different time scales of impingement and solidification, this case is split into two stages, using different time step sizes. In the first stage where inertia forces and surface tension play dominant roles, the droplet impingement on a solid surface is simulated by the full air-water-ice solver. In the second stage, the solidification of the still droplet

is modeled by a simplified air-water-ice solver accounting for heat conduction and phase change, assuming that air and water particles are at rest.

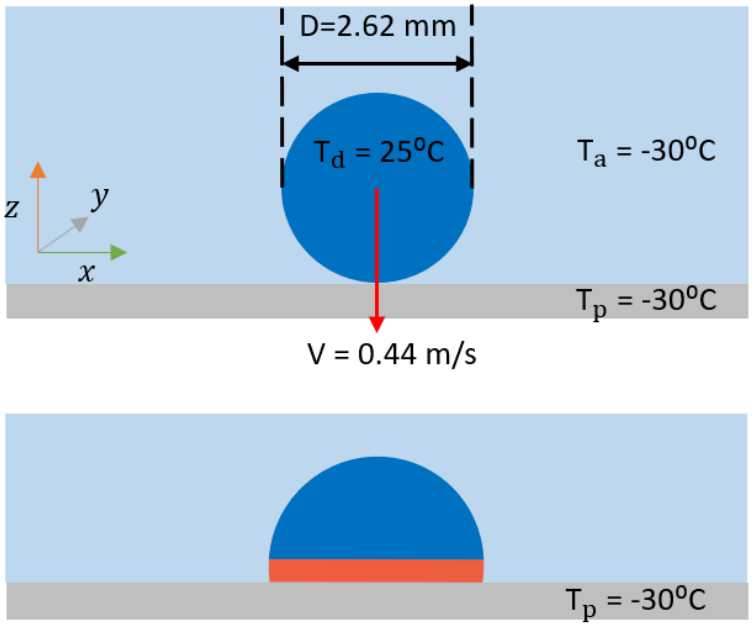

Figure 42. Sketch of the two stages of a post-impact still droplet freezing on a cold plate.

According to the experiments [69], a droplet with a diameter of 2.62 mm is launched towards a cold plate at a speed of 0.44 m/s, as shown in Figure 42. The droplet and air are initially set to 25 °C and −30 °C, respectively, and the cold plate has a constant temperature of −30 °C. The computational domain is set to (3.5D × 3.5D × 1.7D), and the particle spacing is equal to D/40. 32,000 and 1.2 million particles are used for water and air phases, respectively. For all the cases, the latent heat of fusion is taken as 333,500 J/kg. The thermal conductivity and specific heat capacity are set to 0.591 J/s/m/°C and 4190 J/kg/°C for water, and correspondingly to 2.20 and 2100 for ice, and 0.024 and 715 for air.

In Figure 43, snapshots at different time instances show the temperatures of the droplet impacting, spreading, retracting, and depositing on the solid surface. It is found that during impingement the heat transfer between cold plate and droplet is not significant and mainly happens

near the plate. After impingement, a still droplet with a base diameter of 3.56 mm and a height of 1.58 mm is obtained and used in the solidification stage.

In Figure 44, snapshots from experiments and SPH simulations at t = 1 s and t = 5 s illustrate the freezing process of the still droplet on the cold plate. In Figure 45, the time history of the central position of the ice front is compared to experimental data, showing good agreement. At the solidification stage, the SPH simulation only accounts for the thermal effects, and the deformation of the still droplet caused by ice expansion and surface tension cannot be captured. Future work can introduce the density change and surface tension effects into this stage by designing an air-water model that uses adaptive particle resolution and can tolerate large time step sizes.

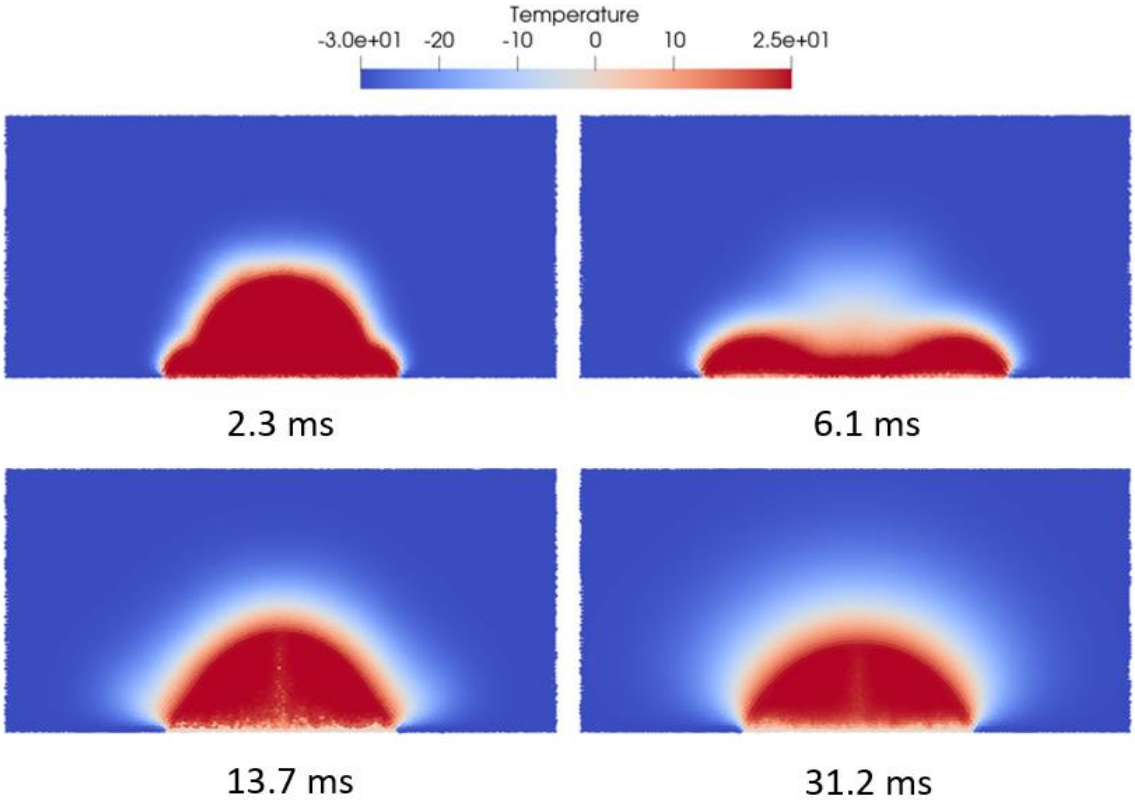

Figure 43. Snapshots of a droplet impacting a cold plate at different time instances. D = 2.62 mm, T_d = 25 °C, T_p = −30 °C and V = 0.44 m/s.

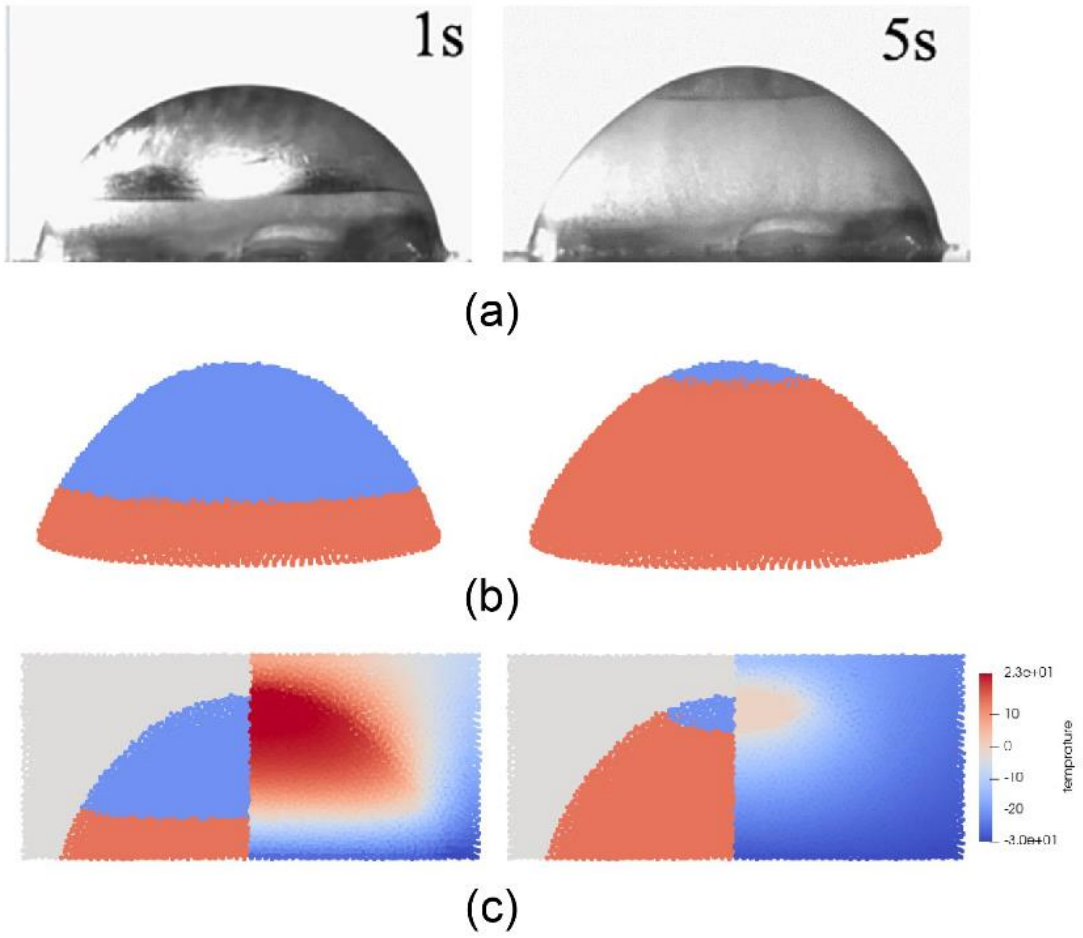

Figure 44. Snapshots of the solidification of a still droplet with a base diameter of 3.56 mm and a height of 1.58 mm on a −30 °C plate.
(a) experimental photos [69]; (b) water-ice interface (blue: water; light red: ice); (c) air-water-ice interface (left) and air-water-ice temperature (right).

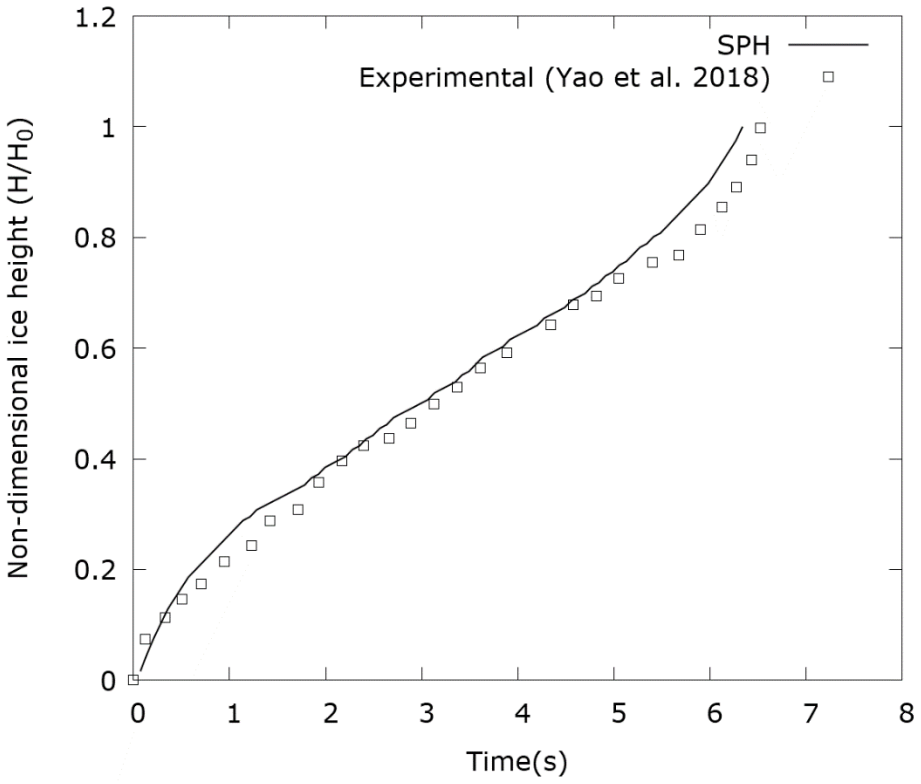

Figure 45. Time history of the position of central freezing front of a still droplet with a base diameter of 3.56 mm and a height of 1.58 mm on a −30 °C plate.

3.2.3 A droplet impinging and freezing on a cold surface

Droplet impingement and solidification on a cold solid surface at different speeds are simulated, and the effects of droplet speed on the impinging and freezing process are analyzed.

A droplet with a diameter of 0.5 mm and a temperature of 0 °C is launched towards a solid surface at −50 °C, as shown in Figure 46. The computational domain is set to (7D × 7D × 1.2D), and the particle spacing is equal to D/45, which results in using 49,000 and 4.80 million particles for water and air phases, respectively. The impact velocities are set to 5 m/s and 100 m/s.

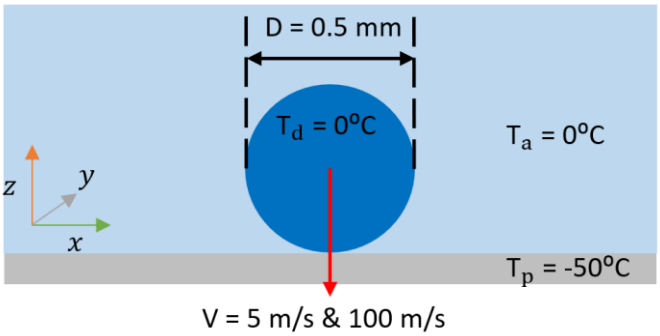

Figure 46. Sketch of the droplet normal impingement.

As shown in Figures 47-48, droplet impingement and solidification take place at different time scales, 0.640 ms and 2.890 ms for V = 5 m/s, and 0.032 ms and 2.105 ms for V = 100 m/s. This means that, for a droplet at a temperature equal or above 0 °C impacting on a cool plate, the solidification process falls behind due to the latent heat of fusion, especially at aeronautical speeds. SLD can freeze immediately upon impact or slightly thereafter [1], indicating that supercooled effects, such as nucleation and dendrites propagation, may play an important role in this process.

The case of 100 m/s generates many splashing particles as compared to 5 m/s, showing that the aeronautical impingement is characterized by a cloud of secondary droplets. Some splashing particles hit the wall boundary, as the size of the computational domain is limited by the computing cost. This can be resolved by introducing an adaptive particle resolution technique.

To draw ice particle distribution profiles, the computational domain is divided into annulus zones with a width of $r_0/10$, as shown in Figure 49, where r_0 is the radius of the droplet, and (0, 0, 0) is the initial impacting point. Denoting N_{ri} and N_o as the number of ice particles in zone i and in the entire domain, respectively, the percentage of ice particles in zone i, N_{ri}/N_o, is plotted in Figure 50. The two cases have a similar linear distribution (indicating an even ice thickness) at $r < 2.5r_0$. Beyond this point, the low-speed case presents thicker ice on the edge, while the high-speed simulation maintains a linear trend until splashing particles being at $r > 4r_0$.

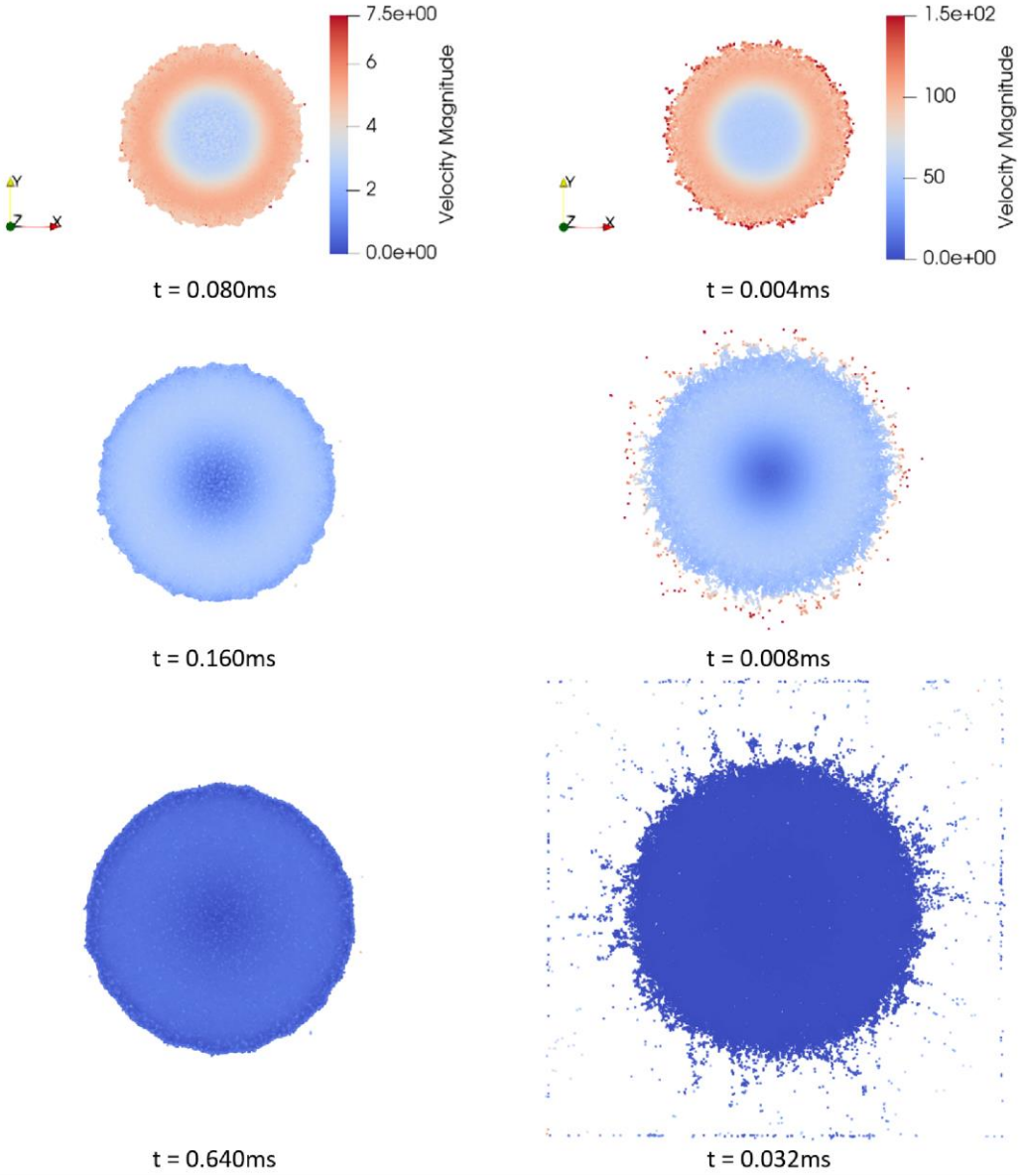

Figure 47. Snapshots of the impingement stage at different time instances. D = 0.5 mm, T_d = 0 °C, T_p = −50 °C and V = 5 m/s (left) & 100 m/s (right).

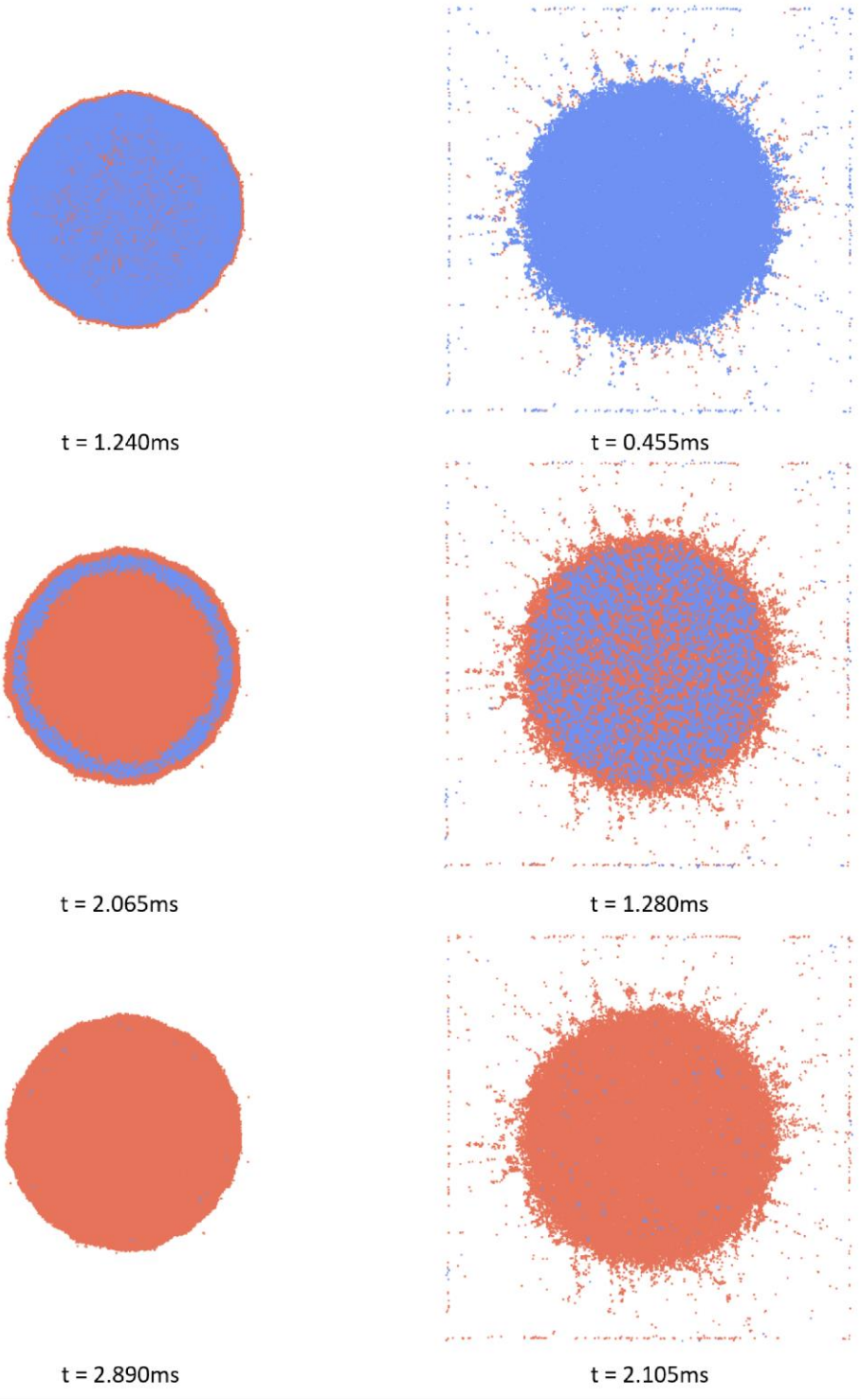

Figure 48. Snapshots of the solidification stage at different time instances.
D = 0.5 mm, T_d = 0 °C, T_p = −50 °C and V = 5 m/s (left) & 100 m/s (right) (blue: water; light red: ice).

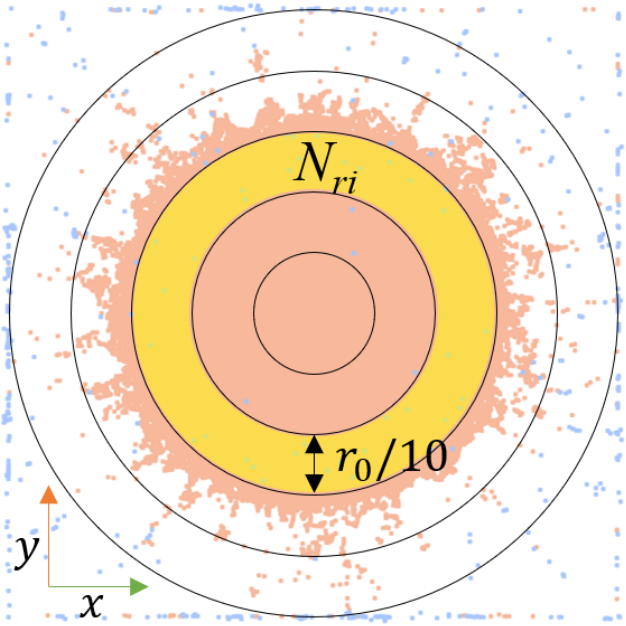

Figure 49. Sketch of the radial binning technique employed to count the number of ice particles in each concentric zone.

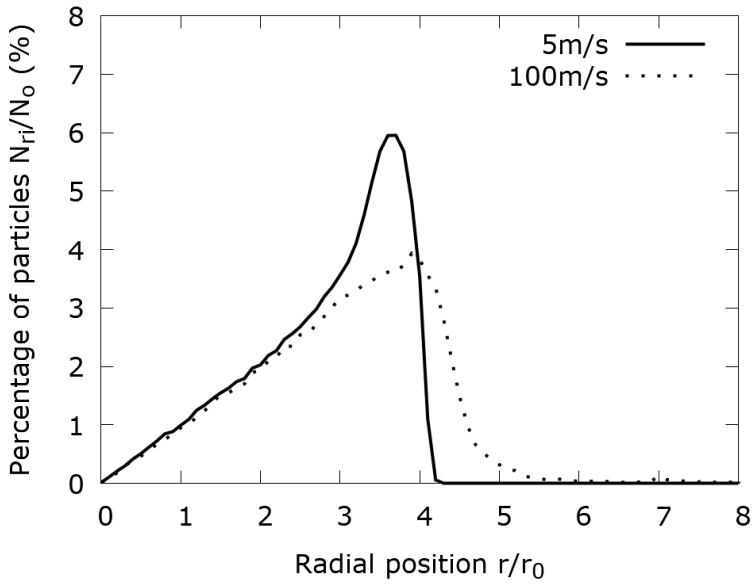

Figure 50. Post-impact ice particle distribution for the normal impingements. D = 0.5 mm, T_d = 0 °C, T_p = −50 °C and V = 5 m/s & 100 m/s.

3.2.4 A droplet obliquely impinging and freezing on a cold surface

Oblique impingements are conducted to study the effects of impact angle, which is a simplified representation of the curvature of aircraft surfaces.

In the simulations, as illustrated in Figure 51, a droplet with a diameter of 0.5 mm and an initial temperature of 0 °C is launched towards a cold plate maintained at −50 °C at 5 m/s or 100 m/s with an impact angle of 30°. The computational domain has a size of (8.4D × 6.0D × 1.2D), and the particle spacing is set to D/43. 48,000 and 4.7 million particles are used for the water and air phases, respectively.

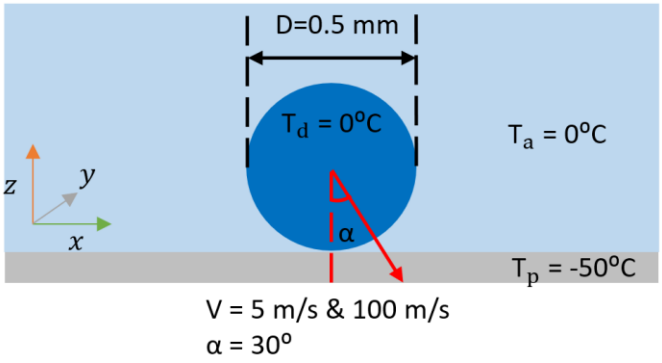

Figure 51. Sketch of the oblique droplet impingement.

The snapshots of the impingement stage are presented in Figure 52, showing that more splashing particles are generated for 100 m/s. The snapshots in the freezing stage are listed in Figure 53, showing that the case of 5 m/s uses more time to complete solidification, and that for both cases the forward front edge takes more time to freeze than for normal impingement.

As shown in Figure 54, the computational domain is divided into bands of width $r_0/10$ along the *x*-direction, and N_{xi} represents the number of particles at zone *i* in the *x*-direction. Ice particle distributions along the *x*- and *y*-directions are plotted in Figures 55 and 56, respectively, where (0, 0, 0) is the initial impacting point. It is found that the high-speed case has a wider spreading range

in all directions, and that there is more splashing in the forward (positive *x*) direction. The leading front has a thicker ice layer than tailing part for both cases.

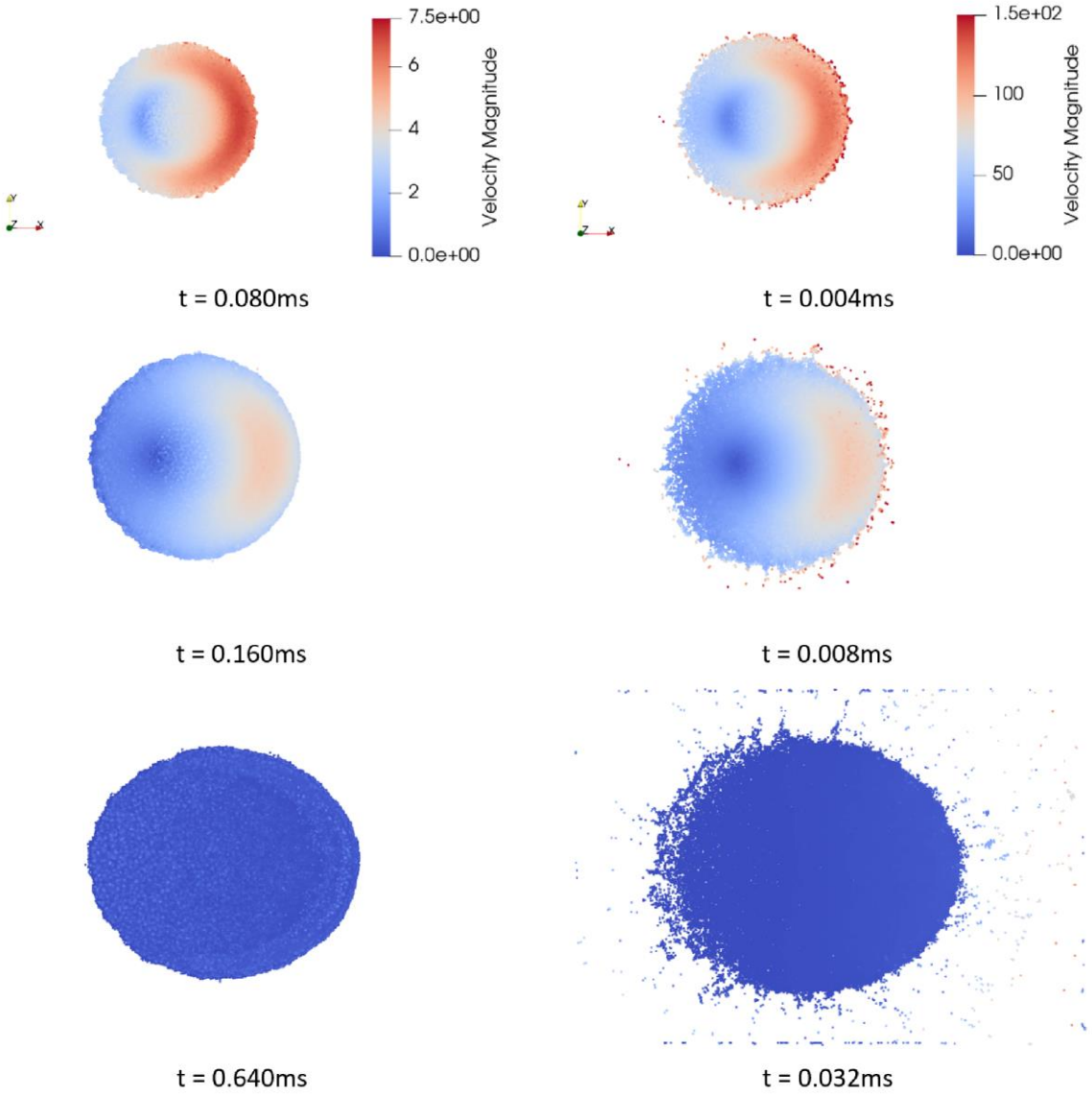

Figure 52. Snapshots of the oblique impingement stage at different time instances. D = 0.5 mm, T_d = 0 °C, T_p = −50 °C, α = 30° and V = 5 m/s (left) & 100 m/s (right).

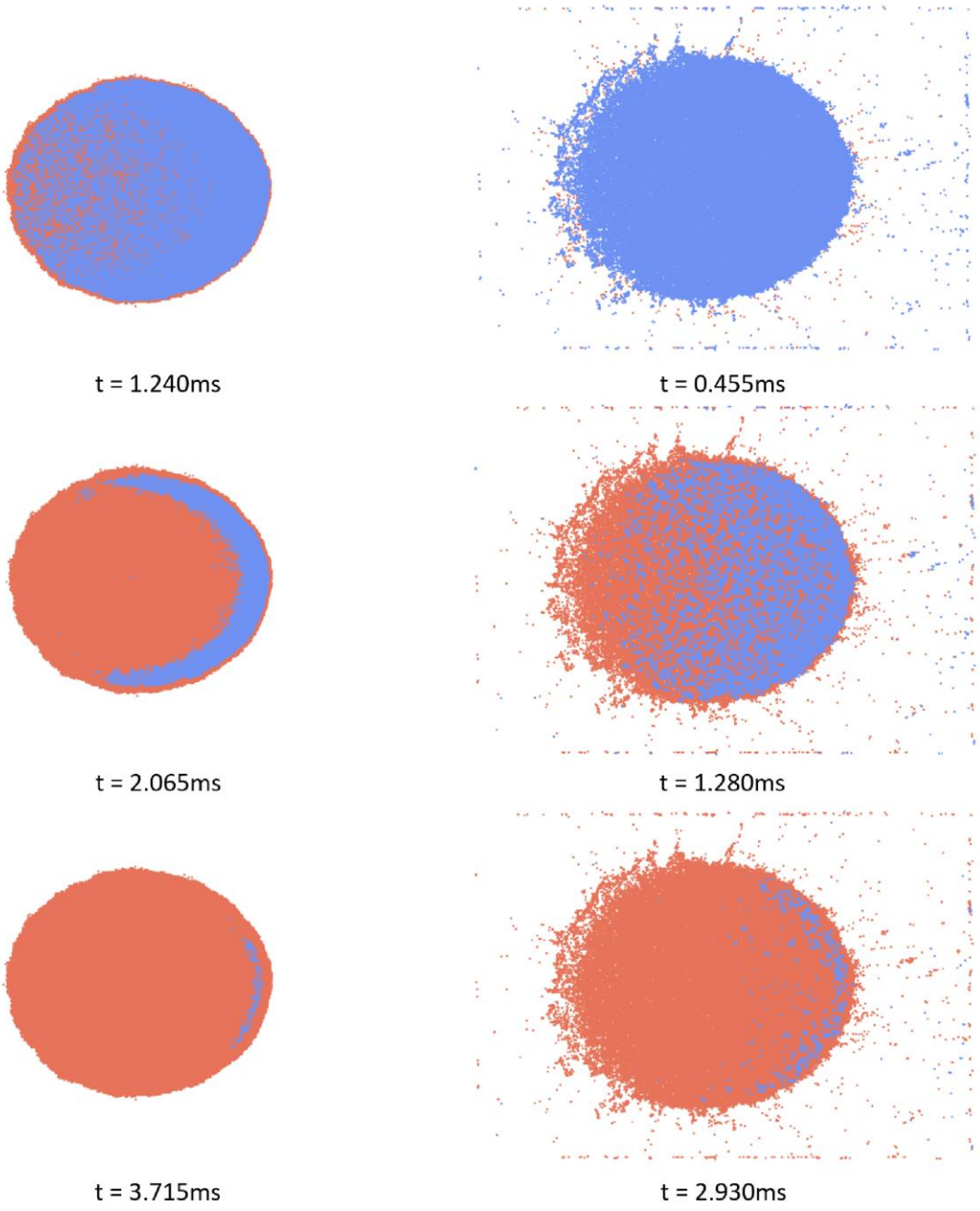

Figure 53. Snapshots of the solidification stage at different time instances. D = 0.5 mm, T_d = 0 °C, T_p = −50 °C, α = 30° and V = 5 m/s (left) & 100 m/s (right) (blue: water; light red: ice).

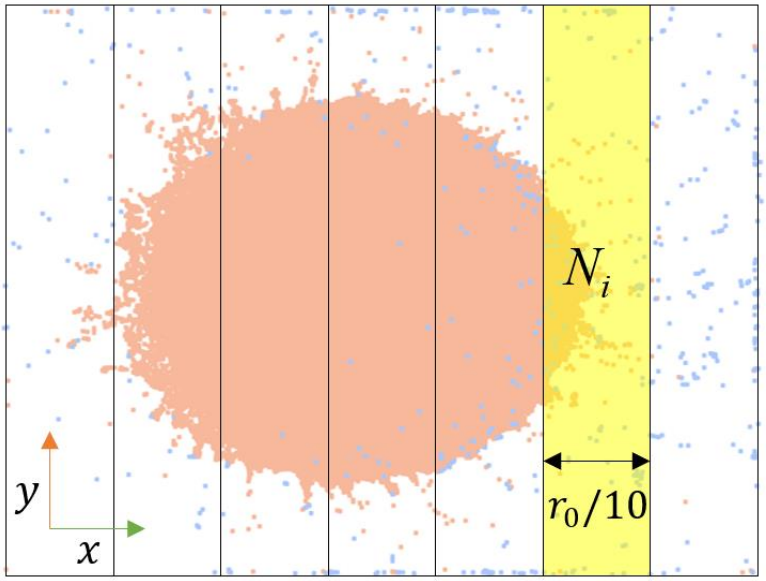

Figure 54. Sketch of the binning technique in *x*-direction employed to count the number of ice particles in each zone.

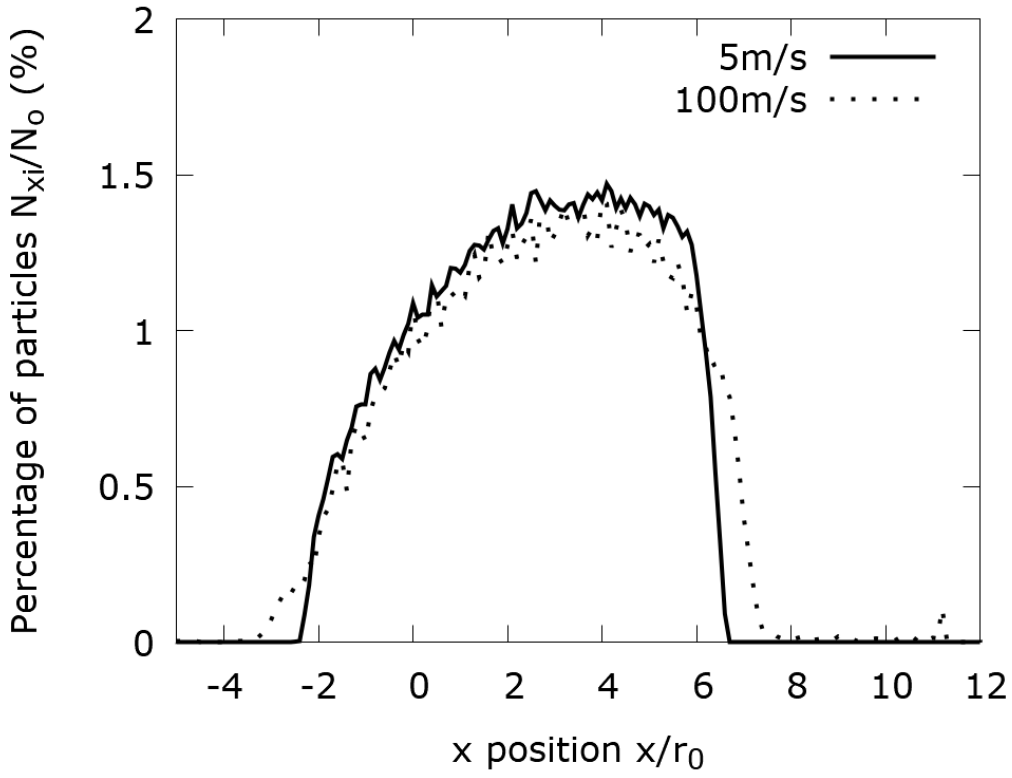

Figure 55. Post-impact ice particle distributions along the *x*-direction for the oblique impingements. D = 0.5 mm, T_d = 0 °C, T_p = −50 °C, α = 30° and V = 5 m/s & 100 m/s.

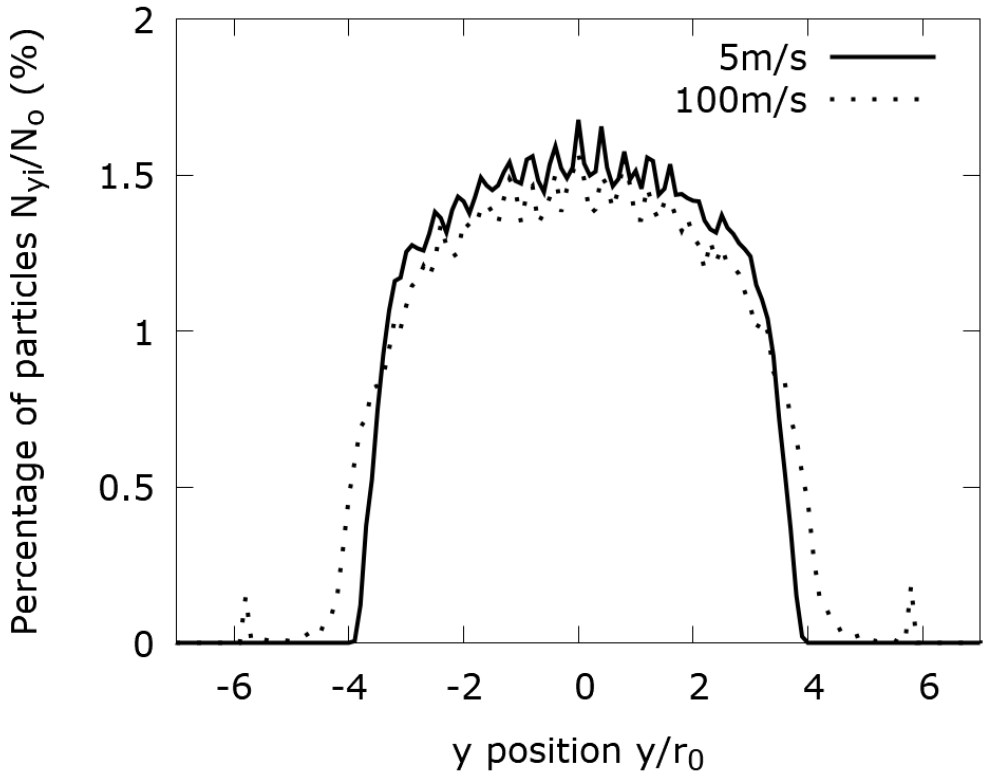

Figure 56. Post-impact ice particle distributions along the *y*-direction for the oblique impingements. D = 0.5 mm, T_d = 0 °C, T_p = −50 °C, α = 30° and V = 5 m/s & 100 m/s.

3.3 Droplet impingement and solidification on hydrophobic surfaces

In this section, the interactions between droplet and hydrophobic/superhydrophobic coatings are investigated using a contact angle model to represent non-wetting effects. Droplet evolving on solid surfaces with various contact angles is first modeled to validate the improved contact angle model. Then, droplets impacting on hydrophobic and superhydrophobic surfaces are simulated.

3.3.1 Validation: evolution of 3D droplets on solid surfaces

The contact angle model is first validated by modeling water cuboids on solid surfaces evolving into droplets at equilibrium with given contact angles, as shown in Figure 57. According to [52], when external body forces are absent, the equilibrium shape of a 3D droplet on a solid surface is a spherical cap, and its radius is a function of its volume V and the given contact angle θ as follows:

$$r = (3V/(\pi(2+\cos\theta)(1-\cos\theta)^2))^{1/3}$$

The height of the spherical cap and the diameter of the solid-fluid contact area can be calculated as:

$$H = r \times (1-\cos\theta)$$

$$D = 2r \times \sin\theta$$

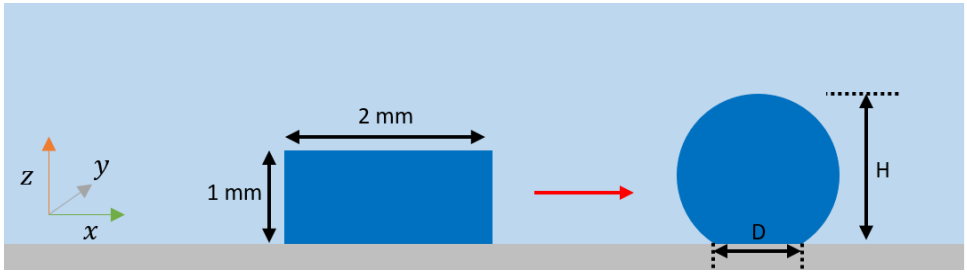

Figure 57. Evolution of 3D droplets on solid surfaces.

In the simulations, the cuboid has a size of (2 mm × 2 mm × 1 mm), and the computational domain is chosen as (6 mm × 6 mm × 4 mm). The contact angle is successively set to 45°, 60°, 75°, 90°, 105°, 120°, 135° and 150°, and the surface tension coefficient equals 0.072 N/m.

To investigate the resolution effects, different water particle numbers: 600, 2,000, 6,000 and 16,000, are used in simulations. The snapshots of droplets evolving on surfaces with contact angles of 45°, 90° and 135° are presented in Figure 58, using 16,000 water particles. When the droplets reach equilibrium shapes, their heights and diameters of the solid-liquid contact areas are measured and compared against analytical solutions in Figures 59 and 60. It is found that the numerical solutions of 6,000 and 16,000 water particles almost overlap and are close to the analytical solutions, proving the proposed contact angle model can simulate 3D equilibrium non-wetting problems.

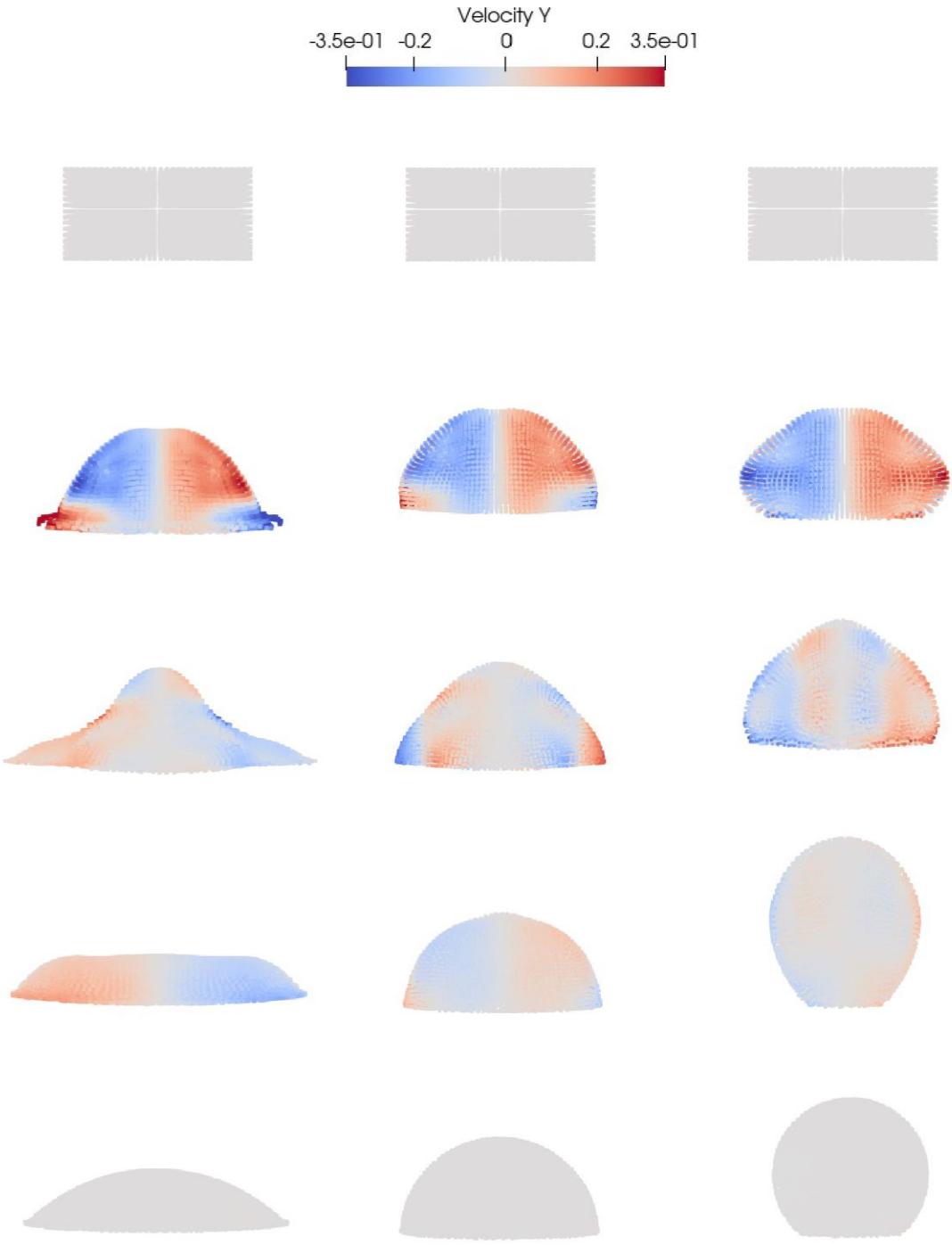

Figure 58. Snapshots of the evolution of droplets on surfaces with various contact angles: 45°(left), 90°(middle) and 135°(right).

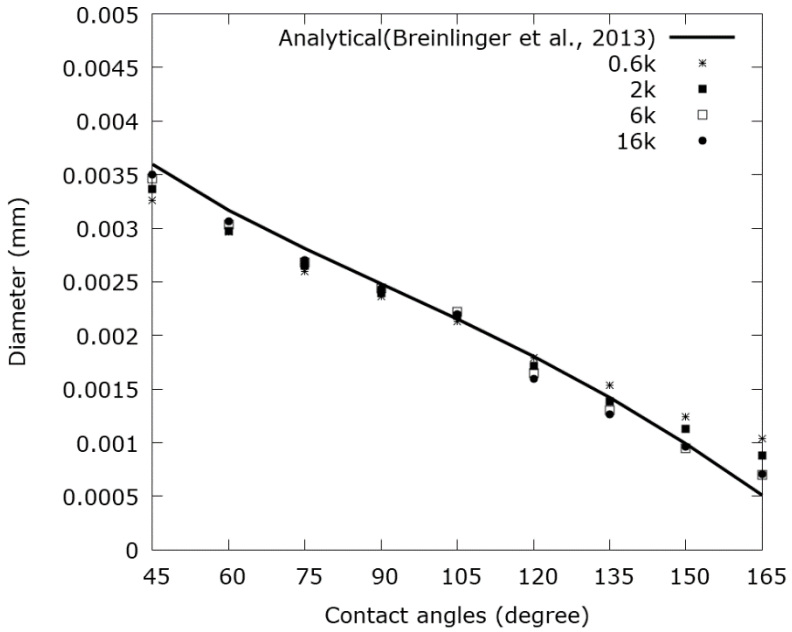

Figure 59. Diameters of the solid-liquid contact aeras of the equilibrium droplets on solid surfaces with contact angles from 45° to 165°.

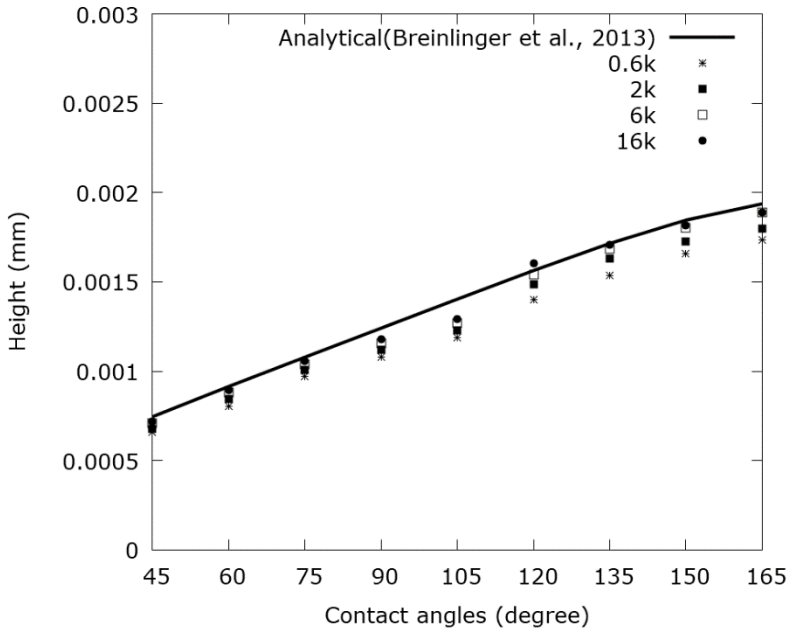

Figure 60. Heights of the equilibrium droplets on solid surfaces with contact angles from 45° to 165°.

3.3.2 A droplet impinging on a hydrophobic surface

A droplet impinging on a hydrophobic surface is simulated to test the model's capability of dynamical non-wetting problems in 3D, comparing against experiments [70] and VOF simulations [71].

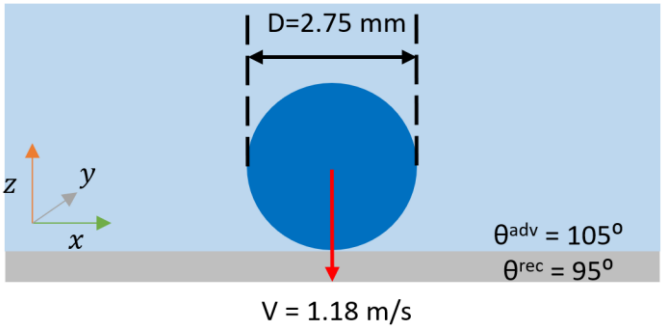

Figure 61. Sketch of a droplet impacting on a hydrophobic surface.

Following the experimental setup of [70], a droplet of diameter 2.75 mm is launched towards a solid surface at a speed of 1.18 m/s as shown in Figure 61. The advancing and receding contact angles are measured from the experiments and set to 105° and 95°, respectively. In the simulation, the computational domain is chosen as (2.85D × 2.85D × 2.85D). To investigate the effects of the number of particles, four particle spacings (D/25, D/36, D/47, D/53) are used, generating 8k, 25k, 56k and 79k water particles with 0.27m 0.75m, 2.4m and 3.4m air particles, respectively.

Figure 62 presents the snapshots of SPH simulations at different time instances, highlighting droplet impact, spread and retraction on a hydrophobic surface, and corresponding experimental photos has been presented in [70]. In Figure 63, the time history of the non-dimensional droplet spreading diameters, D/D_0, shows good agreement with experiments and VOF. By increasing the number of particles, the maximum spreading diameter increases with the 56k and 79k cases almost overlapping.

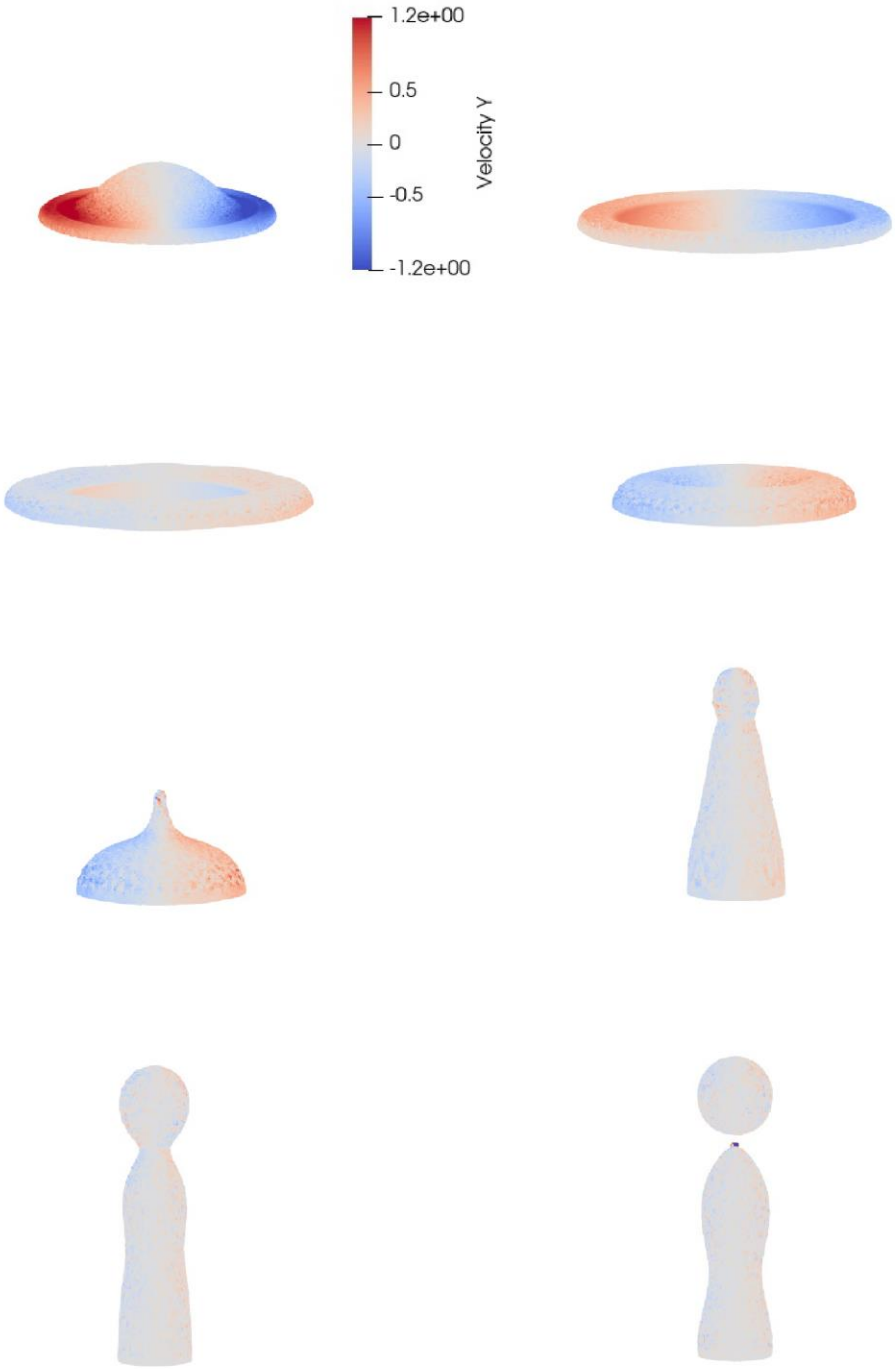

Figure 62. Snapshots of a 2.75 mm droplet impacting-spreading-retracting on a hydrophobic surface at t = 1.31, 3.14, 6.02, 8.21, 10.26, 14.02, 20.54 and 24.12 ms (left to right; top to bottom).

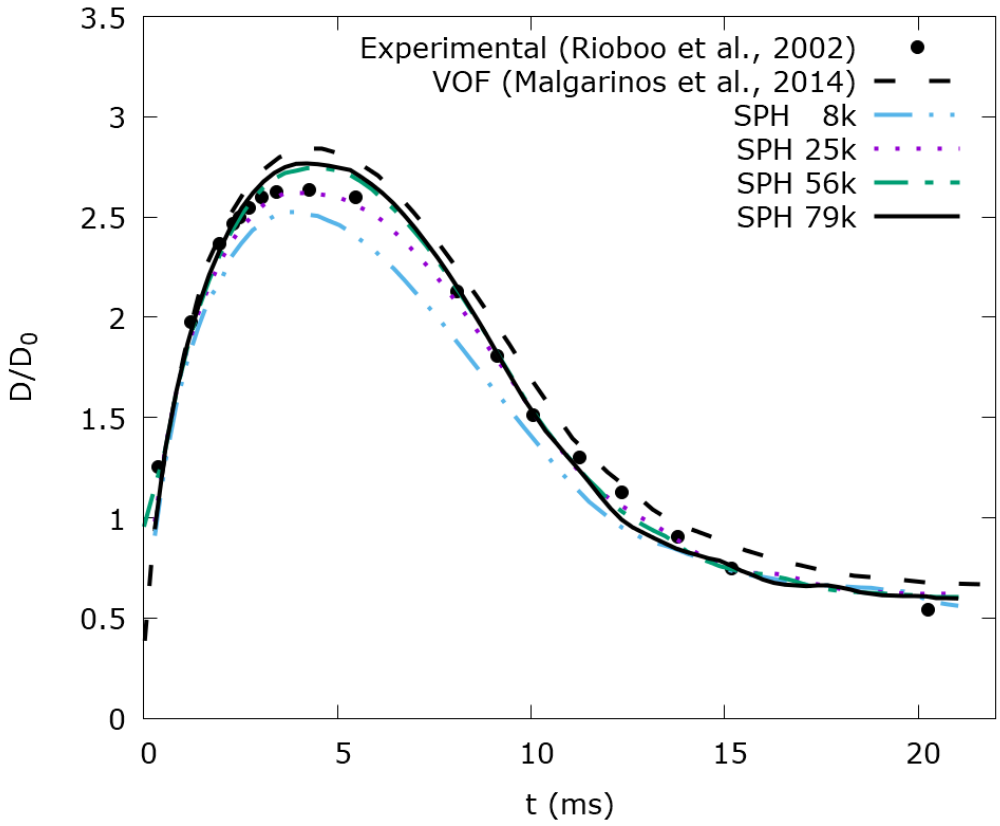

Figure 63. Time history of the non-dimensional spreading diameters of a 2.75 mm water droplet impacting a hydrophobic surface at 1.18 m/s.

3.3.3 A droplet impinging on a cold superhydrophobic surface

The solver is further applied to a 3D droplet impinging on a cold superhydrophobic surface in order to validate the modeling of the dynamical non-wetting phenomena with heat transfer and phase change.

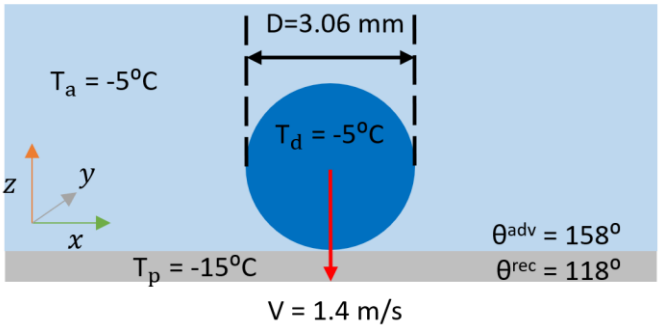

Figure 64. Sketch of a droplet impacting on a cold superhydrophobic surface.

According to the experimental setup of [21], a 3.06 mm droplet at −5 °C is launched at a velocity of 1.4 m/s towards a cold superhydrophobic surface of −15 °C, as shown in Figure 64. The advancing and receding contact angles are measured from the experiments and set to 158° and 118°, respectively.

In the simulation, the computational domain is set to (3D × 3D × 3.77D), where D is the initial droplet diameter. Four particle spacings (D/33, D/42, D/51, D/57) are used to investigate the effects of total number of particles, generating 18k, 38k, 67k and 95k water particles with 0.85m 1.6m, 3.1m and 4.3m air particles, respectively.

In this case, the supercooling degree of the droplet (−5 °C) is slight, and the nucleation and the following dendrites growth are not significant. To simplify the SPH simulations, the initial supercooling degree of the droplet is represented by the initial ice fraction of the particles, $f_{ice0} = C_v(T_f - T_d)/L$, where T_f and T_d are the freezing and initial droplet temperature. At the same time, the initial temperature of the droplet is changed to the freezing temperature. Although the

supercooled effects are not included in this case, they can play an important role in SLD impingement and solidification when droplet temperatures are below −7 °C [19]. The interactions between fluid flows and the fast solidification caused by supercooled effects are investigated in the next section.

In Figures 65, the snapshots of the central section of the SPH simulation at different time instances are presented, with the contours of *z*-axis velocity on the left and the ice fraction on the right. It is found that the freezing process is slower than the impacting, spreading and bouncing phenomena and that the freezing particles mainly appear at the bottom of the bouncing droplet. In Figure 66, the time history of the ratio of droplet contact area and the maximum spreading area, A/A_{max}, is compared against experimental data [21] and a VOF simulation [72], with good agreement being observed. As the total number of particles increases, the time history of A/A_{max} shows that the droplet retracts faster until the cases of 67k and 95k almost overlap. The snapshot of a droplet entirely rebounding from superhydrophobic surface by SPH simulation is presented in Figure 67, and the corresponding experimental photo has been published in [21].

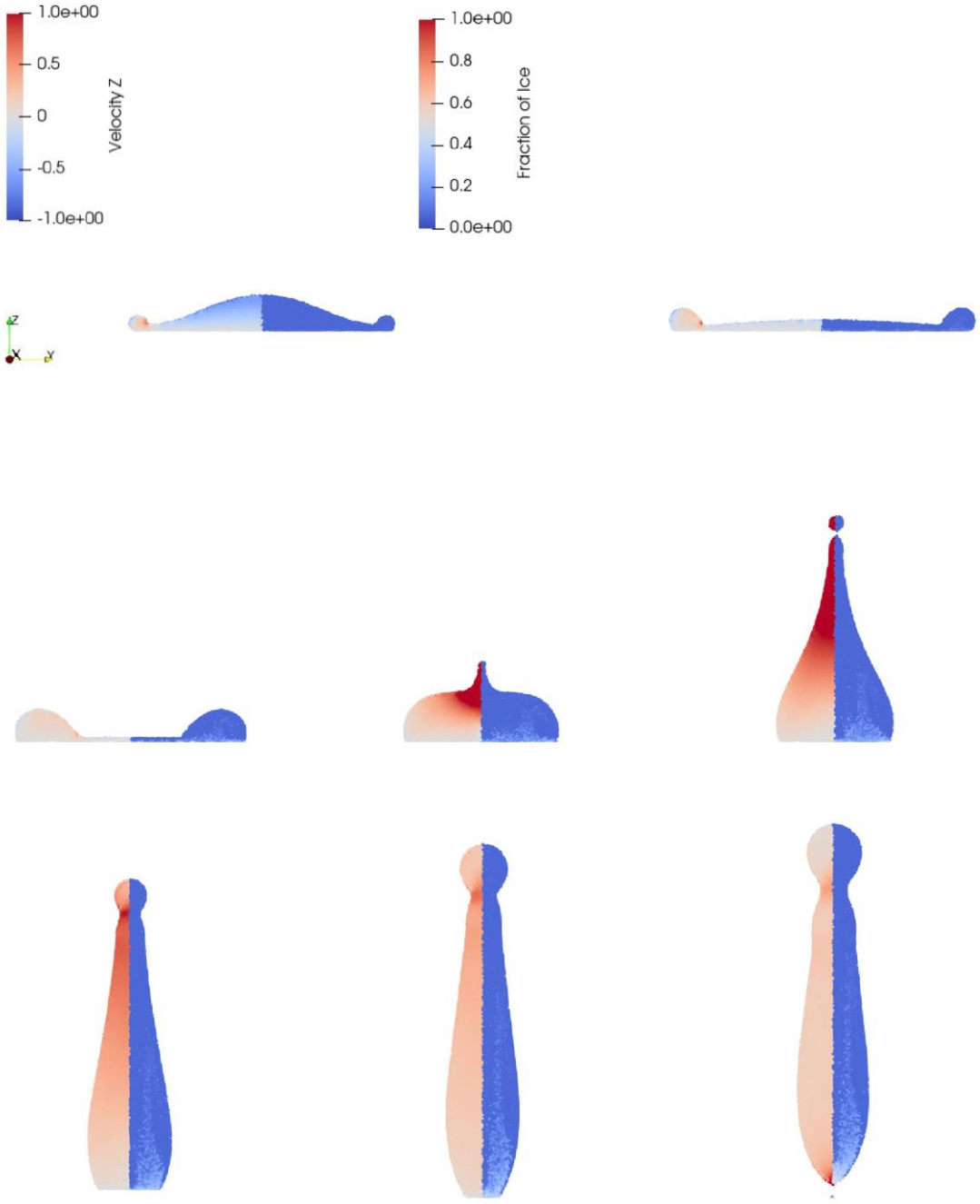

Figure 65. Snapshots of the central section of the SPH simulation of a 3.06 mm droplet impacting a −15 °C superhydrophobic surface at 1.4 m/s at t = 1.885, 3.771, 7.542, 9.428, 11.314, 15.085, 18.856 and 22.628 ms with the contours of *z*-axis velocity (left) and the ice fraction(right).

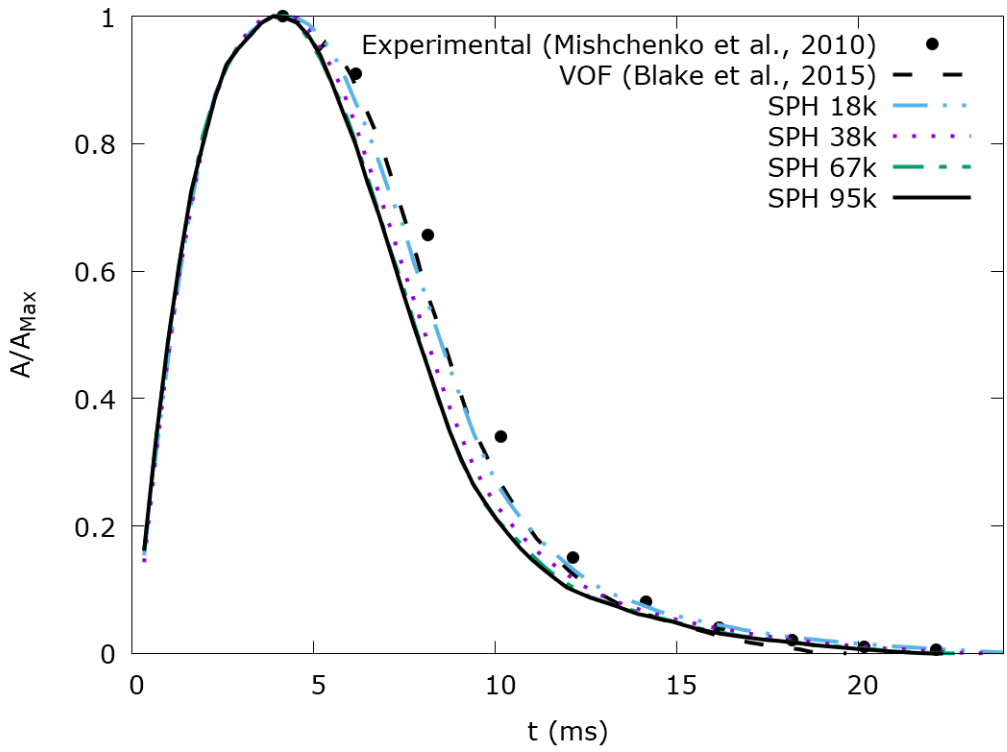

Figure 66. Time history of the contact area ratio, A/A_{max}, of a 3.06 mm droplet impacting a −15 °C superhydrophobic surface at 1.4 m/s.

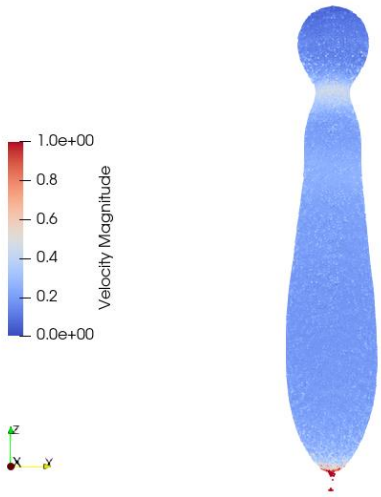

Figure 67. A supercooled water droplet entirely bouncing from a superhydrophobic surface by SPH simulations.

3.4 SLD impingement on iced surfaces with supercooled effects

In this section, the solver incorporating a supercooled solidification model is applied to SLD impingements on iced surfaces, accounting for dendritic freezing and its interactions with fluid flow.

3.4.1 Validation: SLD impinging on an ice target

A test case is first conducted to validate the supercooled solidification model. According to the experiments in [19], a −16 °C droplet with a diameter of 3.4 mm is launched towards an ice target of −11 °C at a speed of 2.2 m/s, as shown in Figure 68. In the simulation, the computational domain is set to (5D × 5D × 2.5D), and the ice target is a cylinder with a height of 0.6D and a diameter of 1.2D. The ice target is represented by fixed ghost particles, and its temperature remains constant during the simulation. At the initial time instance, the air particles are at rest and the droplet is just above the ice surface.

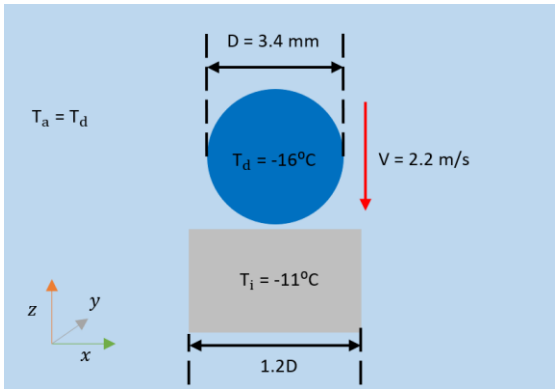

Figure 68. Sketch of a −16 °C SLD impinging on an ice target.

In order to investigate the effects of particle resolution, different particle spacings, D/19, D/29, D/38 and D/48, are used to generate 0.3, 1.2, 3.0 and 6.0 million particles for the simulations, respectively. The time history of the heights of lamella and the final thicknesses of the residual ice are compared to the experimental results in Figure 69. As the particle resolution is increased, the

thickness of the final residual ice increases and approaches the experimental results, and the two cases of D/48 and D/38 are almost overlapping.

A top view of the simulation of D/48 million particles at t = 3.86 ms is shown in Figure 70, and cross-section snapshots at t = 1.26, 2.56, 3.86, 5.16 and 7.66 ms are presented in Figure 71, to illustrate the process of the SLD impinging and freezing on the ice target. It shows that the residual ice layer actually is a mixture of ice and water particles.

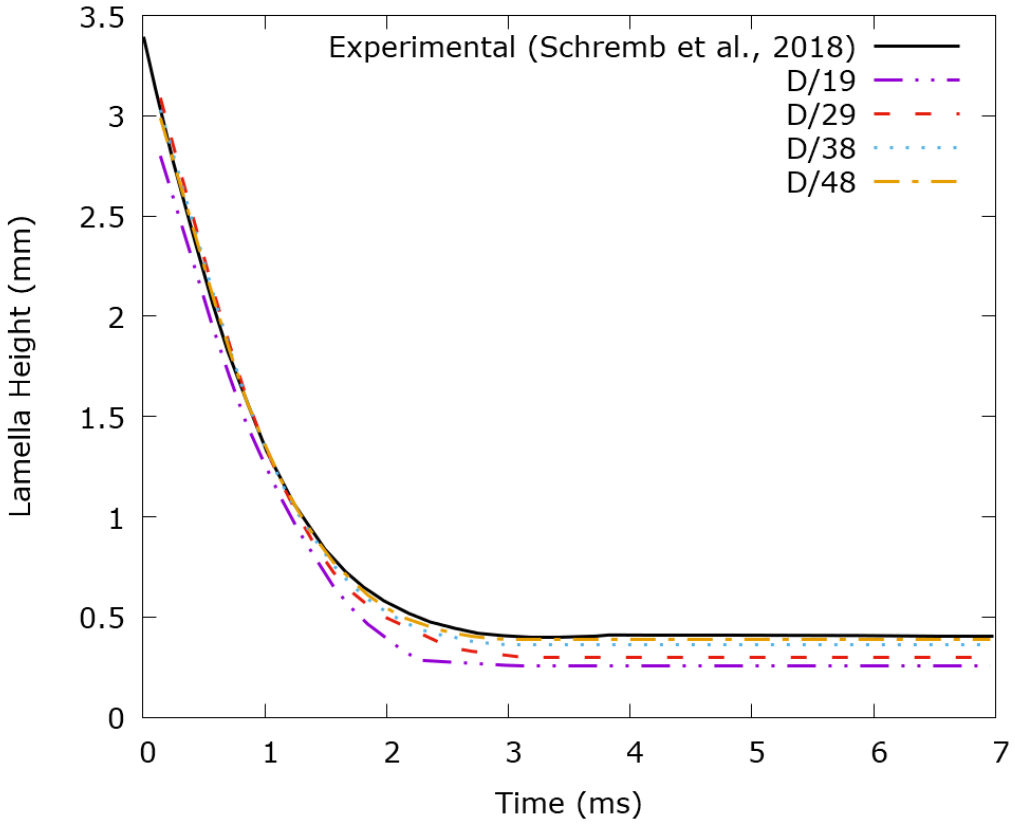

Figure 69. Time history of the lamella heights in different particle resolutions.

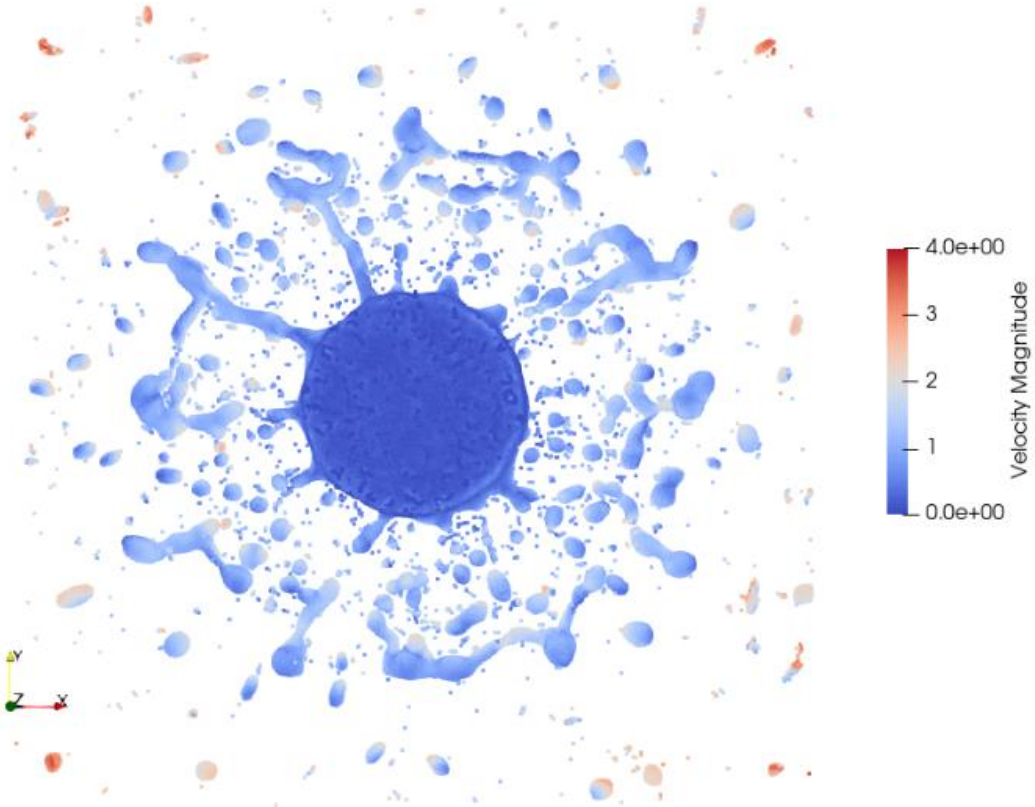

Figure 70. Top view of the SLD impinging on an ice target at t = 3.86 ms.

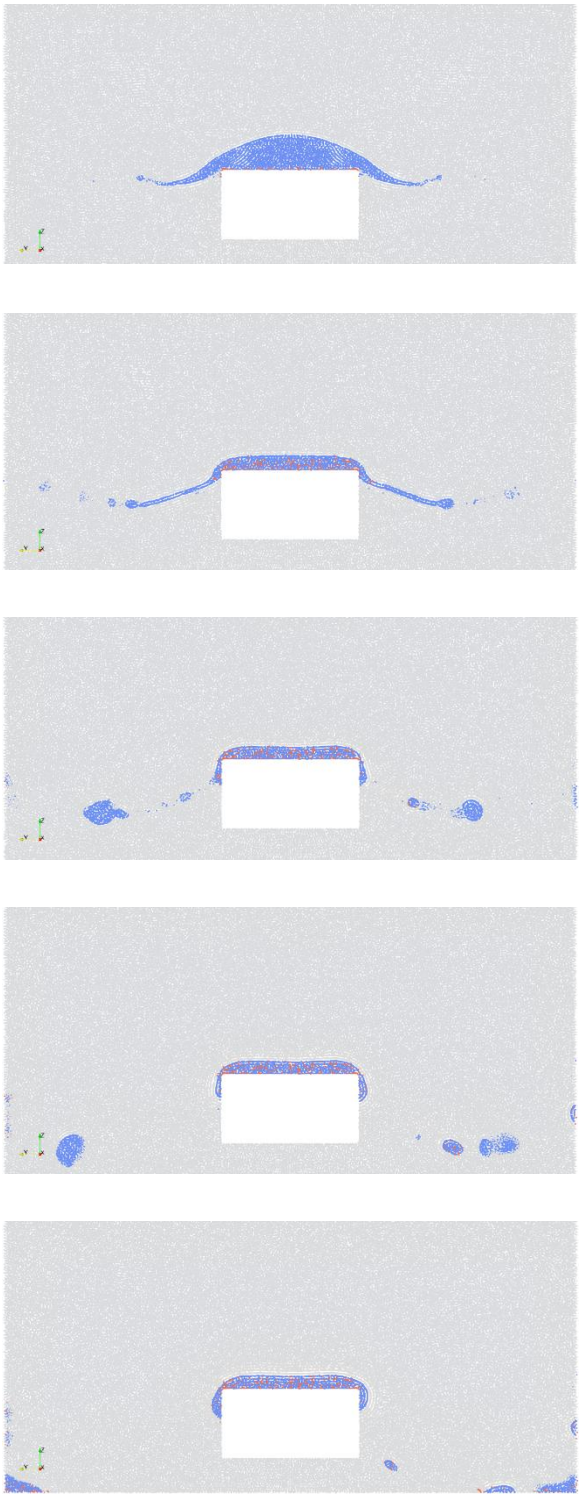

Figure 71. Snapshots of SLD impinging and freezing on an ice target at t = 1.26, 2.56, 3.86, 5.16 & 7.66 ms (blue: water; light red: ice; grey: air).
D = 3.4 mm, T_d = −16 °C, T_i = −11 °C, V = 2.2 m/s.

3.4.2 A study of the effects of droplet supercooling degree

In order to investigate the effects of supercooling degrees on SLD impingement and solidification, droplets of different temperatures, −11 °C, −16 °C and −21 °C, are launched towards an ice target, and the numerical results are compared to the experimental results [19].

As shown in Figure 72, the droplet has a diameter of 3.4 mm, and the impact speed is 2.2 m/s. The ice target is a cylinder with a height of 0.6D and a diameter of 1.2D, and it has a temperature of −11 °C. The particle spacing is equal to D/38, and the computational domain is set to (5D × 5D × 2.5D) with 3.0 million particles.

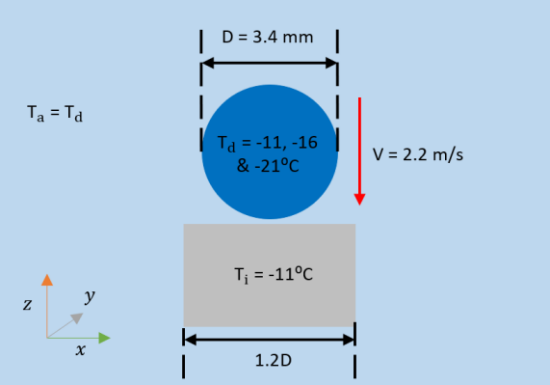

Figure 72. Sketch of SLD impinging on an ice target with different supercooling degrees.

A time series of the droplet lamella height is compared to the available experimental data of the cases of −11 °C and −16 °C in Figure 73. In general, the thicknesses of residual ice agree well with the experimental data. At the early impingement stage (t < 1 ms), the lamella heights of different supercooling degrees overlap until dendritic freezing impedes the fluid flow and causes different thicknesses of residual ice. The snapshots of the simulations at different time instances are presented in Figure 74, showing that the thickness of the residual ice increases as the droplet temperature is reduced. For the case of −11 °C, surface tension effects play a more significant role that causes the residual ice layer to retract and form a concave ice cap.

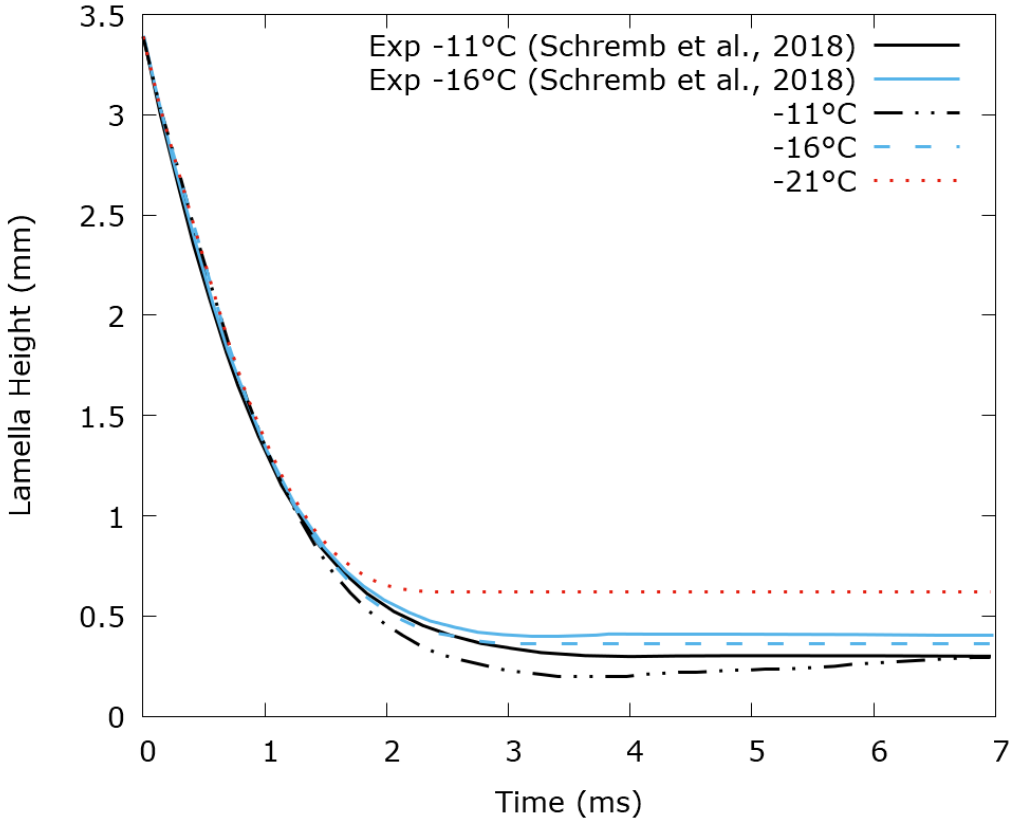

Figure 73. Time history of the lamella heights for different droplet temperatures. D = 3.4 mm, V = 2.2 m/s, T_i = −11 °C, T_d = −11, −16 & −21 °C.

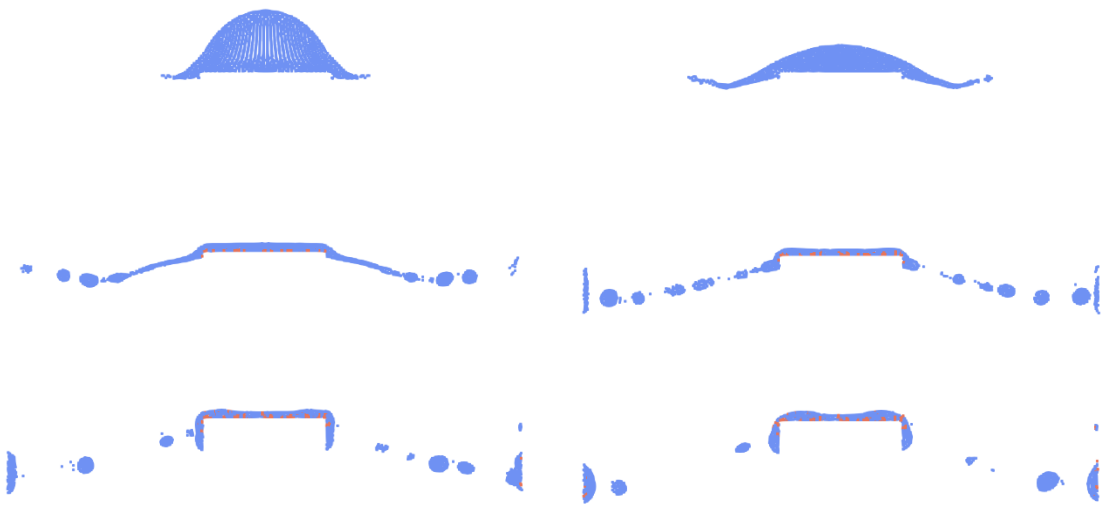

(a) −11 °C

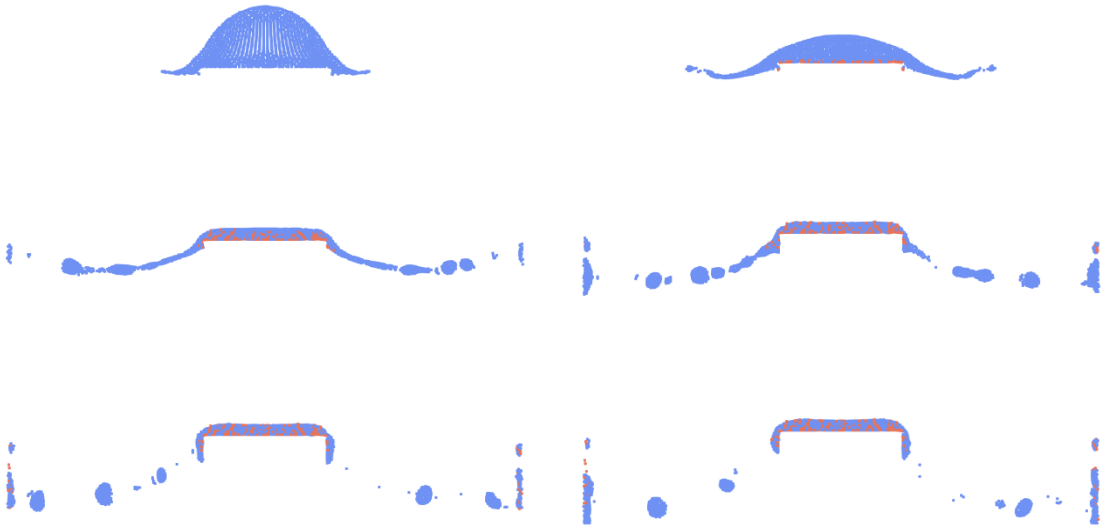

(b) −16 °C

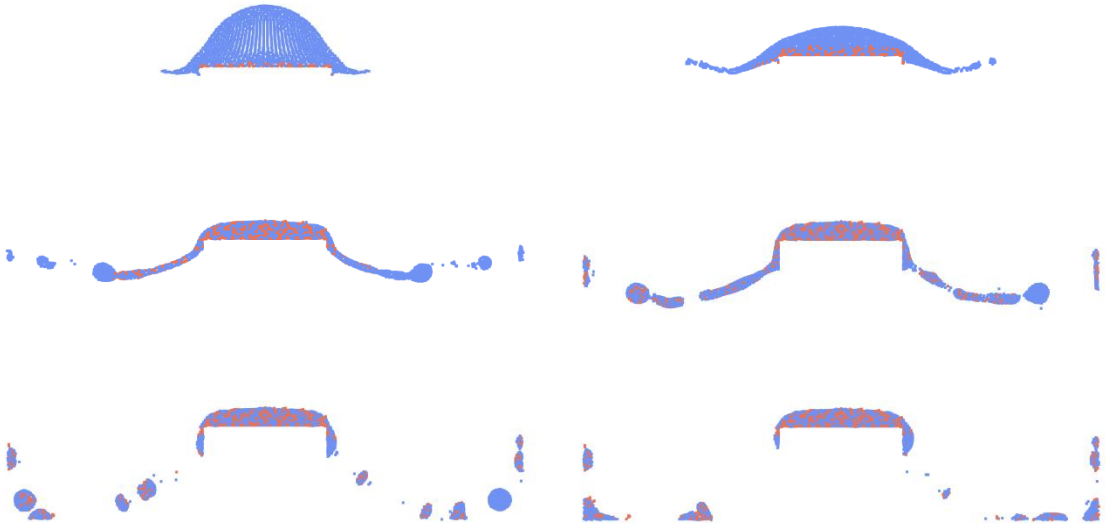

(c) −21 °C

Figure 74. Snapshots of SLD impinging and freezing on an ice target with different droplet temperatures.
D = 3.4 mm, V = 2.2 m/s, T_i = −11 °C, T_d = −11, −16 & −21 °C.

3.4.3 A study of the effects of droplet speed

Test cases are conducted with various droplet speeds to explore their effects on residual ice. As shown in Figure 75, the droplet diameter is set to 0.5 mm, typical of SLDs. The impingement speeds are chosen as 5 m/s, 10 m/s, 20 m/s and 50 m/s. The droplet and ice surface temperatures are set to −21 °C and −11 °C, respectively. In the simulation, the particle spacing is equal to D/38, the computational domain has a size of (5D × 5D × 2.5D), and 3.0 million fluid particles are used.

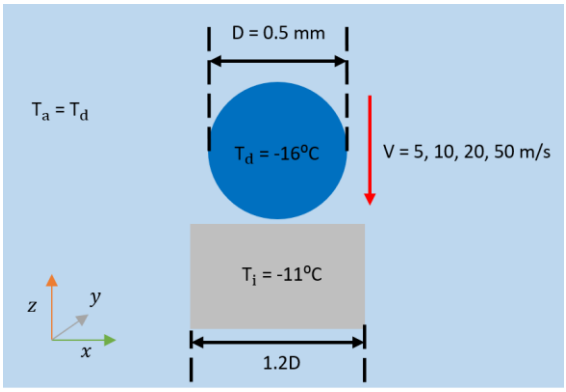

Figure 75. Sketch of SLD impinging on an ice target at various speeds.

The snapshots of the simulations for different droplet speeds at the various time instances are compared in Figure 76, and the time series of the droplet lamella height are presented in Figure 77. It is found that higher impact speeds lead to thinner residual ice layers. When the impact speed increases to 50 m/s, there is no ice particles appearing on the ice target, which means that SLD can hardly freeze on the impact point at in-flight icing conditions. As the dendritic freezing speed only depends on the degree of supercooling in the simulations, dendrites do not have enough time to grow during impingement at 50 m/s.

In the current simulations, the presence of ice is the only way to initiate supercooled solidification. For aeronautical-speed impingements, sharp changes of pressure or density might also trigger nucleation, which requires further detailed fundamental research. When new

nucleation mechanisms are identified, they can be imbedded into the present numerical framework for more accurate simulations of high-speed SLD impingements.

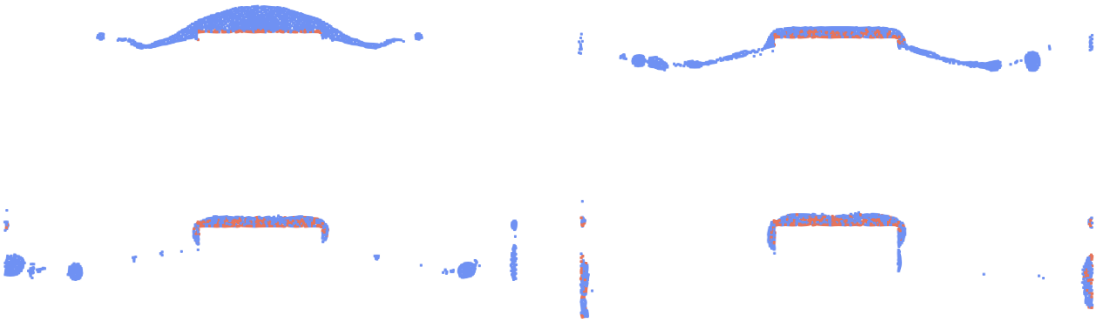

(a) 5 m/s

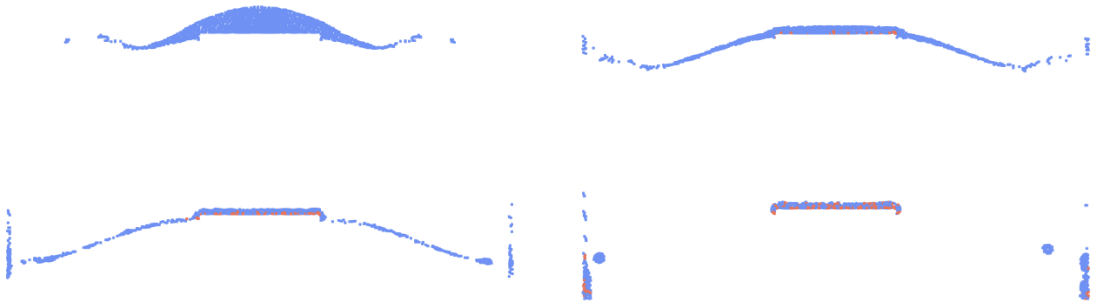

(b) 10 m/s

(c) 20 m/s

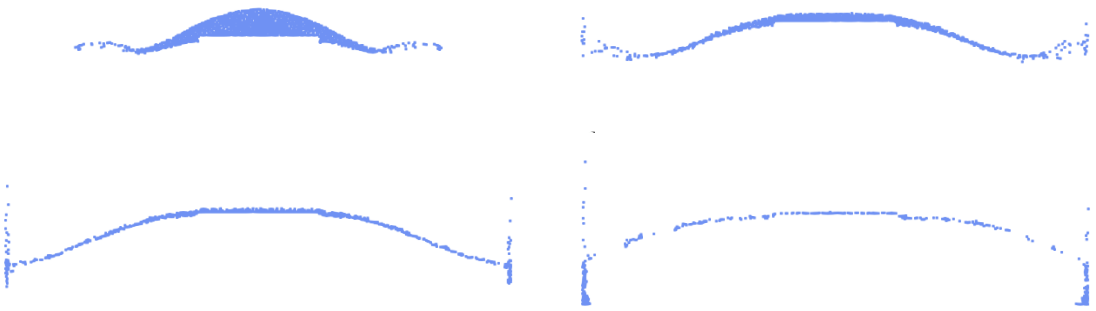

(d) 50 m/s

Figure 76. Snapshots of SLD impinging and freezing on an ice target at different speeds at t* = 0.918, 1.837, 2.755, and 5.511.
D = 0.5 mm, T_i = −11 °C, T_d = −21 °C, V = 5, 10, 20 & 50 m/s.

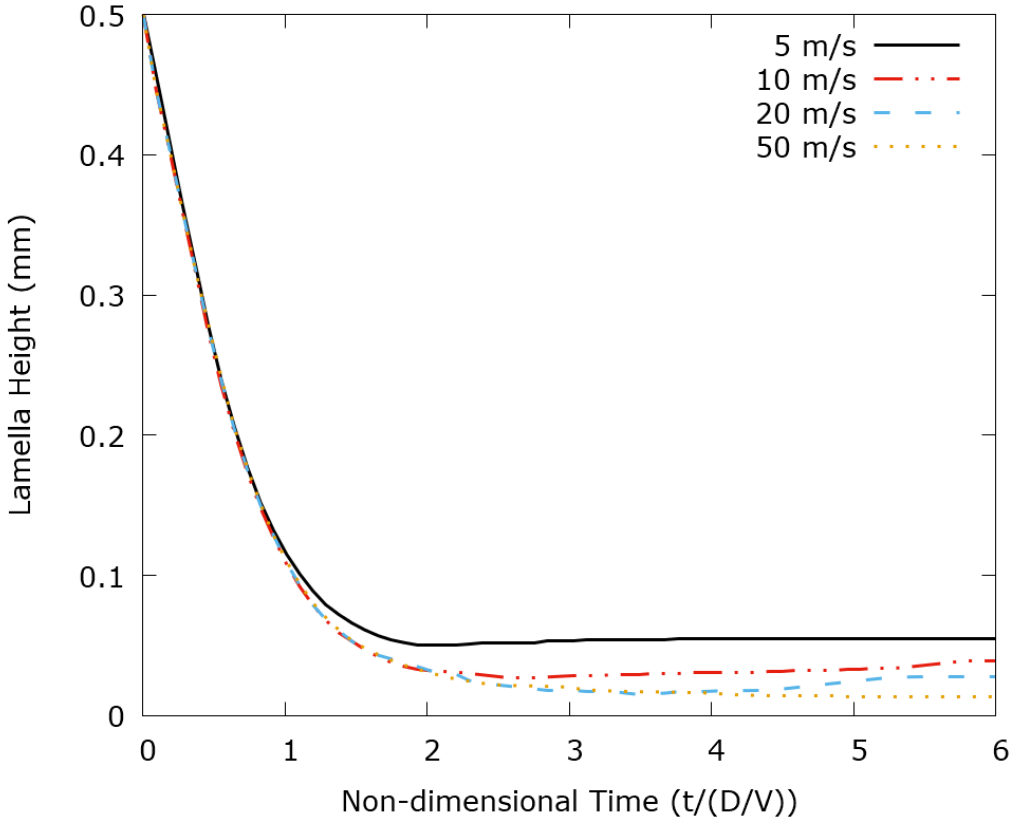

Figure 77. Time history of the lamella heights at different impact speeds.
D = 0.5 mm, T_i = −11 °C, T_d = −21 °C, V = 5, 10, 20 & 50 m/s.

CHAPTER 4 CONCLUSIONS

This thesis presents a highly-parallelized 3D triple-phase (air-water-ice) SPH solver to simulate single SLD impingement and solidification at in-flight icing conditions. This is accomplished by solving the Euler and energy equations, with latent heat and supercooled solidification models to represent phase change and dendritic freezing.

A judicious combination of models is applied to achieve a successful multiphase SPH framework. An artificial viscous term [33] and a diffusive term [37] are added, respectively, to the momentum and continuity equations to eliminate numerical instabilities. A multiphase model [34] is adopted to handle air-water interfacial flows, and a continuum surface tension model [51] is used to simulate surface tension effects. Boundary conditions are enforced by fixed ghost particles [41] and the occurrence of anisotropic particle distributions is alleviated by a particle shifting technique [39]. A simple and robust contact angle model is proposed to represent the non-wetting properties of hydrophobic/superhydrophobic surfaces through specifying the role of fixed ghost particles in the continuum surface tension model. A latent heat model is developed to represent phase change, and the ice fraction is used to describe the freezing process of water particles. A supercooled solidification model is proposed to simulate dendritic freezing and its interactions with fluid flow. In the context of high-performance computing, several parallelization strategies are employed to conduct parallel simulations in 3D partitioning, allowing the use of over 100 million particles.

The solver has been applied to SLD impingement and solidification problems under various conditions. In section 3.1, droplet impinging on a water film at low speed is simulated, and the time history of the water crown height and diameter are compared to the experimental data, showing good agreement. Aeronautical-speed impingements are then carried out with different

water film thicknesses, impact angles, speeds and droplet diameters, and their effects on post-impact water crowns are studied. In section 3.2, a two-phase Stefan problem and a stationary droplet freezing on a cold plate are used to validate the latent heat model, showing that the ice front movements agree with analytical and experimental results. Following this, normal and oblique droplet impingement and solidification at aeronautical speeds are simulated, and ice particle distribution analyzed, highlighting that high speeds can cause more splashing particles and that the front edge takes a longer time to freeze in oblique impingements. In section 3.3, water cuboids evolving into stationary droplets on surfaces with various contact angles are first conducted, and the diameters and heights of the equilibrium droplets match the analytical solutions. The solver then simulates droplets impacting hydrophobic and cold superhydrophobic surfaces, in both cases showing good agreement with experimental results. In section 3.4, impingement on an ice surface is simulated with a model incorporating supercooled solidification to investigate the interactions between fluid flow and dendritic freezing, showing the thickness of residual ice to agree well with experimental data. Following this, cases of different supercooling degrees and impinging speeds are conducted, showing that lower supercooling degrees and higher impact speeds can reduce the thickness of residual ice.

The solver's capabilities of simultaneously handling droplet dynamics, heat transfer, non-wetting phenomenon, phase transition and supercooled effects have been presented in this thesis. This numerical tool can simulate single SLD impingement and solidification at aeronautical speeds, advance the understanding of SLD behavior at in-flight icing conditions, and build a macroscopic SLD model for in-flight icing simulation codes.

Follow-up work could be focused on three aspects: (1) an adaptive resolution technique would greatly reduce the computational cost of SPH simulations, (2) combining SPH and a mesh-based

method would allow simulations with open boundaries and high-speed air flows to study SLD deformation and breakup due to aerodynamic shear forces, (3) reduced-order modeling would create a data-driven model to predict the SLD's post-impingement mass distributions for in-flight icing simulation codes.

REFERENCES

[1] W. G. Habashi. “Recent advances in CFD for in-flight icing simulations.” Japan Society of Fluid Mechanics, 28(2): 99-118, 2009.

[2] K. R. Petty and C. D. Floyd. “A statistical review of aviation airframe icing accidents in the US.” In Proceedings of the 11th Conference on Aviation, Range, and Aerospace, Paper ID: 11.2, 2004.

[3] FAA. “Airworthiness standards: transport category airplanes, in Appendix C to part 25, title 14.” Federal Aviation Administration. Amdt. 25-140, 79 FR 65528: 553-560, 2011.

[4] FAA. “Airworthiness standards: transport category airplanes, in Appendix O to part 25, title 14” Federal Aviation Administration. Amdt. 25-140, 79 FR 65528: 629-639, 2014.

[5] EASA. “Certification specifications and acceptable means of compliance for large aeroplanes CS-25.” European Union Aviation Safety Agency, 2019.

[6] TCCA. “Canadian aviation regulations.” Transport Canada Civil Aviation, SOR/96-433, 2019.

[7] D. Bilodeau, W. G. Habashi, M. Fossati and G. S. Baruzzi. “Eulerian modeling of supercooled large droplet splashing and bouncing.” Journal of Aircraft, 52(5): 1611-1624, 2015.

[8] R. Honsek, W. G. Habashi and M. S. Aubé. “Eulerian modeling of in-flight icing due to supercooled large droplets.” Journal of Aircraft, 45(4): 1290-1296, 2008.

[9] Z. Zhan. “Towards real time CFD simulation of in-flight icing via reduced-order modeling.” PhD Thesis, McGill University, 2016.

[10] Z. Zhan, W. G. Habashi and M. Fossati. “Real-time regional jet comprehensive aeroicing analysis via reduced-order modeling.” AIAA Journal, 54(12): 3787-3802, 2016.

[11] A. Bakkar. “A finite element level-set Eulerian model of supercooled large droplet dynamics.” PhD Thesis, McGill University, 2018.

[12] C. S. Bidwell and M. G. Potapczuk. “Users manual for the NASA Lewis three-dimensional ice accretion code (LEWICE 3D).” NASA Technical Memorandum 105974, NASA, 1993.

[13] R. Gent, J. Ford, R. Moser and D. Miller. “Results from super-cooled large droplet mass loss tests in the ACT Luton icing wind tunnel.” 41st AIAA Aerospace Sciences Meeting and Exhibit, AIAA Paper 2003-389, 2003.

[14] C. Tan, M. Papadakis, D. Miller, T. Bencic, P. Tate, and M. Laun. “Experimental study of large droplet splashing and breakup.” 45th AIAA Aerospace Sciences Meeting and Exhibit, AIAA Paper 2007-904, 2007.

[15] H. Li. “Drop impact on dry surfaces with phase change.” PhD Thesis, Technische Universität Darmstadt, 2013.

[16] Z. Jin, H. Zhang and Z. Yang. “Experimental investigation of the impact and freezing processes of a water droplet on an ice surface.” International Journal of Heat and Mass Transfer, 109: 716-724, 2017.

[17] M. Schremb and C. Tropea. “Solidification of supercooled water in the vicinity of a solid wall.” Physical Review E, 94(5): 052804, 2016.

[18] M. Schremb, J. M. Campbell, H. K. Christenson and C. Tropea. “Ice layer spreading along a solid substrate during solidification of supercooled water: experiments and modeling.” Langmuir, 33(19): 4870-4877, 2017.

[19] M. Schremb, I. V. Roisman and C. Tropea. “Normal impact of supercooled water drops onto a smooth ice surface: experiments and modelling.” Journal of Fluid Mechanics, 835: 1087-1107, 2018.

[20] X. Zhang, X. Liu, X. Wu and J. Min. “Impacting-freezing dynamics of a supercooled water droplet on a cold surface: rebound and adhesion.” International Journal of Heat and Mass Transfer, 158: 119997, 2020.

[21] L. Mishchenko, B. Hatton, Va. Bahadur, J. A. Taylor, T. Krupenkin and J. Aizenberg. “Design of ice-free nanostructured surfaces based on repulsion of impacting water droplets.” ACS Nano, 4(12): 7699-7707, 2010.

[22] T. Tezduyar. “Interface-tracking and interface-capturing techniques for computation of moving boundaries and interfaces.” In Proceedings of the Fifth World Congress on Computational Mechanics, 81513, 2002.

[23] C. W. Hirt and B. D. Nichols. “Volume of fluid (VOF) method for the dynamics of free boundaries.” Journal of Computational Physics, 39(1): 201-225, 1981.

[24] M. Sussman, P. Smereka and S. Osher. “A level set approach for computing solutions to incompressible two-phase flow.” Journal of Computational Physics, 114(1): 146-159, 1994.

[25] A. Bakkar, W. G. Habashi, M. Fossati and G. S. Baruzzi. “A hybrid Taylor–Galerkin variational multi-scale stabilization method for the level set equation.” Computers & Fluids, 121: 192-205, 2015.

[26] Y. Guo, Y. Lian and M. Sussman. “Investigation of drop impact on dry and wet surfaces with consideration of surrounding air.” Physics of Fluids, 28(7): 073303, 2016.

[27] Y. Guo and Y. Lian. “High-speed oblique drop impact on thin liquid films.” Physics of Fluids, 29(8): 082108, 2017.

[28] T. Xavier, D. Zuzio, M. Averseng and J. L. Estivalezes. “Toward direct numerical simulation of high speed droplet impact.” Meccanica, 55(2): 387-401, 2020.

[29] M. Tembely, R. Attarzadeh and A. Dolatabadi. “On the numerical modeling of supercooled micro-droplet impact and freezing on superhydrophobic surfaces.” International Journal of Heat and Mass Transfer, 127: 193-202, 2018.

[30] J. J. Monaghan. “Smoothed particle hydrodynamics.” Reposrt on Progress in Physics, 68(8): 1703, 2005.

[31] R. A. Gingold and J. J. Monaghan. “Smoothed particle hydrodynamics: theory and application to non-spherical stars.” Monthly Notices of the Royal Astronomical Society, 181(3): 375-389, 1977.

[32] L. B. Lucy. “A numerical approach to the testing of the fission hypothesis.” The Astronomical Journal, 82:1013-1024, 1977.

[33] J. J. Monaghan. “Simulating free surface flows with SPH.” Journal of Computational Physics, 110(2): 399-406, 1994.

[34] A. Colagrossi and M. Landrini. “Numerical simulation of interfacial flows by smoothed particle hydrodynamics.” Journal of Computational Physics, 191(2): 448-475, 2003.

[35] N. Grenier, M. Antuono, A. Colagrossi, D. Le Touzé and B. Alessandrini. “A Hamiltonian interface SPH formulation for multi-fluid and free surface flows.” Journal of Computational Physics, 288(22): 8380-8393, 2009.

[36] J. J. Monaghan and R. A. Gingold. “Shock simulation by the particle method SPH.” Journal of Computational Physics, 52(2): 374–389, 1983.

[37] D. Molteni and A. Colagrossi. “A simple procedure to improve the pressure evaluation in hydrodynamic context using the SPH.” Computational Physics Communications, 180(6): 861-872, 2009.

[38] R. Xu, P. Stansby and D. Laurence. “Accuracy and stability in incompressible SPH (ISPH) based on the projection method and a new approach.” Journal of Computational Physics, 228(18): 6703-6725, 2009.

[39] P. Sun, A. Colagrossi, S. Marrone and A. Zhang. “The plus-δ-SPH model: simple procedures for a further improvement of the SPH scheme.” Computer Methods in Applied Mechanics and Engineering, 315: 25-49, 2017.

[40] X. Cui, and W. Qiu. “Solving 2-D highly nonlinear free-surface problems with an improved smoothed particle hydrodynamics method.” Marine Systems & Ocean Technology, 13(2-4): 74-86, 2018.

[41] S. Marrone, M. Antuono, A. Colagrossi, G. Colicchio, D. Le Touzé and G. Graziani. “δ-SPH model for simulating violent impact flows.” Computer Methods in Applied Mechanics and Engineering, 200(13-16): 1526-1542, 2011.

[42] J. J. Monaghan. “Smoothed particle hydrodynamics and its diverse applications.” Annual Review of Fluid Mechanics, 44: 323-346, 2012.

[43] M. S. Shadloo, G. Oger and D. Le Touzé. “Smoothed particle hydrodynamics method for fluid flows, towards industrial applications: motivations, current state, and challenges.” Computers & Fluids, 136: 11-34, 2016.

[44] D. Violeau and B. D. Rogers. “Smoothed particle hydrodynamics (SPH) for free-surface flows: past, present and future.” Journal of Hydraulic Research, 54(1): 1-26, 2016.

[45] T. Ye, D. Pan, C. Huang and M. Liu. “Smoothed particle hydrodynamics (SPH) for complex fluid flows: recent developments in methodology and applications.” Physics of Fluids, 31(1): 011301, 2019.

[46] M. Zhang, H. Zhang and L. Zheng. “Simulation of droplet spreading, splashing and solidification using smoothed particle hydrodynamics method.” International Journal of Heat and Mass Transfer, 51(13-14): 3410-3419, 2008.

[47] N. Nishio, K. Yamana, Y. Yamaguchi, T. Inaba, K. Kuroda, T. Nakajima, K. Ohno and H. Fujimura. “Large scale SPH simulations of droplet impact onto a liquid surface up to the consequent formation of Worthington jet.” International Journal for Numerical Methods in Fluids, 63(12): 1435-1447, 2010.

[48] X. Yang, L. Dai and S.C. Kong. “Simulation of liquid drop impact on dry and wet surfaces using SPH method.” Proceedings of the Combustion Institute, 36(2): 2393-2399, 2017.

[49] P. W. Cleary and J. J. Monaghan. “Conduction modelling using smoothed particle hydrodynamics.” Journal of Computational Physics, 148(1): 227-264, 1999.

[50] J. J. Monaghan, H. E. Huppert and M. G. Worster. “Solidification using smoothed particle hydrodynamics.” Journal of Computational Physics, 206(2): 684-705, 2005.

[51] X. Y. Hu and N. A. Adams. “A multi-phase SPH method for macroscopic and mesoscopic flows.” Journal of Computational Physics, 213: 844–861, 2006.

[52] T. Breinlinger, P. Polfer, A. Hashibon and T. Kraft. “Surface tension and wetting effects with smoothed particle hydrodynamics.” Journal of Computational Physics, 243: 14-27, 2013.

[53] F. Amirsaman, B. Samareh and J. Mostaghimi. “Applying contact angle to a two-dimensional multiphase smoothed particle hydrodynamics model.” Journal of Fluids Engineering, 137(4): 041303, 2015.

[54] M. Ihmsen, N. Akinci, M. Becker and M. Teschner. “A parallel SPH implementation on multi-core CPUs.” In Computer Graphics Forum, 30(1): 99-112, 2011.

[55] M. Luo and C. G. Koh. “Shared-memory parallelization of consistent particle method for violent wave impact problems.” Applied Ocean Research, 69(1): 87-99, 2017.

[56] S. Marrone, B. Bouscasse, A. Colagrossi and M. Antuono. “Study of ship wave breaking patterns using 3D parallel SPH simulations.” Computers & Fluids, 69(1): 54-66, 2012.

[57] G. Oger, D. Le Touzé, D. Guibert, M. De Leffe, J. Biddiscombe, J. Soumagne and J. G. Piccinali. “On distributed memory MPI-based parallelization of SPH codes in massive HPC context.” Computer Physics Communications, 200(1): 1-14, 2016.

[58] M. Schaller, P. Gonnet, A. Chalk, and P. Draper. “SWIFT: using task-based parallelism, fully asynchronous communication, and graph partition-based domain decomposition for strong scaling on more than 100,000 cores.” In Proceedings of the Platform for Advanced Scientific Computing Conference, 2: 1-10, 2016.

[59] P. Goswami, P. Schlegel, B. Solenthaler and R. Pajarola. “Interactive SPH simulation and rendering on the GPU.” In Proceedings of the 2010 ACM SIGGRAPH/Eurographics Symposium on Computer Animation, pp: 55-64, 2010.

[60] J. M. Domínguez, A. J. C. Crespo and M. Gómez-Gesteira. “Optimization strategies for CPU and GPU implementations of a smoothed particle hydrodynamics method.” Computer Physics Communications, 184(3): 617-627, 2013.

[61] C. Peng, S. Wang, W. Wu, H. Yu, C. Wang and J. Chen. “LOQUAT: an open-source GPU-accelerated SPH solver for geotechnical modeling.” Acta Geotechnica, 14(5): 1269-1287, 2019.

[62] J. Bonet and T. S. Lok. “Variational and momentum preservation aspects of smooth particle hydrodynamic formulations.” Computer Methods in Applied Mechanics and Engineering, 180(1-2): 97-115, 1999.

[63] A. Zhang, P. N. Sun and F. Ming. ”An SPH modeling of bubble rising and coalescing in three dimensions.” Computer Methods in Applied Mechanics and Engineering, 294: 189-209, 2015.

[64] A. Colagrossi, M. Antuono and D. Le Touzé. “Theoretical considerations on the free-surface role in the smoothed-particle-hydrodynamics model.” Physical Review E, 79(5): 056701, 2009.

[65] C. Tropea, M. Schremb and I. V. Roisman. “Physics of SLD impact and solidification.” In Proceedings of the 7th European Conference for Aeronautics and Space Sciences, Milan, EUCASS2017-512, 2017.

[66] A. A. Shibkov, Y. I. Golovin, M. A. Zheltov, A. A. Korolev and A. A. Leonov. “Morphology diagram of nonequilibrium patterns of ice crystals growing in supercooled water.” Physica A: Statistical Mechanics and its Applications, 319: 65-79, 2003.

[67] G. Cossali, M. Marengo, A. Coghe and S. Zhdanov. “The role of time in single drop splash on thin film.” Experiments in Fluids, 36(6): 888-900, 2004.

[68] R. Merle and J. Dolbow. “Solving thermal and phase change problems with the extended finite element method.” Computational Mechanics, 28(5): 339-350, 2002.

[69] Y. Yao, C. Li, Z. Tao, R. Yang and H. Zhang. “Experimental and numerical study on the impact and freezing process of a water droplet on a cold surface.” Applied Thermal Engineering, 137: 83-92, 2018.

[70] R. Rioboo, M. Marengo and C. Tropea. “Time evolution of liquid drop impact onto solid dry surfaces.” Experiments in Fluids, 33(1): 112-124, 2002.

[71] I. Malgarinos, N. Nikolopoulos, M. Marengo, C. Antonini and M. Gavaises, “VOF simulations of the contact angle dynamics during the drop spreading: standard models and a new wetting force model.” Advances in Colloid and Interface Science, 212: 1-20, 2014.

[72] J. Blake, D. Thompson, D. Raps and T. Strobl. “Simulating the freezing of supercooled water droplets impacting a cooled substrate.” AIAA Journal, 53(7): 1725-1739, 2015.